Downloaded from orbit.dtu.dk on: Dec 20, 2017

Technical University of Denmark

DTU

Fabrication and Multiprobe Electrical Characterization of Nanostructures

Klarskov, Mikkel Buster; Bøggild, Peter

Publication date:
2013

Document Version
Publisher's PDF, also known as Version of record

Link back to DTU Orbit

Citation (APA):
Klarskov, M. B., & Bøggild, P. (2013). Fabrication and Multiprobe Electrical Characterization of Nanostructures.

DTU Library
Technical Information Center of Denmark

General rights
Copyright and moral rights for the publications made accessible in the public portal are retained by the authors and/or other copyright owners and it is a condition of accessing publications that users recognise and abide by the legal requirements associated with these rights.

- Users may download and print one copy of any publication from the public portal for the purpose of private study or research.
- You may not further distribute the material or use it for any profit-making activity or commercial gain
- You may freely distribute the URL identifying the publication in the public portal

If you believe that this document breaches copyright please contact us providing details, and we will remove access to the work immediately and investigate your claim.

DTU Nanotech
Department of Micro- and Nanotechnology

Danmarks Tekniske Universitet

Technical University of Denmark

Fabrication and Multiprobe Electrical Characterization of Nanostructures

A dissertation submitted in partial fulfillment of the requirements for the degree of Doctor of Philosophy

Author:
Mikkel Buster Klarskov

Supervisor:
Associate Professor
Peter Bøggild

Summer, 2012

Abstract

Engineering of graphene for modifying electrical properties, such as opening an electronic band gap, has been shown both theoretically and experimentally by creating periodic holes in the graphene sheet, however at the price of lower carrier mobility. Such holes can be made with special fabrication techniques, such as colloidal lithography or block copolymers lithography, which covers the entire sample. This project presents graphene devices with periodic holes fabricated by electron beam lithography. Only partial coverage of holes are fabricated by making from one to many rows of holes perpendicular to the current direction. The results show a decrease in carrier mobility with increasing number of rows, but does not indicate a band gap opening with holes sizes of 50 nm and a pitch of 100 nm, which suggests that smaller holes and pitch are necessary for creating band gap in graphene.

Electrical characterization of graphene and other nanostructures usually involves lithographic processing which can alter or damage fragile materials, and metal electrodes are permanently placed to the sample. This project presents a fast method for electrical characterization for graphene and other nanostructures by the use of micro four-point probes.

My contribution to knowledge includes characterization of graphene using micro four-point probes, which proves to be a fast and reliable method for electrical and mechanical characterization. The micro-four point probe technique is shown to apply to other fragile nanostructures, such as nanograss and silver nanowires. Furthermore, antidot lattice of different sizes are made in graphene, to investigating the dependence of number of holes needed for modifying the electronic properties of graphene.

Resumé

Fabrikation af graphene devices med formål at ændre de elektriske egenskaber, såsom at åbne et elektronisk båndgab, er blevet vist både teoretisk og eksperimentelt ved at skabe periodiske huller i graphene. Dette er dog ofte på bekostning af lavere ladnings mobilitet. Sådanne huller kan fremstilles med specielle fabrikationssteknikker, såsom kolloid eller blok copolymerer litografi, der som udgangspunkt dækker hele prøven. I dette projekt fabrikeres graphene prøver med periodiske huller fremstillet ved elektronstråle litografi. Dette gør at kun dele af prøven bliver dækket af huller, hvilket kan have en påvirkning på ladnings mobiliteten. Hullerne er fremstillet i rækker vinkelret på strømretningen. Resultaterne viser et fald i ladnings mobilitet med stigende antal rækker, men der er ikke antydning af et båndgab ved huller med størrelser på 50 nm og en periode på 100 nm. Dette tyder på, at mindre huller og periode er nødvendig for at skabe båndgab i graphene.

Elektrisk karakterisering af graphene og andre nanostrukturer involverer sædvanligvis litografisk behandling, der kan ændre eller beskadige skrøbelige materialer, og metalelektroder vil være en permanent ændring af prøven. Her præsenteres en hurtig fremgangsmåde til elektrisk karakterisering af graphene og andre nanostrukturer ved anvendelse af mikro fire-punkts prober.

Mit bidrag til viden omfatter karakterisering af graphene ved hjælp af mikro fire-punkts prober, der viser sig at være en hurtig og pålidelig metode for elektriske og mekaniske karakterisering. Mikro-fire point probe teknikken har vist sig også at gælde for andre skrøbelige nanostrukturer, såsom nanogræs og sølv nanotråde. Endvidere er et hullet gitter af forskellig størrelse fremstillet i graphene, for at undersøge et eventuelt båndgabs afhængighed af antallet af huller, samt andre ændringer af de elektroniske egenskaber i graphene.

Preface

This project was carried out at DTU Nanotech - Department of Micro- and Nanotechnology, at the Technical University of Denmark, DTU. It is PhD project in the Nanointegration group and was supervised by Associate Professor Peter Bøggild.

Acknowledgement

I would like to thank the following people for their help and guidance during this project. The Danchip staff, Helle V. Jensen, Majken Rasmussen, Conny Hougaard, Yvonne Gysling for general cleanroom help. Peixiong Shi, Hassan Ouacha, Rune Christensen and Tine Griebe for electron beam processing, and the rest of Danchip staff for their assitance. From Copenhagen University, I would like to express thanks to Nader Payami for help with wirebonding of samples, Shivendra Upadhyay and Rune Hviid for e-beam exposures, and Søren Petersen for experiments with reduced graphene oxide. My great thanks to the Post Docs. in the group, Tim Booth, Dirch Petersen and David Mackenzie for their priceless guidance, ideas and discussions. The Nanointegration group for their inspiring input and ideas, especially my fellow PhD students for their help during the project, and my supervisor Peter Bøggild for his encouraging guidance and for promoting a cheerful atmosphere during this project. Finally I would like to thank my beloved wife and son for love and support during the project.

List of Acronyms

AC	Alternating Current
BCP	Block Copolymer
CL	Colloidal Lithography
CAD	Computer Aided Design
CVD	Chemical Vapor Deposition
DAQ	Data Acquisition Card
DC	Direct Current
E-beam	Electron Beam
EBL	Electron Beam Lithography
FIB	Focused Ion Beam
GAL	Graphene Antidot Lattice
GNR	Graphene Nanoribbons
HOPG	Highly Oriented Pyrolytic Graphite
IC	Integrated Circuit
IPA	Iso-Propanol
ITO	Indium Tin Oxide
KOH	Potassium Hydroxide
LOR	Lift-off Resist
MIBK	Methyl Isobutyl Ketone
M4PP	Micro Four-Point Probe
NMP	N-Methyl Pyrrolidone
PCB	Printed Circuit Board
PMGI	Polydimethyl Glutarimide
PMMA	Poly(methyl methacrylat)
RIE	Reactive Ion Etching
sccm	Standard Cubic Centimeter per Minute
SEM	Scanning Electron Microscope/Microscopy
SiO_2	Silicon Dioxide
TEM	Transmission Electron Microscope/Microscopy
TiW	Titanium Tungsten
TMAH	Tetramethyl Ammonium Hydroxide
UV	Ultra Violet
ZIF	Zero Insertion Force

List of mathematical symbols

ϵ_0	Permittivity of vacuum ($8.854 \cdot 10^{-12}$ F/m)
ϵ_r	Relative permittivity of SiO_2 (3.9)
ϵ	Permittivity of SiO_2, product of ϵ_0 and ϵ_r
e	Electron charge ($1.602 \cdot 10^{-19}$ C)
h	Planck's constant ($6.626 \cdot 10^{-34}$ J·s)
$\hbar$	Reduced Planck's constant ($1.054 \cdot 10^{-34}$ J·s)
k	Boltzmann constant ($8.617 \cdot 10^{-5}$ eV/K)
t	Thickness of SiO_2
T	Temperature
σ	Conductance
V_g	Gate voltage
n	Charge carrier density
k or $\vec{k}$	Crystal momentum
m_c (m_v)	Electron (hole) mass
v_F	Fermi velocity ($5 \cdot 10^8$ m/s)
E_c (E_v)	Energy in conductance (valence) band
E_c^0 (E_v^0)	Minimum (maximum) energy level of conduction (valence) band
E_g	Band gap

Contents

1 Introduction **2**
- 1.1 Graphene Background . . . 2
- 1.2 Motivation . . . 6
- 1.3 Summary . . . 6

2 Nanopatterned Graphene **8**
- 2.1 Graphene . . . 8
- 2.2 Electrical Properties . . . 10
  - 2.2.1 Gating Graphene . . . 13
  - 2.2.2 Band Gap in Graphene . . . 15
- 2.3 Bandgap Engineering of Graphene . . . 15
  - 2.3.1 Graphene Nanoribbons . . . 15
  - 2.3.2 Antidot Lattice . . . 17
  - 2.3.3 Block Copolymer . . . 17
  - 2.3.4 Colloidal Lithography . . . 19
  - 2.3.5 Periodic gating . . . 19
- 2.4 Summary . . . 20

3 Experimental Methods **22**
- 3.1 Graphene Fabrication . . . 22
  - 3.1.1 Substrate . . . 22
  - 3.1.2 Cleaving . . . 24
- 3.2 Raman Spectroscopy of Graphene . . . 26
- 3.3 Wet Chemistry on Graphene . . . 27
- 3.4 Graphene Etching . . . 28
- 3.5 Device Fabrication . . . 30
  - 3.5.1 Electron Beam Lithography . . . 30
- 3.6 Electron Beam Irradiation . . . 32
- 3.7 Fixed Electrodes . . . 33
- 3.8 Summary . . . 34

4 Micro Four-Point Probes 36
4.1 Theory . . . 36
4.1.1 Errors . . . 38
4.2 Methods . . . 39
4.2.1 Probes . . . 39
4.3 Setup . . . 40
4.4 Micro Four-Point Probes . . . 41
4.4.1 Aligning and Approach . . . 41
4.4.2 Issues . . . 42
4.5 Electrical Characterization of Silver Nanowires . . . 44
4.6 Mechanical Impact on Vertical Nanowires . . . 45
4.7 Summary . . . 46

5 Hysteresis and Contamination 48
5.1 Hysteresis in Graphene Field Effect . . . 48
5.2 Contamination and Irradiation . . . 49
5.2.1 Splitting of the Charge Neutrality Point . . . 51
5.3 Summary . . . 51

6 Nanopatterned Graphene 52
6.1 Raman Analysis . . . 52
6.2 Variations in Number of Rows . . . 54
6.2.1 Band gap in Antidot Lattice . . . 56
6.3 Summary . . . 58

7 Conclusions 60

8 References 62

A E-beam Fabrication Process 74

B Graphene Identification 78
B.1 Graphene Identification . . . 78
B.2 Image Recognition and Processing . . . 79
B.3 Image Recognition Code . . . 80

C Articles 84
C.1 Fast and direct measurements of the electrical properties of graphene using micro four-point probes . . . 84
C.2 Micro-cantilever for non-destructive characterization of nanograss uniformity . . . 91
C.3 Direct Electrospinning of Ag-Polyvinylpyrrolidone Nanocables . . . 96

D Patents 104
D.1 Automatic Identification of Single- and/or Few-layer Thin-Film Material . . . 104

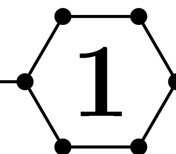

Introduction

The electronic industry has never produced devices at a higher rate as they are today. Cell phones, laptops and tablets are commercialized within few years, and continuously being smaller, lighter and faster. Furthermore, precise and fast characterization in production of new nanomaterials are needed for process control. However, fabrication limit in silicon drives researchers to look for alternative materials. One of these promising materials is graphene.

1.1 Graphene Background

In 1965, Gordon Moore described what he expected to be the trend for future silicon processing, and predicted that the number of transistors per unit area would double every 18-24 months. His prediction set a benchmark for the processor industry, which have been compelled to follow this prediction. An illustration of this trend is shown in Fig. 1.1.

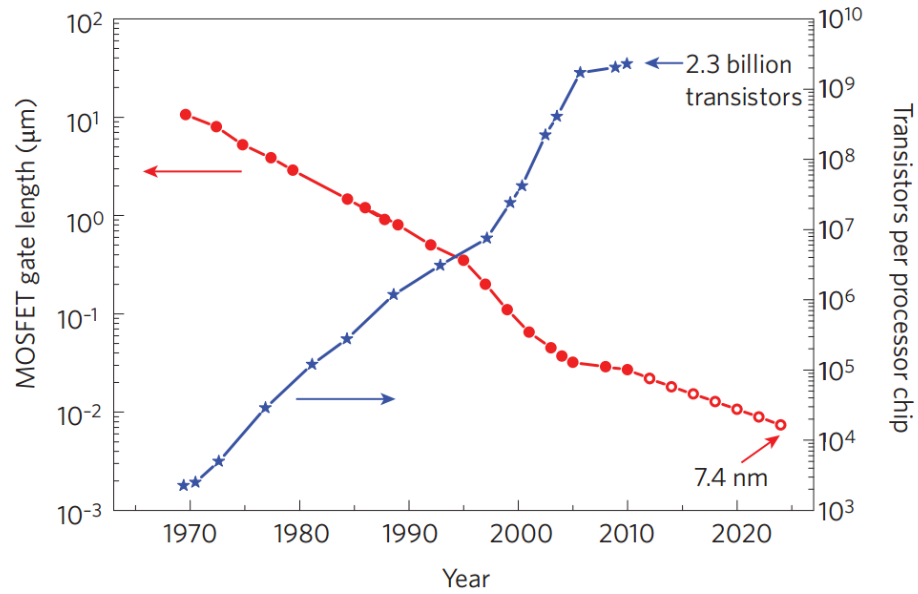

Figure 1.1: Illustration of Moore's law, showing the exponential tendency of number of transistors per unit area, which doubles every 18 months. Also shown is the gate oxide thickness exponentially decreasing. Figure from [1].

However, fabrication techniques is an increasing challenge with this trend, and to overcome this, research have redirected some effort into materials and technologies alternative to silicon. Both for higher processing speeds, smaller device structures, and lower costs [2]. Such a material should have higher electrical mobility than silicon and have an adjustable band gap up to 400 meV [1].

	Electron(hole) mobility [cm^2/Vs]	Band gap [eV]	Effective carrier mass
Si	1400(450) [3]	1.12	0.19(100)
Ge	3900(1900) [4, 5]	0.66 [6]	0.082(111)
GaAs	8500(400) [7]	1.42 [7]	0.063
InAs	40000(500) [8]	0.35 [9]	0.023
Carbon nanotube	100000 [10]		
Supported graphene	15000 [11]	0 [11]	0 [11]
Suspended graphene	200000 [12]	0	0

Table 1.1: Carrier mobility, Band gap and effective mass of charge carriers for typical semiconducting materials.

Possible candidates, such as gallium arsenide (GaAs), germanium (Ge), indium arsenide (InAs) and carbon nanotubes (CNT) has been suggested. A summary of their electrical properties are listed in table 1.1.

Recently another candidate for electronics, has been isolated experimentally [13]. It consists of a single layer of carbon atoms in a honeycomb lattice. The layer originates from graphite, which is a stacked structure with these individual layers named graphene [14]. Graphene is the two dimensional allotrope of carbon, as shown in Fig. 1.3 [15].

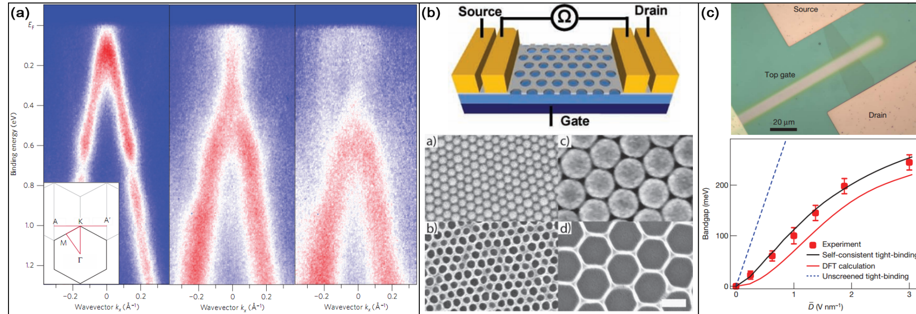

Figure 1.2: Three different examples for creating a band gap in graphene, **(a)** chemically/structural, **(b)** structural and **(c)** by gating. **(a)** Photoemission intensity of graphene on Ir exposed to various doses of atomic hydrogen [16]. **(b)** Holes made in graphene using colloidal lithography [17]. **(c)** Bilayer graphene with top and bottom gate contacts, where band gap is created by a strong displacement field from the bottom electrode [18].

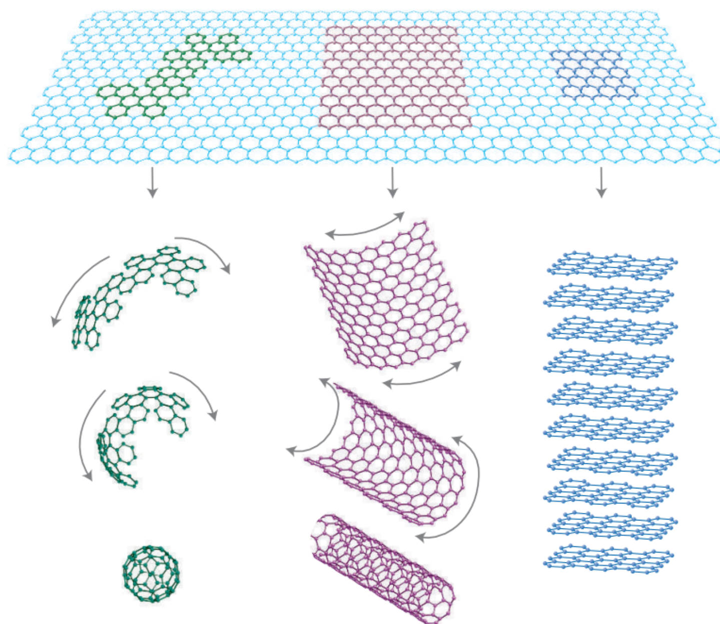

Figure 1.3: Allotropes of carbon. At the top is depicted a single layer of graphene showing the honeycomb lattice, and by slicing and forming it is possible to create the the zero dimensional buckeyball, the one dimensional carbon nanotube, and the three dimensional structure of graphite. Figure from [15].

Graphene has promising properties of future electronics, such as high carrier mobilities at room temperature, but misses one important quality; a band gap. A band gap is necessary for defining on and off states in logic circuits and for achieving gain in analog electronics [19]. It has been shown that it is possible to construct a band gap, and primarily three different methods has been used; by chemical doping, nanostructuring into ribbons or antidot lattices or by applying an electrostatic gate to a bilayer graphene. Fig. 1.2 shows some research examples of chemical, nanostructuring and gating for creating a band gap in graphene, while detailed description of nanostructuring of graphene is described in chapter 2.

1.2 Motivation

Electrical measurements on graphene usually involves lithography patterning of fixed metal electrodes, which is both time consuming and permanent. In the process the sample can be contaminated by resists, solvents, and irradiation, which is also potentially destructive and can alter the electronic structure of as-fabricated graphene. Micro four-point probes (M4PP) on graphene is a real alternative to fixed electrodes, similar to what has been achieved with M4PP in the semiconductor industry [20]. M4PP allows greater flexibility, positionability, comparable accuracy and lesser damage in measurements of nanostructures compared to fixed electrodes. Using M4PP on graphene and other nanostructures may introduce damage, which may be minimized by careful placement, fast measurements and optimized design of the probes, and M4PP may be positioned precisely for electronic measurements on nanostructures. Furthermore, electron imaging of graphene may damage and/or contaminate the sample leading to reduction of the electrical conductance and mobility.

The last section showed some of the possibilities for creating a band gap in graphene. However, the price is usually lower carrier mobilities [21], and antidot structuring of graphene flakes usually mean that the whole flake is patterned, making scattering events frequencies much higher. Partial patterning of antidot structures may achieve the same effect and offer the minimal decrease of carrier mobility. Electron beam lithography, which is a well established technique, is capable of delivering such small patterns, which may be sufficient for electrical modification of graphene.

1.3 Summary

This chapter described briefly the background area of graphene research, which is continued in this project. The electrical characterization of graphene can be expensive and time consuming, so a new technique using micro-four point probes is proposed. Furthermore, altering the electrical properties by a reduced antidot structure is suggested.

Chapter 2 will give an overview of graphene and its electronic properties, and introduce the antidot lattice in graphene. Chapter 3 illustrates the fabrication techniques for graphene and nanostructures, and the techniques used the characterization of samples. In chapter 4 is shown the uses of micro four-point probes on sensitive nanostructures and how the probes can interact with various samples. Chapter 5 presents electrical measurements of graphene which includes hysteresis and contamination measurements. Finally, chapter 6 shows results from measurements on antidot graphene, and how the number of holes in graphene affect the electrical properties.

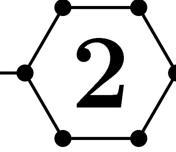

NANOPATTERNED GRAPHENE

Continuing from last chapter, this chapter will describe in further detail the structure, electrical properties of graphene, and the state of art of band gap creation through nanostructuring.

2.1 Graphene

As previous mentioned, graphene consists of carbon atoms in a planar honeycomb lattice. Carbon is the 6th element in the periodic table, in Group IV, meaning it has six electrons, of which four are valence electrons. The four valence electrons occupy the 2s and the 2p orbitals. This electron configuration when hybridized allows for sp^2 and sp^3 hybridized orbitals. The sp^3 results in a diamond crystal, whereas the sp^2 results in in-plane bonding, as shown in Fig. 2.1. The 2s orbital hybridize with the $2p_X$ and the $2p_Y$ orbitals, leading to three in-plane σ-bonds to neighboring carbon atoms. The last p_Z orbital is perpendicular to the plane, and creates π-bonds to the neighboring atoms. The electrons in the σ-bond are very localized to the atoms, while the electrons in the π-orbitals are delocalized, and can easily move through the lattice. The delocalization in the π-orbitals, combined with the relativistic nature of the charge carriers, which allows for Klein tunneling [22], contributes to a long mean free path in graphene.

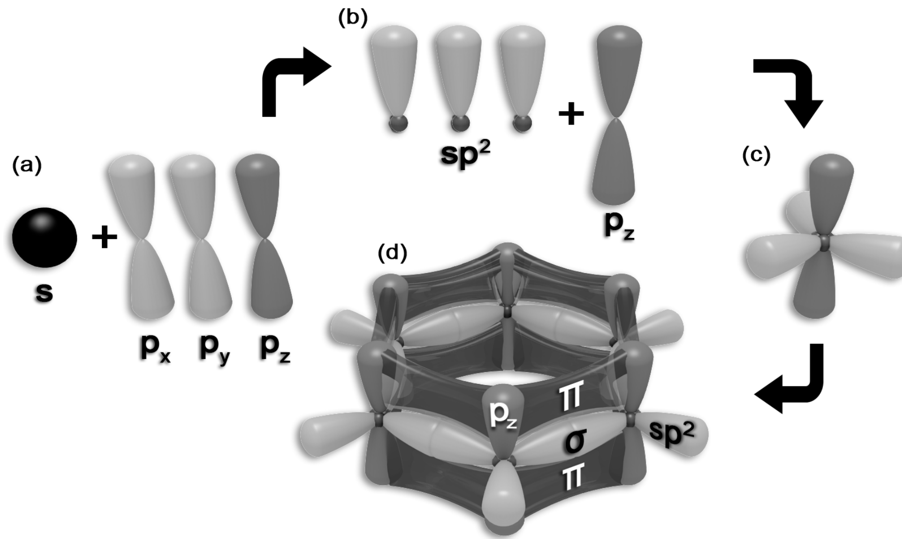

Figure 2.1: sp^2 hybridization of carbon. **(a)** One 2s and three 2p orbitals. **(b)** Hybridization into three sp^2 orbitals, leaving one 2p orbital. **(c)** Structure of the hybridized carbon atom. The sp^2 orbitals lies in the plane, while the p_z orbital is perpendicular to the plane. **(d)** Six carbon atoms combined to benzene, which can be considered to be the smallest possible graphene, a graphene quantum dot [23].

Combining multiples hexagonal rings, graphene is constructed in a honeycomb pattern, as shown in Fig. 2.2a. For an infinite sheet, the reciprocal lattice is also a hexagonal lattice, although rotated by 90 degrees. The first Brillouin zone is shown in Fig. 2.2b, which also marks the points M, K, K' and Γ. The K and K' points are the most relevant points for the electrical properties of graphene.

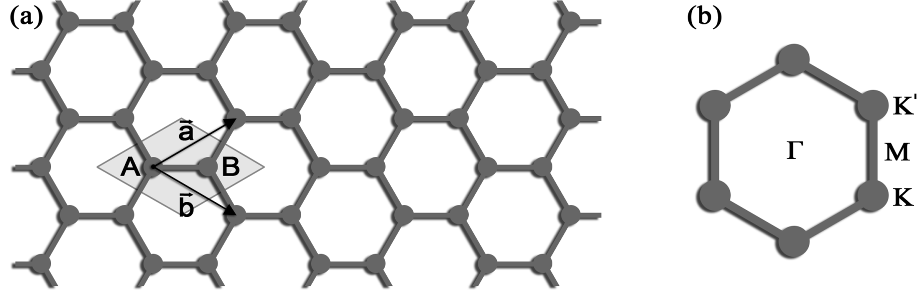

Figure 2.2: **(a)** Graphene consists of carbon atoms in a hexagonal lattice with a lattice spacing of 1.42 Angstrom. The unit cell is shown in light gray, which contains the atoms A and B. Also shown is the lattice vectors $\vec{a}$ and $\vec{b}$, which shifting the unit cell along these vectros result in the complete infinite graphene sheet.. **(b)** The first Brillouin zone of the reciprocal lattice, with indication of the K, K', M and Γ points.

2.2 Electrical Properties

Theoretical calculations by P. R. Wallace in graphene [24] were made long before the experimental realization, who showed that graphene had a linear dispersion relation, which means that the mobility close to the charge neutrality point is independent of the charge carrier density. This was later experimentally verified [13], and it was found that electrons did not obey the Schrödinger equation, but the *relativistic* Dirac equation:

$$\begin{aligned} \text{Time} - \text{dependent} \quad \text{equation} \quad &: \quad i\hbar\frac{\partial}{\partial t}\Psi = \hat{H}\Psi \\ \text{Schrödinger} \quad &: \quad \hat{H} = -\frac{\hbar^2}{2m}\nabla^2 + V(\mathbf{r}, t) \\ \text{Dirac} \quad &: \quad \hat{H} = c\alpha \cdot \hat{\mathbf{p}} + \beta mc^2 \end{aligned}$$

From the reciprocal lattice (Fig. 2.2b), the band structure of graphene can be calculated using ab initio [25] or tight binding calculations [26]. From tight binding calculations, the band structure is given as [27]:

$$E = \pm\sqrt{\gamma_0^2\left[1 + 4\cos^2\left(\frac{k_y a}{2}\right) + 4\cos\left(\frac{k_y a}{2}\right)\cdot\cos\left(\frac{k_x\sqrt{3}a}{2}\right)\right]}, \qquad (2.1)$$

where γ_0=2.8 eV and a=2.46 Angstrom. The ± indicates the conduction and valence band respectively. The band structure is shown in Fig. 2.3c.

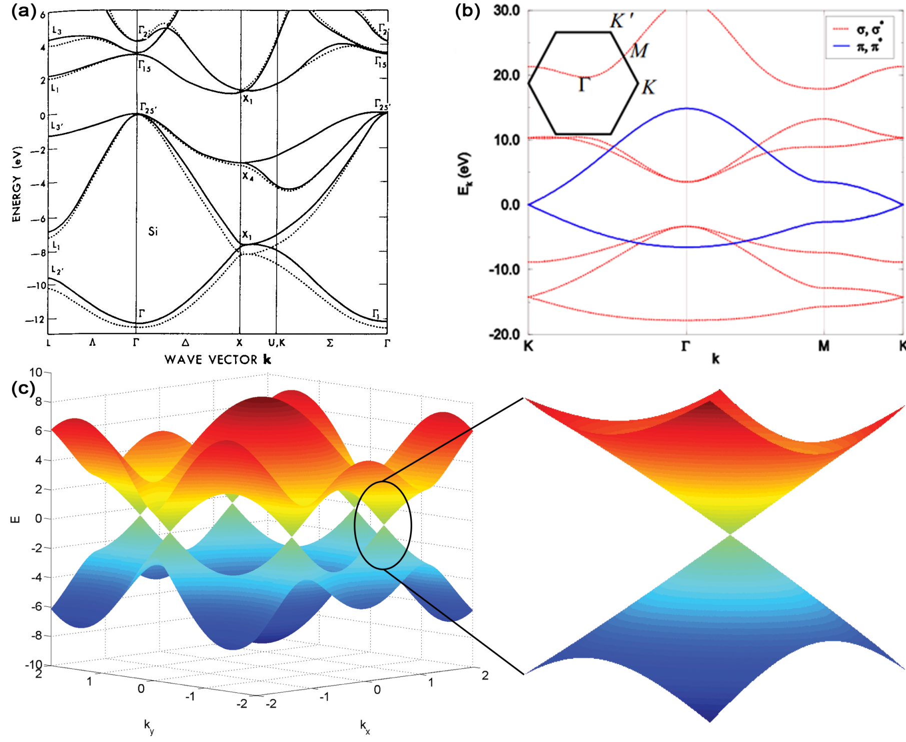

Figure 2.3: **(a)** Band diagram of silicon. **(b)** and **(c)** Band diagram and graphene. The conductance and valance bands of silicon near the Fermi energy can be approximated by a polynomial, whereas the dispersion relation in graphene is linear. Silicon band diagram from [28].

Comparatively, the electrical properties of graphene are quite different from those of silicon. The band diagram for silicon is shown in Fig. 2.3a. The main feature of this diagram is the approximate parabolic dispersion relation near the Fermi energy; at $\Gamma_{25'}$ in the valence band and at X_1 in the conduction band. Furthermore, silicon has an indirect band gap. The energy near the Fermi level can be approximated by:

$$E_c = E_c^0 + \frac{\hbar^2 k^2}{2m_c^2} \qquad\qquad E_v = E_v^0 - \frac{\hbar^2 k^2}{2m_v^2},$$

where the parabolic nature of the bands (k^2) is visible. Fig. 2.3b shows the band diagram for graphene, as calculated from tight-binding approximations. In contrast to silicon, graphene does not have a band gap, but near the Fermi

level, at K and K', the dispersion relation is linear, and is approximated by:

$$E = \pm v_F \hbar |\vec{k}|,$$

where v_F is the Fermi velocity, and $\hbar$ is the reduced Planck's constant. If the Fermi energy is below the Dirac energy, the majority carriers are holes (p doping), and if the Fermi energy is above, electrons are the major carriers (n doping). At the K and K' point there are no carriers for conduction at zero temperature, and the point is also known as the charge neutrality point (CNP).

The first electronic measurements on single layer graphene was made by Novoselov et al. [13], and this showed this contrasting electrical characteristic compared to typical semiconductors. The parabolic dispersion relation for silicon and the fact that the mobility is proportional to $\frac{dE}{dk}$, means that in the limit of zero charge carriers, the mobility tends towards zero. For graphene, Novoselov et al. [11] showed that the electronic transport was dictated by massless relativistic fermions, and measured both the electron and hole mobilities to 15.000 cm^2/Vs at low temperatures. Fig. 2.4 is from the first article on experimental fabricated graphene, where a linear dependence between conductance and gate voltage can be seen in Fig. 2.4B.

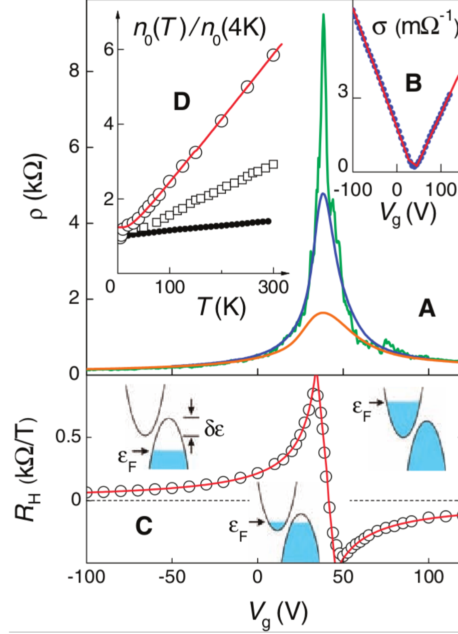

Figure 2.4: Figure from [13]. **A** Resistivity of graphene vs. gate voltage. The peak position denotes the charge neutrality point(CNP). **B** The conductivity of the sample at 70 K, where the mobility is proportional to the linear slope. **C** Hall resistance.

The theoretical limit on mobility imposed by acoustic phonons scattering was later found to be as high as 200.000 cm^2/Vs [29, 30]. These calculations are for planar graphene at room temperature without interaction with environment or substrate. Experimental measurements have exceeded this limit with mobilities in suspended graphene at low temperatures at 230.000 cm^2/Vs [12], and lately Tombros et al. fabricated suspended samples with mobilities up to 600.000 cm^2/Vs [31]. These high mobilities are more than 400 times higher than for silicon [3].

2.2.1 Gating Graphene

Varying a gate voltage in a graphene device, effective changes the charge carrier density according to [32],

$$n = \frac{\epsilon}{te} V_g = \alpha V_g \tag{2.2}$$

where n is the charge carrier density, ϵ is the relative permittivity of the gate insulator, t is the thickness of the insulator, and e is the electron charge. With a gate insulator consisting of SiO_2 of 90 nm or 300 nm, α is $2.4 \cdot 10^{15} (cm \cdot V)^{-1}$

and $7.2 \cdot 10^{14}(cm \cdot V)^{-1}$ respectively. The conductance of a graphene sample depends on the charge carrier density and the carrier mobility:

$$\sigma = ne\mu, \tag{2.3}$$

where e is the electron charge and μ is the carrier mobility. By combining equation 2.2 and 2.3, the conductance should be zero for no applied gate voltage. However, experimentally, there is a conductance minimum, which can also be seen in Fig. 2.4B. This minimum arises from electron/hole puddles in the graphene sheet, which originates from the presence of disorder [33]. The fact that graphene sheet are not completely planar [34], and contains impurities or disorder in the lattice results in a non-zero conductance at the CNP. Many research groups has found this minimum conductance experimentally to be $4e^2/h$ or higher [15], where the theoretical prediction is $4e^2/\pi h$. The value of $4e^2/h$ is equal to about 0.155 mS.

Carrier mobilities is calculated from equations 2.2 and 2.3, and the slope of the conductance dependence on gate voltage away from the CNP as

$$\mu = \frac{t}{\epsilon}\frac{d\sigma}{dV_g}. \tag{2.4}$$

2.2.2 Band Gap in Graphene

A practical method for measuring the band gap in graphene devices is by measuring the conductance at different temperatures, because the conductance in the presence of a band gap is exponential with temperature [35]:

$$\sigma = \sigma_0 \exp\left(-\frac{E_g}{2kT}\right), \tag{2.5}$$

where k is Boltzmann constant, T is temperature and E_g is the bandgap. Measuring the conductance at different temperatures, and plotting the natural logarithm of the conductance against the inverse temperature, the band gap can be calculated from the slope as:

$$E_g = -2k \cdot \text{slope}. \tag{2.6}$$

This is used in the experimental chapter for determining band gaps.

2.3 Bandgap Engineering of Graphene

As seen in equation 2.1 and in Fig. 2.3, the valence and conduction bands meet in six discreet points, making graphene a semimetal or a zero-bandgap semiconductor [24]. Such a property is desirable in for example a photovoltaic cell which will absorb light at all wavelengths and thereby increase the efficiency of the cell. For other components, electrical logic switching depends on a bandgap and a non-zero on-off ratio [1], which makes usable graphene transistor devices impossible from pristine graphene.

However, graphene does excel as having the highest intrinsic mobility and maximal current density at room temperature [36], and compared to silicon it can be used more efficiently and faster in electronics [1]. The main challenge and focus with graphene electronics has therefore been producing a band gap. Numerous research groups has worked on this issue [16–18, 21, 37–44], using the three different techniques mentioned in the introduction; chemical, structural and gating of bilayer transistors. The following sections provide a review of the state of art of structural modification of graphene.

2.3.1 Graphene Nanoribbons

Graphene nanoribbons (GNR) are graphene etched into strips, making it a quasi one-dimensional structure. Earlier work with carbon nanotubes shows that single walled carbon nanotubes can have large band gaps in part due to the lateral confinement [45, 46]. As with carbon nanotubes, the chirality [47, 48] of the graphene nanoribbon plays an important role; graphene with zigzag edges produces metallic states, while armchair can be either metallic or semiconducting depending on the width. If an armchair graphene nanoribbon does produce a band gap it depends inversely on the width of the graphene nanoribbon [40, 49].

Theoretical calculations shows a band gap opening with decreasing GNR width, but also a decrease in mobility (Fig. 2.5(a)-(b)) [21]. Several groups has confirmed the band gap opening, and reduction of mobility, see Fig. 2.5.

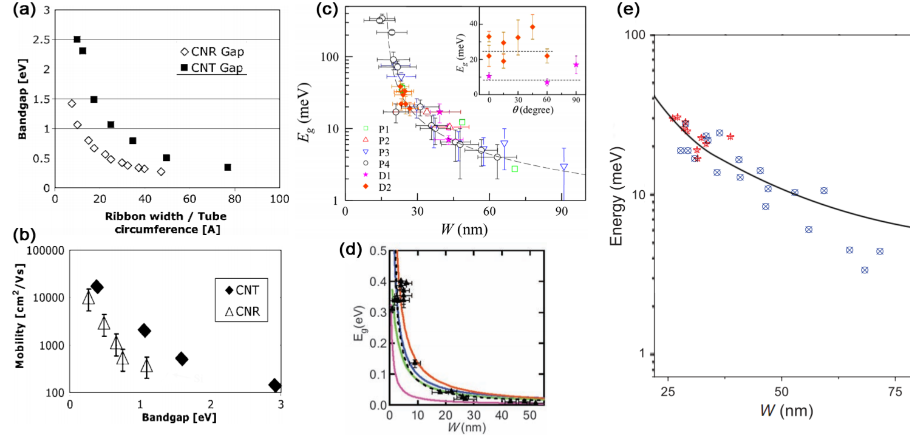

Figure 2.5: **(a)**-**(b)** Theoretical comparison of band gap and mobility between carbon nanotubes and graphene nanoribbons. **(c)**-**(e)** Experimental measurements from different groups which confirms the bandgap opening for narrow GNR. **(a)** and **(b)** from [21]. **(c)** from [39]. **(d)** from [50]. **(e)** from [38].

2.3.2 Antidot Lattice

Another possible way to structure the graphene was proposed by Pedersen et al. [51], where periodic holes (antidots) were made in graphene, as shown in Fig. 2.6a. A band gap of up to 1 eV was predicted. The main difficulty with this approach, is the theoretical calculations estimates hole size of 1-2 nm, which is a impossible task to realize experimentally with current technology. However, the important relation is the ratio of number of atoms removed and number of atoms in total ($\frac{\sqrt{N_{removed}}}{N_{total}}$) in a unit cell. Special fabrication techniques for achieving small holes has been used, such as block copolymer and colloidal lithography.

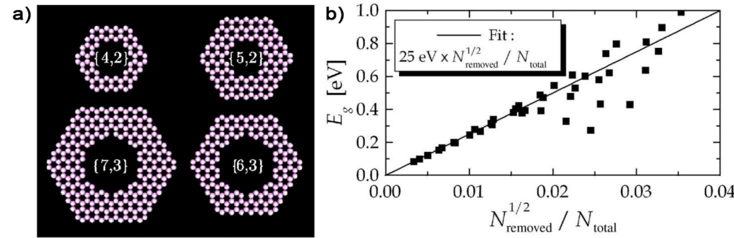

Figure 2.6: Theoretical structure and calculation of graphene antidot lattice. **(a)** Unit cells of various numbers of atoms removed. **(b)** Relation between bandgap and the root of removed atoms divided by total number of atoms in the unit cell ($\frac{\sqrt{N_{removed}}}{N_{total}}$) is linear. Figure adapted from [51].

2.3.3 Block Copolymer

A block copolymer consists of two different polymers. Polymers usually does not mix due to entropy [52], but heterogenic polymers will separate in smaller domains, such as a hexagonal cylinders or lamella ridges, which can be used in lithography.

Bai et al. [42] showed this experimentally with a PMMA-PS block copolymer, with neck widths down to 7 nm. The electrical measurements shows a field effect, as shown in Fig. 2.7, which they believe arises from the confinement of the current to a semi one dimensional structure in the spacing between the holes. Later the bandgap of a graphene antidot lattice was measured by to be in the range 60-140 meV [41], which depended on the neck width (Fig. 2.8). This was comparable to the graphene nanoribbons previously made, however the mobility was lower than pristine graphene at 1000 cm^2/Vs for holes and 200 cm^2/Vs for electrons for the antidot lattice.

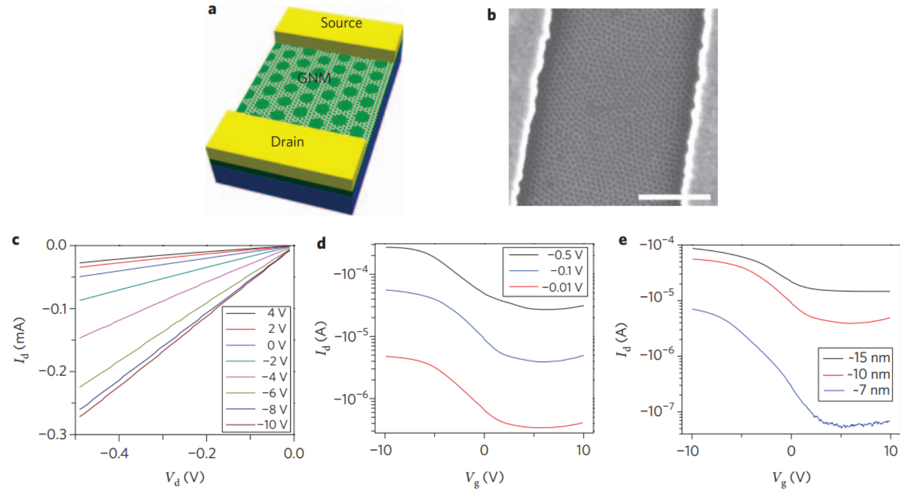

Figure 2.7: **(a)** Schematic of graphene nanomesh device. **(b)** SEM image of graphene nanomesh with hole periodicity of 39 nm and diameters of 10 nm. **(c)** I-V characteristics for various gate voltages. **(d)** Transfer characteristics for different drain voltages. An on-off ratio of 14 is estimated at -100 mV. **(e)** Transfer characteristic at various neck widths, which indicates the smaller the neck width, the higher on-off ratio. Figure from [42].

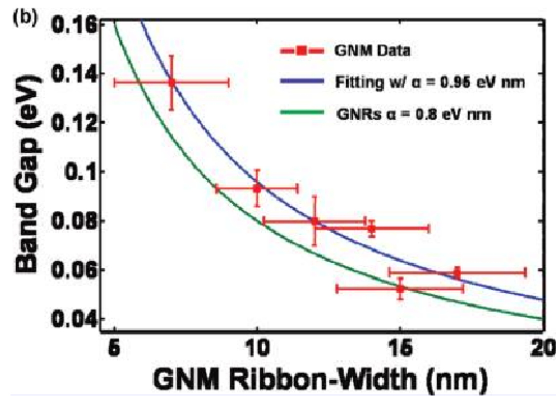

Figure 2.8: Bandgap dependence on neck width of graphene antidot lattice made with BCP. The results are compared to those of graphene nanoribbons. Fig. from [41].

2.3.4 Colloidal Lithography

A similar fabrication technique to BCP is using colloidal lithography (CL). Colloidal lithography involves spinning of spheres of polystyrene [17,37] or silica [53] onto a graphene sample. The mask is reversed by a metal deposition. The advantages of CL over BCP is that it can be used directly on graphene, whereas BCP requires a neutral surface for the BCP to align. The electrical measurements in Fig. 2.9(c)-(d), shows a field effect arising from the antidot lattice and a reduction in mobility.

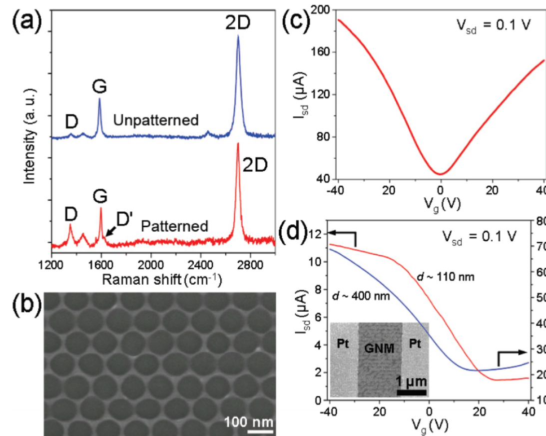

Figure 2.9: Fabrication of graphene antidot lattice with CL by Sinitskii et al. [53]. **(a)** Raman map of sample before and after etching. **(b)** SEM image of antidot sample. **(c)** Transfer characteristic before and after **(d)** CL and etching.

2.3.5 Periodic gating

Resent research has indicated that actual perforation of the graphene sheet is not necessary for band gap opening. Pedersen et al. [54] shows that periodic gating results in a band gap of approximately 30 meV. Fig. 2.10 illustrated the theoretical prediction of band gap opening at varying applied gate voltages. This type of antidot lattice have the potential of retaining the carrier mobility in graphene.

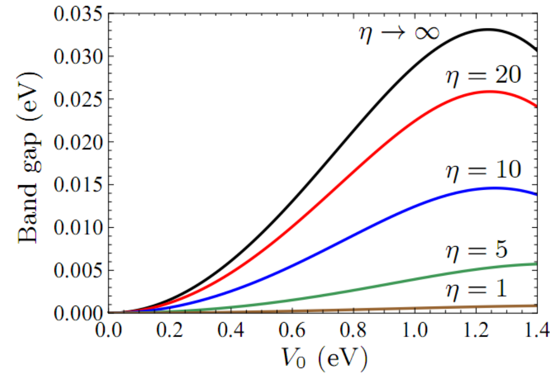

Figure 2.10: Band gap opening for different applied gate voltages for periodic gating of graphene. η is a smoothing function of the applied voltage. Band gap opening is possible, although smaller than periodic perforated graphene. Fig. from [54].

2.4 Summary

This chapter described the structure and properties of graphene with and without an antidot lattice. The high carrier mobility is favorable in fabrication of graphene devices, however fabrication of antidot lattices for band gap opening will reduce the mobility. Antidot lattices in graphene has been fabricated by the use of block copolymers or colloidal lithography, resulting in band gaps of up to 140 meV.

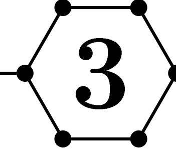

Experimental Methods

This chapter will describe in detail the fabrication process used for making graphene devices in this project.

3.1 Graphene Fabrication

Graphene was first isolated by Geim and Novoselov et al. [13] via micromechanical cleavage. Other methods have since been introduced, such as chemical vapor deposition (CVD) growth on copper or nickel [55–57], or epitaxial growth on silicon carbide [58–60], which can produce graphene on wafer scale or foils. Other methods includes fabrication of a graphene-like material from reduction of graphene oxide [61–63] or even unzipping of nanotubes [64, 65].

In this project, cleaving graphene from natural graphite is used for large single-crystalline domains and low defect density [15].

3.1.1 Substrate

For electronic measurements, the interaction between substrate and the graphene is very pronounced [44, 66], and it is therefore critical to choose the correct substrate and substrate treatment. Typically, a silicon wafer with a silicon dioxide (SiO_2) layer is used [17, 29, 33, 67–73]. The purpose of the SiO_2 is twofold; to serve as a gate dielectric between the substrate and the graphene, and to enhance the optical contrast of the graphene.

The relatively high optical absorption of 2.3% visible light per layer [74], is usually not sufficient to observe single layers using optical microscopy. It has however been shown that with proper thickness of the SiO_2 substrate, the contrast can be increased as much as up to 15%, due to optical interference in the SiO_2 [75]. Figure (3.1) shows how the contrast between the substrate and the graphene depends on the thickness of SiO_2 and the wavelength of the light [75].

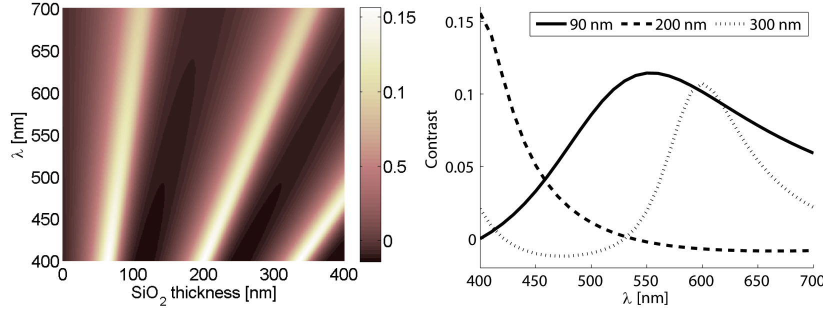

Figure 3.1: Optical contrast of graphene as function of SiO_2 thickness and wavelength of the light. Right figure shows 90 nm and 300 nm SiO_2 has contrast higher than 10%, whereas graphene on 200 nm SiO_2 will be almost invisible. Figure made with data from [75].

From the above figure, it is clear that a thickness of 90 nm or 300 nm is preferable for optimal optical contrast. In this project, both 90 nm and 300 nm SiO_2 were used. The advantage of 90 nm SiO_2 is that the contrast is higher than 10% for light in the range 520-605 nm, while 300 nm SiO_2 only has higher than 10% contrast in the range 590-610 nm, however 300 nm SiO_2 has a smaller risk of gate leaks. Furthermore, for 90 nm SiO_2 only 30% of the gate voltage is needed compared to 300 nm SiO_2. For M4PP measurements, 90 nm SiO_2 is used, while for fixed electrodes the thickness is 300 nm SiO_2.

The initial wafers are highly doped ($<0.025\Omega$cm) wafers, which are used to grow a dry thermal oxide. Using standard photolithography, a coordinate system with index markers are defined on the wafer using 5/50 nm Ti/Au. Each coordinate point is referred to as an index mark, and is used for logging the locations of graphene flakes.

3.1.2 Cleaving

Graphene is produced by micromechanically cleaving of natural graphite from graphit.de onto SiO_2 wafers. Prior to exfoliation, the wafer is baked on a hotplate at 110°C for 5 minutes, and cleaned in a oxygen (200 sccm) and nitrogen (50 sccm) plasma at 1000 W for 10 minutes, in order to remove surface water and organic residues which reduces the adhesion between graphene and substrate. Preparation of graphite is done by pressing graphite onto Nitto Denko tape. A new piece of tape is placed on top, and when pulling the tape apart, the graphite is on both pieces of tape. This is done 3-4 more times to reduce the amount of large graphite chunks, and finally the tape is applied to the wafer straight after plasma clean. Using a 50°C hotplate, the tape is slowly released from the wafer by thermal breakdown of the adhesive, leaving graphene and graphite behind.

To locate the graphene, the wafer is scanned in a Nikon Eclipse L200 optical microscope, either manually or using a robust, calibration-free scanning and graphene identification system [76], which captures images at 10x magnification, and saves all images to disk. Single layer graphene is identified by 10% contrast with the substrate, as shown in Fig. 3.2. The program was made by Bjarke Jessen Sørensen [76], and outputs only the images with graphene and corresponding black and white images masking the single layer graphene area with a yield close to 100%. Appendix B.1 describes the process in detail, and the patent is in appendix D.1.

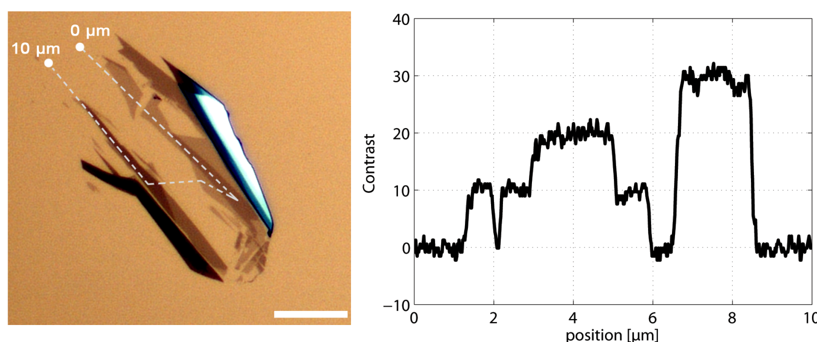

Figure 3.2: Contrast of one, two and three layer graphene compared to SiO_2 substrate from one of my samples. Each layer contributes to 10% contrast, and single layered flakes are identified using this method. Extracted curve is along the dotted line in the image.

For graphene samples which would be patterned by e-beam lithography, I made a script (appendix B.3) to ease the design process. The script detects the angle of rotation of the image, does image recognition of the index marks, identifies

the position of the graphene, and exports the data to a .cif-file. Multiple images can do done a once, resulting in a single .cif-file, which can be directly imported into a CAD drawing program, see appendix B.2.

Prior implementation of this method, the process included 2-4 hours of graphene identification at the microscope, and 2-3 hours of aligning graphene and design patterns per wafer. Known issues with the software is proper identification of the numbers 0 and 8 if metal residues exists after lift-off, as seen in some number in Fig. 3.3.

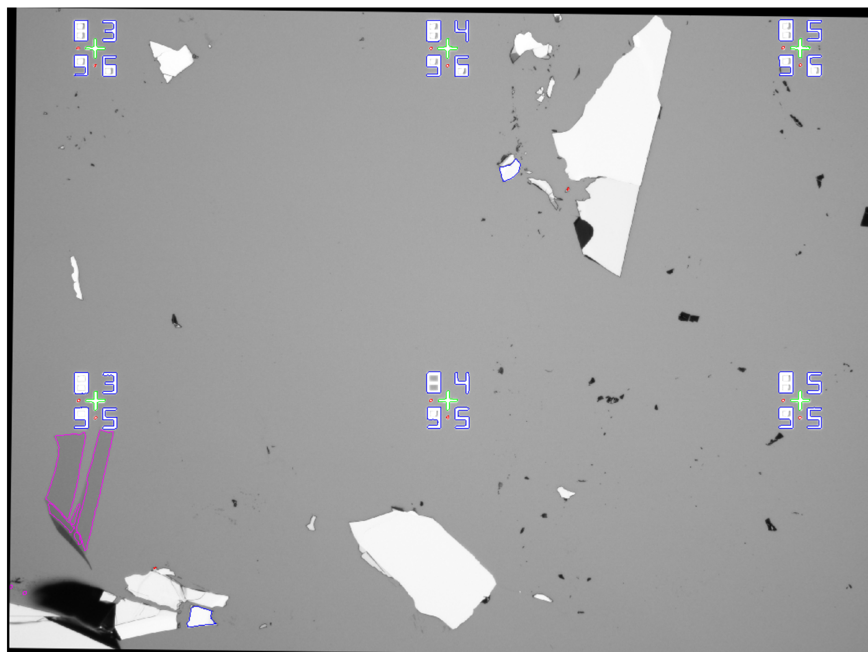

Figure 3.3: Sample output from image analysis from graphene scanning. The program identifies index mark locations (green), does image recognition of numbers (blue), quadrant (red) and graphene (purple). The program also auto-rotates images.

3.2 Raman Spectroscopy of Graphene

A fast and non-destructive method of characterization of graphene is using Raman spectroscopy. Raman spectroscopy gives information about vibrational and rotational modes by scattering of laser light in the sample. A example of a Raman map is shown in Fig. 3.4.

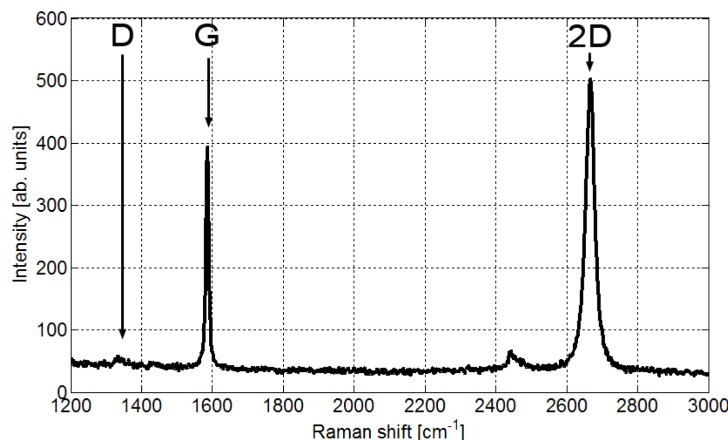

Figure 3.4: Raman spectrum from sample b4w5A with the three most important peaks, D, G and 2D marked.

The three major peaks in Raman spectroscopy of graphene is the D peak around 1350 cm^{-1}, the G peak around 1580 cm^{-1} and the 2D peak around 2700 cm^{-1}. The D peak is associated with disorder of the graphene lattice, indicating edge states or amorphous carbon. While the intensity of the peaks depends on the Raman system used, for comparable results the ratio of the D and G peak intensities, I_D/I_G, is a better indicator for defect density. Similarly, the ratio of the 2D and G peak, I_{2D}/I_G, indicates the number of graphene layers, where a ratio of one indicates single layer graphene.

For Raman spectra in this project, a Thermo Scientific DXR Raman Microscope is used. The spot size is around 1 μm, and a map can be generated with user defined step-sizes. Spectra are made with 10x magnification.

3.3 Wet Chemistry on Graphene

After fabrication and identification of graphene flakes, consideration about further processing is necessary, since cleanroom fabrication which includes graphene, gives some limitations to standard cleanroom processing due to concerns with cross contamination. Graphene can be damaged or unwantingly released from the substrate surface. Several commonly used and obvious process steps are known to cause damage to graphene, such as oxygen plasma [77, 78] or ultrasonic agitation [79]. In liquid environments graphene can withstand most chemicals, but not if the surface energy of the liquid matches that of graphene. In that case, the graphene flakes will be lifted from the surface [80]. Table 3.3 list surface energies for some common chemical in cleanroom fabrication, which illustrates that chemicals containing NMP, such as 1165 or remover PG, should be avoided when doing graphene fabrication, since it will lift the graphene from the SiO_2 surface.

Material	Surface energy $[\frac{mJ}{cm^2}]$
Graphene	46.7 [81]
Water	72
NMP	41
Acetone	25
Iso-propanol	23
MIBK	24
KOH	72-98 [82]

Table 3.1: Surface energies of graphene and common chemicals. If the surface energy match that of graphene, graphene will be lifted off the surface [80], so for example NMP is to be avoided in processing. Unreferenced values are from [83].

3.4 Graphene Etching

Etching of graphene is done in a reactive ion etching (RIE) process using an oxygen plasma. The process was tailored for etching of graphene using Poly(methyl methacrylat) (PMMA) as masking material. The critical issue with regard to etching graphene is making sure not to crosslink or sputter the resist, which will make it difficult to remove after the etching process.

To optimize etching parameters, graphene flakes with regions of single-, bi- and tri-layers were e-beam patterned in 3x3 μm squares, which are visible in an optical microscope. It was found that high volume of Ar, introduced sputtering of the resist, and to improve etching, low Ar and high O_2 volumes were chosen. Furthermore, the power was set low to avoid inconveniently short etching times, and the parameters, 45 sccm O_2, 5 sccm Ar, at 40 mTorr and 10 W were chosen.

In order to establish the etching process, characterization was done by evaluating the contrast in a optical microscope. Several consecutive attempts with 2 seconds etching showed no change in contrast, however for 3 seconds, a single layer of graphene was etched, but not bi- or tri-layer. Consecutive etching processes of 3 seconds duration showed contrast of 10% of each layer. Fig. 3.5 shows a sample with multiple layers etched for increasing periods of time.

The RIE system uses gas stabilization before processing, and the ignition of the plasma takes 2 seconds. Therefore, at least 3 seconds were needed for single layer etching.

Fig. 3.6 shows the precise tailoring of the graphene etching process, which could be interpreted as layer-by-layer etching. However, the etching of graphene produces amorphous carbon, so partially etched samples would not be pristine graphene. Fig. 3.5(f) shows the Raman spectrum of single-layer pristine graphene, and a bilayer etched for 3 seconds, which shows a significant D-peak at 1350 cm^{-1}, indicating amorphous carbon [77].

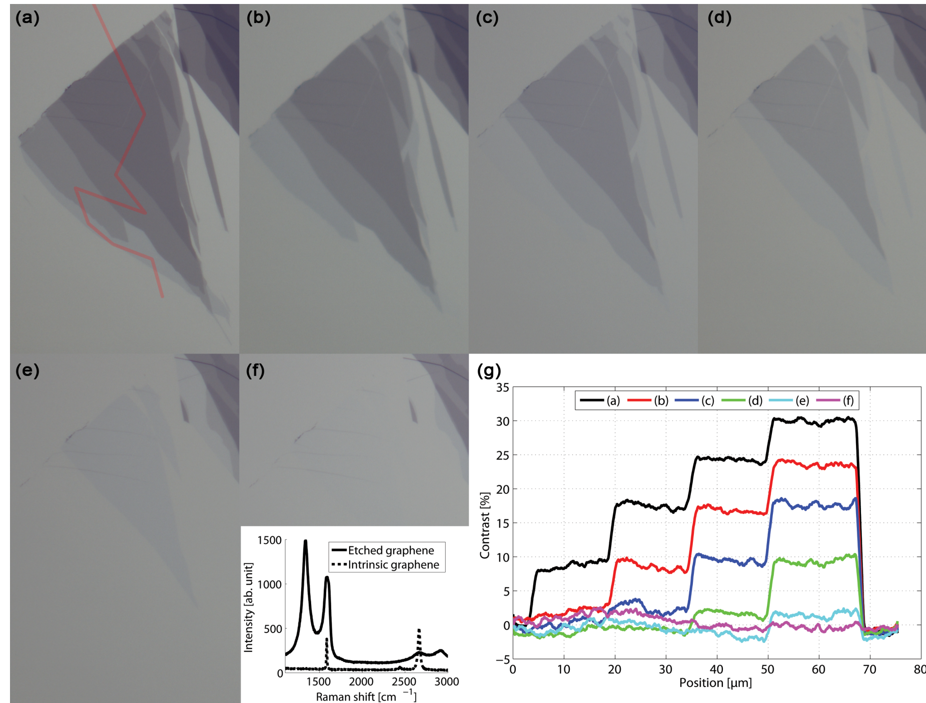

Figure 3.5: Etching of a graphene sample consisting of one to four layers. With increasing etching times, it is possible to thin down a graphene sample, however producing amorphous carbon as a result. Contrast profiles in **(g)** is along the red line in **(a)**. Raman map in lower part of **(f)** shows amorphous carbon after etching.

The etching process also etches the PMMA, so to test the durability of PMMA as an etch mask, holes of 50 nm diameter and 100 nm pitch where transferred in a honeycomb pattern to the graphene using e-beam lithography as described in section 3.5, and etched for 3-7 seconds. The size of the holes increase with time as shown in Fig. 3.6.

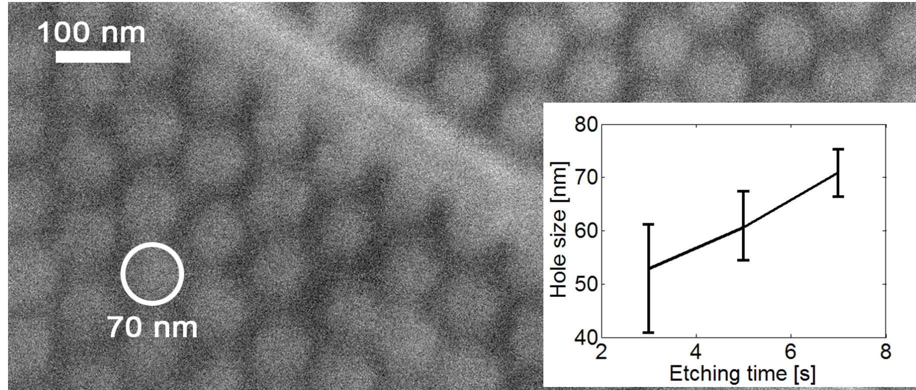

Figure 3.6: Overetched graphene sample. The holes were designed in a honeycomb lattice with hole diameter of 50 nm and a pitch of 100 nm. The overetching resulted in a hole diameter of 70 nm, leaving 30 nm of graphene between the holes. Inset shows hole diameter for three different etch times.

3.5 Device Fabrication

This section describes the fabrication process of graphene Hall bars using electron beam lithography (EBL).

3.5.1 Electron Beam Lithography

Graphene devices were fabricated in a two-step e-beam process, metallization and etching. Metal contacts can be made on a surface using standard photolithography, however, the random positioning of graphene flakes, makes e-beam lithography a suitable choice for custom contacts. The first mask step defined the metal contacts, and the second defined the etching pattern of the graphene sample. The lithography steps were done in this order, since the metallization proved to enhance the yield of devices, by pinning the graphene to the surface. The lithography was performed on a Joel JBX9300FS writer. For the metallization step a dose of 1000 μC/cm^2 and a current of 41 nA were used, while for the etching step a dose of 1000-16000 μC/cm^2 and a current of 0.2 nA were used (see appendix A). The high current can be used for the metallization since the smallest features are around 1 μm, and the high current reduces writing time.

Metallization and lift-off

The first lithography step consists of a bilayer resist of 350 nm LOR and 300 nm PMMA, with LOR as lift-off resist, and PMMA as patterning resist. After

e-beam exposure, PMMA is developed and an undercut is made in the LOR using diluted Tetramethyl ammonium hydroxide (TMAH), 50% in water. Metal deposition of 10 nm Cr and 100 nm Au are done at a low rate of 1 Å/s in order to reduce stress in the metal. Lift-off is a two step process; first the sample is immersed in acetone for 10-15 minutes for metal lift-off and PMMA removal, followed by 5 minutes in TMAH to remove the LOR. These steps are shown in Fig. 3.7(a)-(e).

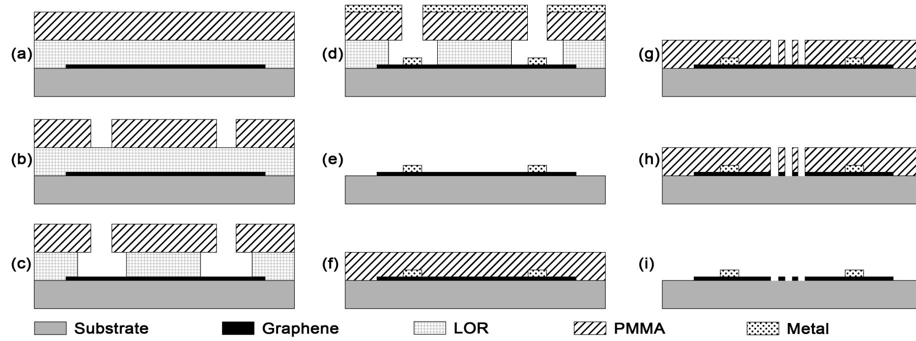

Figure 3.7: Schematic of e-beam fabrication process. **(a)** PMMA and LOR resist stack. **(b)** Development of PMMA after e-beam exposure. **(c)** Undercut of LOR resist. **(d)** Metal deposition. **(e)** Metal lift-off. **(f)** PMMA deposition. **(g)** Development after e-beam exposure. **(h)** Graphene etching. **(i)** Resist removal.

Twelve metal contacts are placed in a circle around the device, each 400x400 μm in size, which can be connected using probes, as shown in Fig. 3.9.

Graphene patterning

The second lithography step consist of an etch mask for defining a multielectrode Hall bar structure. The Hall bar has four measurement areas; graphene, one row of holes, three rows of holes and a mesh of holes. The device is fabricated on a single crystal graphene flake. The Hall bar is 2 μm in width, and each area is 4 μm in width. The lithography step uses two different beam currents; one for nanoscale structures (hole pattern) and one for microscale structures (Hall bar boundary and electrodes). Following the lithography step, the samples are etched as described in section 3.4 and the resist is removed. Fig. 3.7(f)-(i) shows the second lithography step, and a final device is shown in Fig. 3.8 and in Fig. 6.1a.

Appendix A shows the fabrication process in detail.

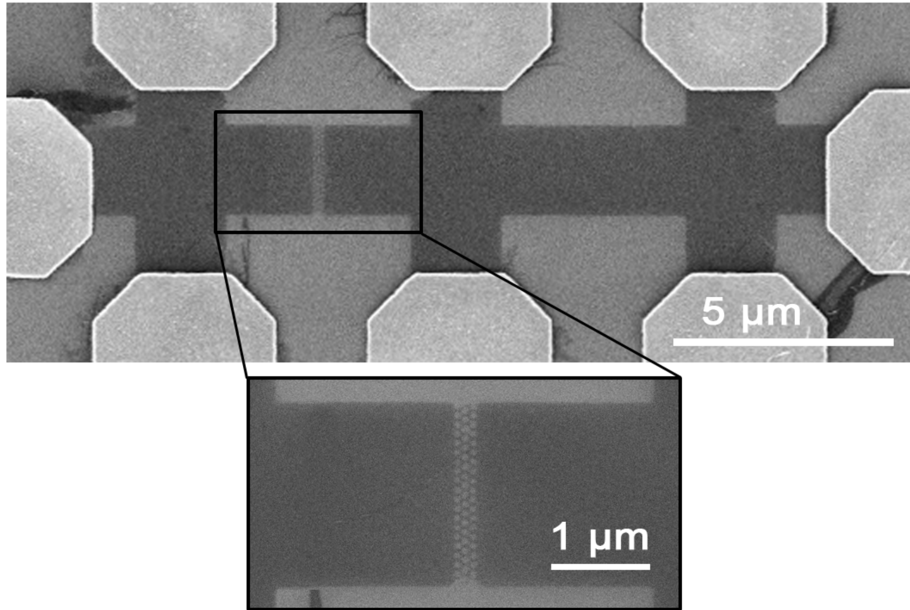

Figure 3.8: Multielectrode Hall bar device fabricated by e-beam lithography. Bottom figure shows 3-dotted lines.

3.6 Electron Beam Irradiation

The effect of electron beam irradiation during scanning electron microscopy is discussed in the following. Samples for electron beam irradiation were made as described in section 3.1. To protect the graphene during imaging, diluted AZ5214e (2:1 in PMGEA) was spun at 6000 rpm for 50 seconds with an acceleration of 500 rpm/s. This resulted in a 200 nm thick layer. Irradiation of the sample was performed by aligning the electron beam to a known index mark, turning off the electron beam, translate the stage to the position of the graphene and irradiate the sample for the desired time. For my samples, I used a magnification of 10.000 and irradiated for 3 minutes, which resulted in a dose of 5.000 $\mu C/cm^2$. This dose was chosen since it has shown to drastically alter the electrical properties [77, 84, 85].

After irradiation, the resist is removed in acetone.

3.7 Fixed Electrodes

Measurements with fixed lithographic contacts were measured using a Linkam stage, which allows for eight electrical connections. The stage has a heater and cooling elements, and the chamber can be sealed in low vacuum or a controlled atmosphere (see Fig.. 3.9).

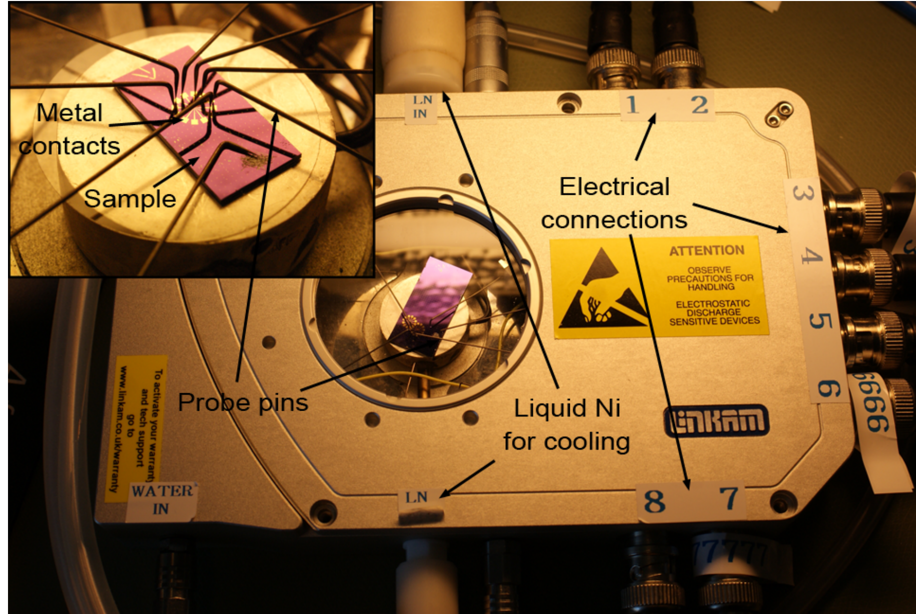

Figure 3.9: Graphene sample with fixed metallic electrodes mounted on the Linkam stage under vacuum. Inset shows probe pins connected to contact pads for electrical connections.

Measurements are performed by applying a voltage and measuring the current through the Hall bar. The voltage drop over each section of the Hall bar is measured simultaneously, as illustrated in Fig. 3.10. The Hall bar is fabricated from a single cleaved graphene flake, so any difference between flakes are eliminated.

All electrodes attached to the Hall bar is tested before measurements. Two-point measurements are performed across V_1, then V_2 and so on, until all electrodes to the Hall bar has been tested. Although a metal connection can visually appear to be functional, all connections are tested in this manner, before four-point measurements are performed. The system is put under vacuum, followed by both gated and temperature measurements. The gate sweep rate is set 100 ms/V_g (see section 5.1), and done at temperature is the range -150°C - +50°C.

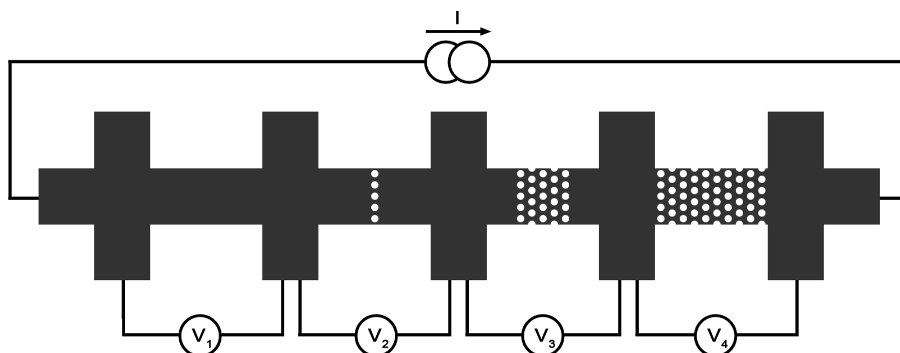

Figure 3.10: Technique for measuring on hallbar. A constant voltage drop is applied across the hallbar, the current and the four voltage drops are measured. Holes are not to scale.

3.8 Summary

This chapter described in detail the fabrication processes using for making graphene and graphene devices. Fabrication of graphene and graphene devices consist of several step, including lithography, etching and wet chemistry. All processes are potential damaging for graphene, so extra care needs to be taken with chose of chemicals and etching parameters. The chapter also introduce Raman spectroscopy of graphene and the electrical setup used for the fixed metal electrodes on graphene. The next chapter will describe the use of micro four-point probes on graphene which is a fast and flexible alternative to fixed electrodes for characterization of nanostructures.

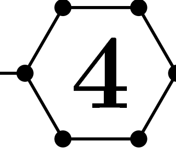

Micro Four-Point Probes

Last section described the process of fabricating graphene, graphene devices and experimental methods used in this project. However, by using micro four-point probes (M4PP), it is possible to perform measurements without any lithography, and to measure is different positions. This section will describe the theory of micro four-point probes technology and measurements, and illustrate the fabrication of probes and the construction and design of the measurement setup.

4.1 Theory

The most straightforward way to measure the electronic properties of a sample, would be to attach two wires to the sample, let a current (I) run through it, measure the voltage drop (V) and calculate the conductance as $G = \frac{I}{V}$. However, such a two-point measurement will also include the serial resistance of the wires, spreading and contact resistances. A better way is to contact the sample with four independent electrodes, and measure the voltage drop across two of these, while passing a current through the two other electrodes. This will eliminate all wire- and contact-resistances, since the supplied current is the same in a serial circuit, and the voltmeter has a very high internal resistance.

With four connections to the sample, there exist six different combinations of current- and voltage-connections (shown in Fig. 4.1), where only five of them are independent [86].

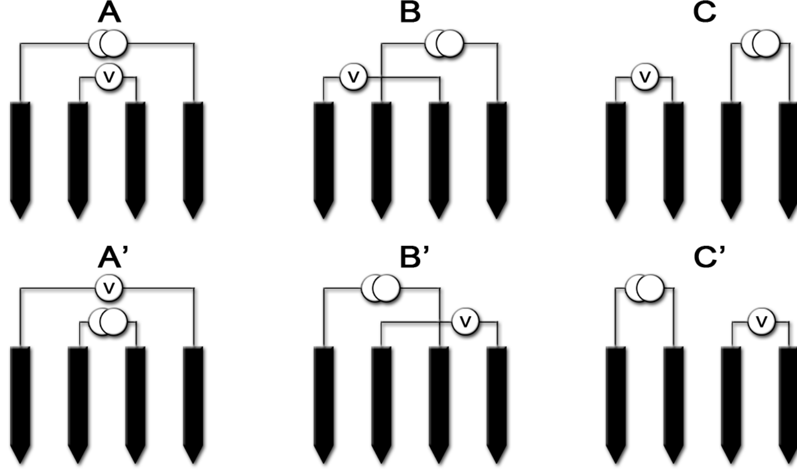

Figure 4.1: Configurations of current and voltage probes.

In the absence of a magnetic field, the following identities are valid; $R_A = R_{A'}$, $R_B = R_{B'}$ and $R_C = R_{C'}$, where R_i is the sheet resistance calculated from $R_i = \frac{V_i}{I}$, as indicated in Fig. 4.1.

For a point potential of ϕ_0 on a thin sample of infinite size (sample thickness much smaller than half probe spacing ($t << S/2$) [87]), the potential (ϕ) in a distance r is [88],

$$\phi - \phi_0 = -\frac{R_s I}{2\pi} \ln(r). \tag{4.1}$$

The potential from a dipole is then:

$$\phi - \phi_0 = \frac{R_s I}{2\pi} \ln\left(\frac{r_1}{r_2}\right), \tag{4.2}$$

where r_1 and r_2 is the distances to the poles. Considering a co-linear four-point probe with probe pitch s, and the dipole at the outer probes, the applied bias voltage between the center probes is:

$$V_A = \Delta\phi = \frac{R_s I}{2\pi}\left[\ln\left(\frac{2s}{s}\right) - \ln\left(\frac{s}{2s}\right)\right] \tag{4.3}$$

$$= R_s I \frac{\ln(4)}{2\pi} \approx \frac{1}{4.53} R_s I \tag{4.4}$$

where the factor 4.53 is called the correction factor (C_A) for configuration A, valid in the limit of an infinite two-dimensional sheet. Similarly, the correction factors for B and C configuration are found to be; $C_B = 5.72$ and $C_C = 22.84$ [88].

4.1.1 Errors

When performing micro-four point probe measurements, there are certain types of errors which can contribute to incorrect interpretation of the results. In the following, the position errors and the sample sensitivity is discussed.

Position errors

When placing the probes on the substrate, the contact positions may deviate from their ideal, equidistant positions. These contact point deviations are either in-line or off-line errors, as shown in Fig. 4.2. To compensate for in-line position errors, a dual measurement can be used, by first measure the A configuration followed by the B configuration [89]. This van-der Pauw like measurement strategy has been proven extremely useful in improving the accuracy with which micro four-point probe measurements can be carried out [87].

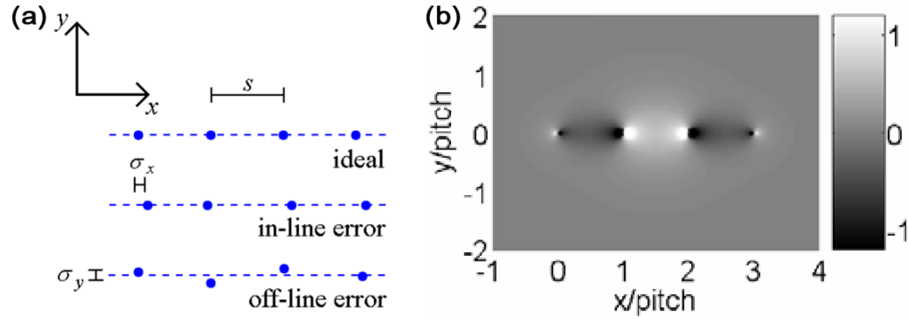

Figure 4.2: **(a)** In-line and off-line position errors using M4PP. From [90]. **(b)** M4PP resistance sensitivity. Notice the high sensitivity area near the probe contact positions at x=0,1,2,3. Fig. from [91].

Sample Sensitivity

Variations in the graphene sheet, such as defects, impurities, scratches or kinks give rise to different measured values for the resistance, depending on the placement of the probes. The sensitivity to such variations is shown in Fig. 4.2(b). The sensitivity goes to infinity at the probe positions, so any defects directly at the voltage probes will result in very unreliable measurements. This means that small changes in the probe position on the graphene flake may result in variations in the conductance. This has been observed by a simply disengage and reengage the probes.

4.2 Methods

This section will briefly describe the methods used for making four point probe measurements on graphene, specifically the probe fabrication and the measurement setup.

4.2.1 Probes

The probes for measurements were prefabricated using standard cleanroom techniques by the fabrication process described in [92]. The probes consist of SiO_2 with metal. As seen in Fig. 4.3a, the chips also include a strain gauge, although it was not used. The chips are glued to printed circuit boards (PCB), and zero insertion force (ZIF) connectors were used for easy switching of probes.

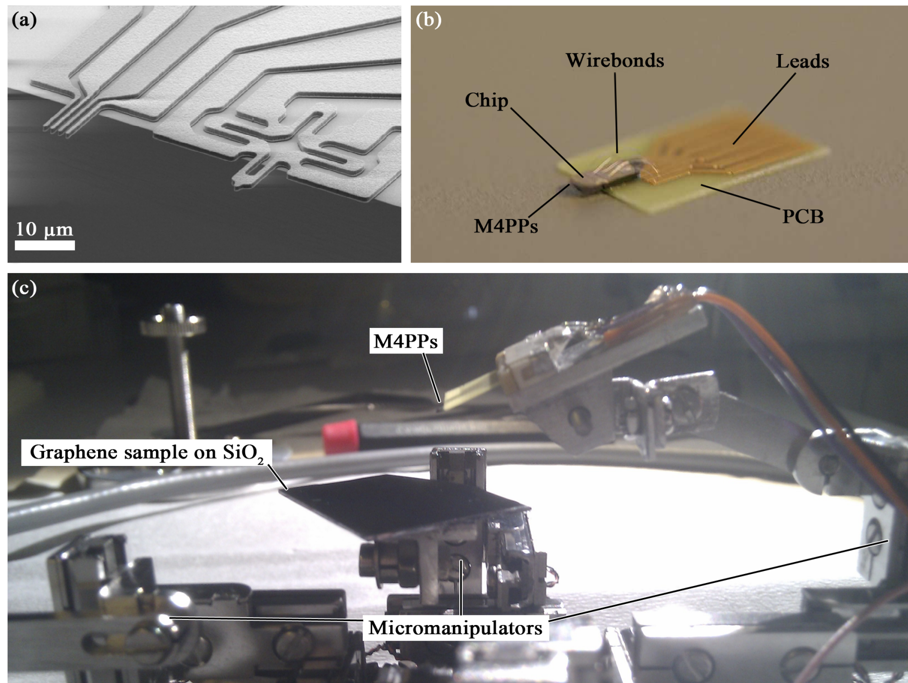

Figure 4.3: **(a)** SEM image of a M4PP used for measuring [20]. **(b)** Chip with probes glued and wirebonded to a ZIF PCB. **(c)** Graphene sample and M4PP mounted on a SmarAct micromanipulator.

4.3 Setup

In order to do M4PP measurements on graphene, a setup was built, which is sketched in Fig. 4.4.

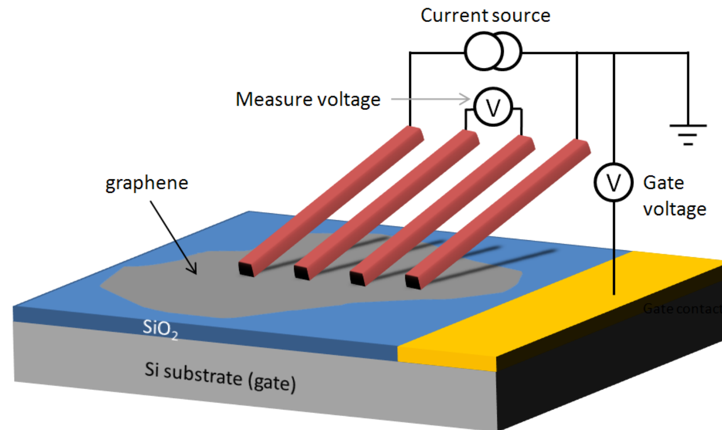

Figure 4.4: Schematic of measurements setup.

The DC current source is supplied by a Keithley 2400 sourcemeter, while a National Instruments Data Acquisition Card (DAQ) supplies the gate voltage and measures the voltage drop across the voltage probes. In order to obtain higher gate voltages, the gate voltage was amplified using a Falcon voltage amplifier. The setup was controlled with a laptop running LabView, and was designed for both ambient and vacuum measurements. For measurements in vacuum, the probes were mounted on a 13 axis SmarAct micromanipulator which was fitted inside a FEI Quanta 200 ESEM FEG environmental SEM. Measurements in ambient conditions were performed in using a Zeiss optical microscope for alignment of probes to sample.

For the reason of high gate sweep rate of up to 240 V/s (see section 5.1), all measurements are done in the A configuration unless otherwise stated.

4.4 Micro Four-Point Probes

The M4PP setup was made usable for both ambient conditions using an optical microscope, and for vacuum conditions inside a SEM. Different techniques were used for measuring and aligning probes wether measurements were done in ambient or vacuum.

4.4.1 Aligning and Approach

For measurements in vacuum, aligning of the sample and probes are performed on the SmartAct stage before placing the setup into the SEM. This is done in to insure the probes approach the sample from the intended direction, which cannot be changed once the chamber has been put under vacuum. In ambient, the sample can be gently rotated underneath lifted probes. The engage angle of the probes is set to 30°. If the probes are oriented wrongly with respect to the sample surface, there is a change that the four probe pins will not engage the surface simultaneously. This aligning is done by eye, and adjustments are made before re-engage.

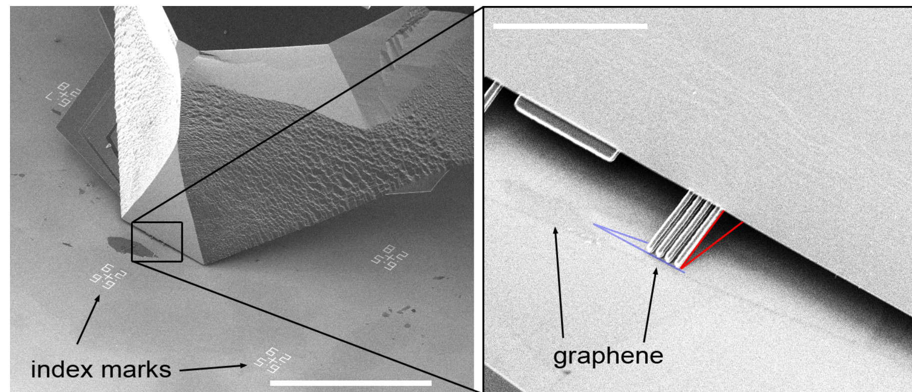

Figure 4.5: Aligning and contacting graphene samples in SEM. Alignment and rotation of probes needs to be precise for successful contact. Red lines indicates angle between M4PP and the surface, while the blue lines indicates the orientation between the probes and the graphene flake. Left scale bar is 400 μm, right is 20 μm.

Samples are located using the index marks, and the distance between the sample and the probes are estimated from the field of view of the microscope. For measurements in vacuum, the sample were placed just outside the field of view of the electron beam. Focusing and lens calibration is done in the visible region, and the probes are moved in after everything is ready. This was done in order to avoid damage and/or contamination on the surface from the electron beam, see section 5.2. In ambient, it is not an issue of aligning with the graphene flake

in the field of view.

Fig. 4.5 shows a tilted view of M4PP in contact with a single layer graphene in SEM.

4.4.2 Issues

Although M4PP allows for fast electrical or mechanical characterization of surfaces, there are issues which should be considered.

Mechanical contact between probes and a graphene flake has potential for scraping and creating holes, as seen in Fig. 4.6. White spots on graphene in SEM do not necessarily correspond to scraping damage. After SEM, optical images of the samples are recorded to confirm wether the features are due to scraping from the probes or not. A White spot is believed to be induced charges from the electrical measurements.

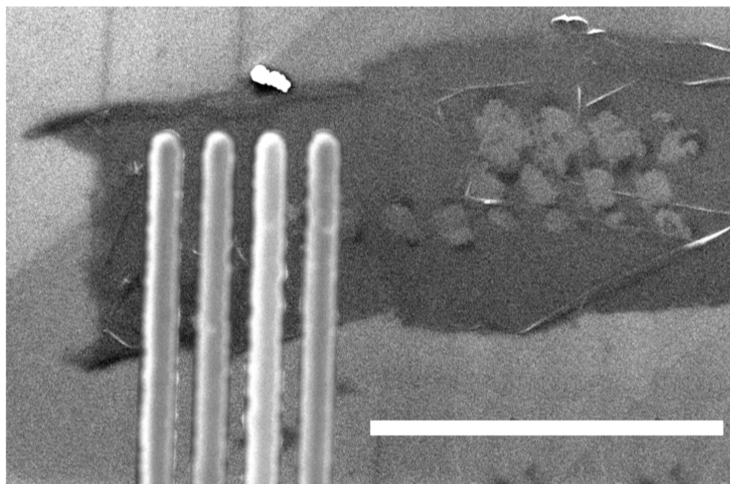

Figure 4.6: A high mechanical force from too large engagement depth can result in scraping and damage of the graphene flake. The scale bar is 10 μm.

When using M4PP, only very small engagement depth should be used to avoid scraping. Furthermore, stability and drift should be reduced as much as possible. A large source of drift was found to be the use of carbon tabs for sample adhesion and instability source included nearby traffic and other people in the building. This was reduced by working at nighttime. The possibility of using a different design of probes is discussed in section 4.6.

When measuring with M4PP, the very best measurements are achieved by making dual configuration measurements and multiple engages on the sample. However, due to stability, drift and vibrations, measuring on graphene was found to be most reliable by making a single engage and a fast measurement in a single configuration. This is discussed further in chapter 4.4.2.

Electrical breakdown in graphene can happen if the current density exceeds 10^8 A/cm^2 [36], which was observed with currents of 100 μA and higher. The contact point when using M4PP is approximately 100 nm and assuming a graphene thickness of 3.4 Angstrom, we calculate a current density through the perimeter of the assumed circular perimeter of the contact area of 10^7 A/cm^2, which correlates with breakdown current density in graphene [36]. Using M4PP, the current is kept below 10 μA to avoid electrical breakdown.

4.5 Electrical Characterization of Silver Nanowires

Conductive nanowires can interconnect with nanoelectronic devices [93,94], however contamination or oxidation of the bare metal nanowires can lead to degradation of the conductance of the wires. A simple and cheap method for fabrication of silver nanowires with a polyvinylpyrrolidone (PVP) cladding by direct electrospinning was shown by Song et al. [95]. The wires were characterized using the setup described in section 4.3, with extra care taken to align probes and wires. The wires are around 80 nm in diameter.

Fig. 4.7(a)-(b) shows the M4PP on a bare silver nanowire, and a wire with protective PVP cladding respectively. Fig. 4.7(c) shows the electrical measurements on silver nanowires, with and without PVP cladding. Measurements on the silver nanowires were performed as previously described, while measurements on PVP/Ag nanowires were done with greater care. Firstly, several engages were made to ensure minimal mechanical damage by the probes. Afterwards, higher and higher voltage sweeps were performed up to 50 mV.

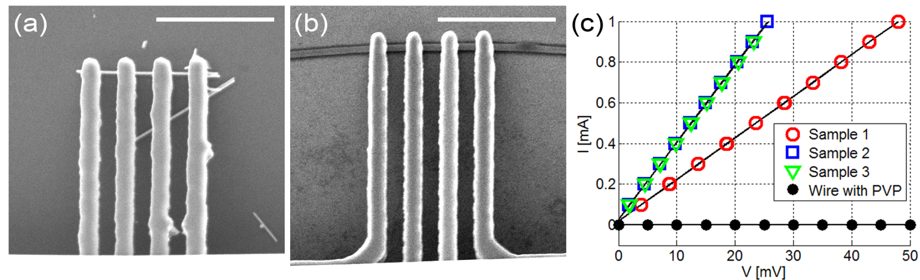

Figure 4.7: SEM images of bare silver nanowires **(a)** and nanowires with PVP cladding **(b)**. **(c)** Electrical characteristics of three different bare nanowires and silver nanowire with PVP cladding. No current can run through the cladding. Scale bar in **(a)**-**(b)** is 5 μm.

Conductivity of $0.3 - 0.5 \cdot 10^5$ S/cm of the bare silver nanowire, which is comparable to $0.8 \cdot 10^5$ S/cm measured by Xia et al. [96]. It was not possible to run a current through the cladding.

The results showed that a thin organic film is able to block the conductance measurements using M4PP, while other times, damages to graphene flakes were visible from mechanical contact.

4.6 Mechanical Impact on Vertical Nanowires

As was shown in section 4.4.2, the use of M4PP can lead to damage of the graphene sheet from the contact force during mechanical contact. Sometimes so severe that the sample is unmeasurable. The reason for the damage is the high mechanical rigidity of the cantilever in the longitudinal direction, compare to the two lateral directions. An L-shaped probe designed by Dirch Petersen [97] solved this by having the same spring constant in all three directions, enabling the probe to stay in static contact (ie. without scraping) despite vibrations, smaller translations and drift. Thee L-shaped was tested and compared to regular straight cantilevers on TiW coated nanograss. Fig. 4.8 shows the difference from mechanical contact between probes and nanograss.

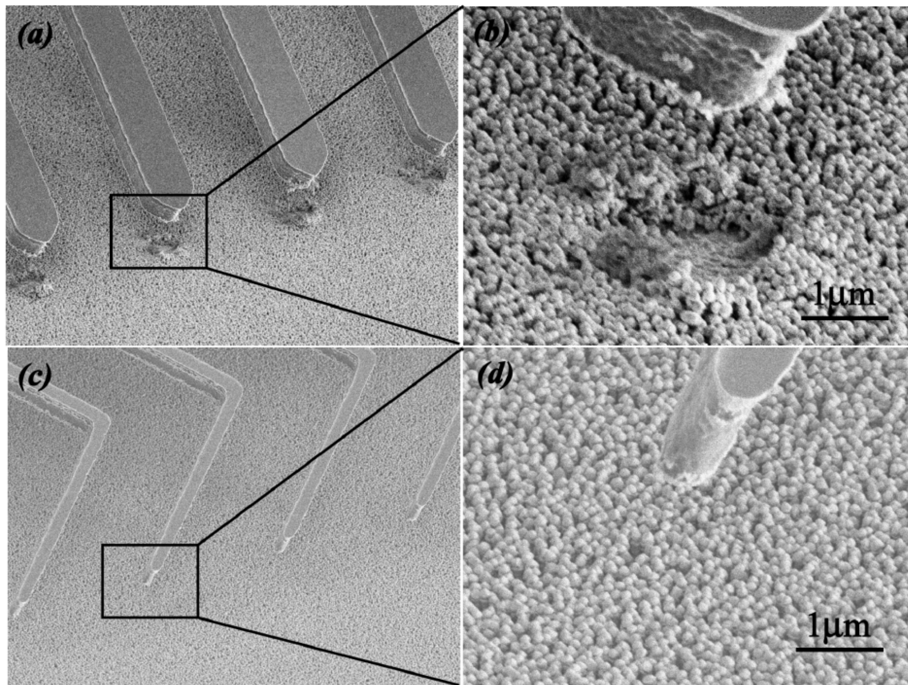

Figure 4.8: SEM images of cantilever engages on TiW nanograss. **(a)-(b)** Single engage using straight probes with an engage depth of 1-2 μm, which leaves marks of 1 μm. **(c)-(d)** Same experiment using L-shaped cantilever, which shows no visible damage to the nanograss.

Nanograss are made by deep reactive ion etching of silicon, followed by a sputtering of TiW. The probes are made 5 μm thick polysilison and coated with 10/200 nm Ti/Ni. Straight cantilever leaves marks in the nanograss and even contaminate the probes with the nanograss, with engage depths of 1-2 μm.

For the L-shaped cantilevers, even for high engage depths of 20 μm, a static contact is maintained to the nanograss, and no visible damage is observed upon disengage. The L-shaped cantilevers were fabricated with a pitch of 20 μm, and were therefore not small enough measurements on cleaved graphene. Such cantilevers, however, are being developed at DTU, with a pitch down to 1 μm.

4.7 Summary

This chapter presented the use of micro four-point probes, the electrical setup and issues when measuring on graphene and sensitive nanostructures. For sensitive samples, where damages from scraping, fast measurements are needed so vibrations and drift are minimized. The characterization setup and probes allows for measurements on 80 nm thick nanowires, and L-shaped cantilever probes proved with static contact to nanograss appears to be a highly usable tool for characterization.

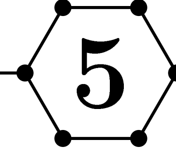

Hysteresis and Contamination

This chapter will present results arising from electrical characterization of graphene, namely the hysteresis effect and electron beam contamination.

5.1 Hysteresis in Graphene Field Effect

The field effect in graphene often show hysteresis, occuring in the difference in conductance depending on the sweep direction of the gate voltage. This has been previously observed for gating graphene [70–72, 98, 99]. The gate sweep performed in this thesis starts from zero voltage to a positive voltage, $+V$, to a negative of the same magnitude, $-V$ and back to zero. The position of the gate voltage at the CNP depends on the sweep direction, and hysteresis is defined as the difference in voltages at which charge neutrality appears.

The origin of the hysteresis is believed to be capacitive gating [100, 101] or by charge transfer with a liquid, usually water [70, 72, 102]. Charge trapping in the SiO_2 has been suggested [70–72, 98, 99, 101], which screens the graphene from the gate voltage. In this picture, the accumulated charge in the SiO_2 augments the applied gate voltage, creating a lower effective voltage.

To investigate the hysteresis dependence on the gate sweep rate, I used the setup describe in section 4.3, with M4PP in SEM. The gate sweep rate was varied between 0.4 V/s and 240 V/s, shown in Fig. 5.1.

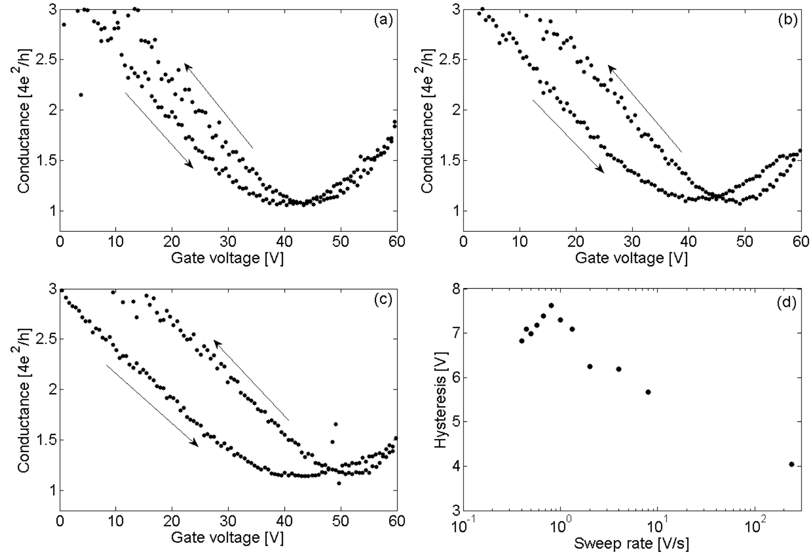

Figure 5.1: Hysteresis dependence on sweep rate of the gate. **(a)-(c)** Conductance for gate sweep rates of 240, 40 and 0.4 V/s respectively. **(d)** Hysteresis for different gate sweep rates.

In the simple picture of hysteresis, applying a voltage to the gate, the electric field traps or detraps charges with a specific rate, depending on sweep direction. At high sweep rates (sweep rate higher than the trapping rate), the traps does not have time to fill, before the direction is reversed. At very low sweep rates, a steady state is expected, meaning that the trapping or detrapping rates reaches zero before the next step in the gate voltage, and the hysteresis should approach a constant value, possibly zero.

Between the very high and very low gate sweep rates, we expect a maximum to occur, which is found at a gate sweep rate of around 0.8 V/s, as seen in Fig. 5.1d. The reason for 0.8 V/s is believed to be that for the fast sweep rates , the capacitance dominates, while for very slow sweep rates charge trapping dominates [72, 100]. The magnitude of the hysteresis is comparable to results obtained by Wang et al. [72], who measure a rate of 1.25 V/s.

5.2 Contamination and Irradiation

E-beam lithography and SEM/TEM investigation of graphene devices exposes the sample to an electron beam. The irradiation can introduce lattice damage and amorphisation of the graphene [77, 84, 102–104] or deposit contamination [105]. Many experiments have shown that irradiation on graphene will change

the electrical properties, typically by a n-doping effect [77,84,85,94,103,104,106].

To investigate the effects of e-beam irradiation, a graphene flake is contacted in SEM as described in section 4.4.1. To avoid irradiation of the sample, the graphene flake is positioned just outside the field of view of the microscope, and the M4PP is then placed on top. An initial measurement is made, followed by irradiation by shifting the beam. Fig. 5.2 shows a SEM image after irradiation.

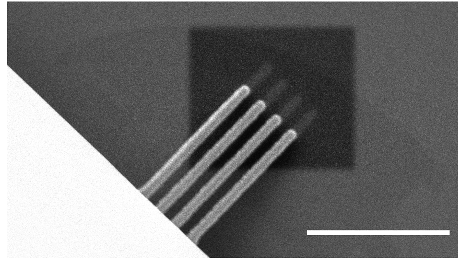

Figure 5.2: Visible effect of electron beam contamination with M4PP in contact. Sample exposed in a rectangular area (dark). After exposure the position of M4PP is observed as light areas. Scale bar is 10 μm.

From the SEM image, it can be seen that the probes shadows the e-beam at the probe position. Measurements are done every 5 minutes. The measurements are shown in Fig.. 5.3.

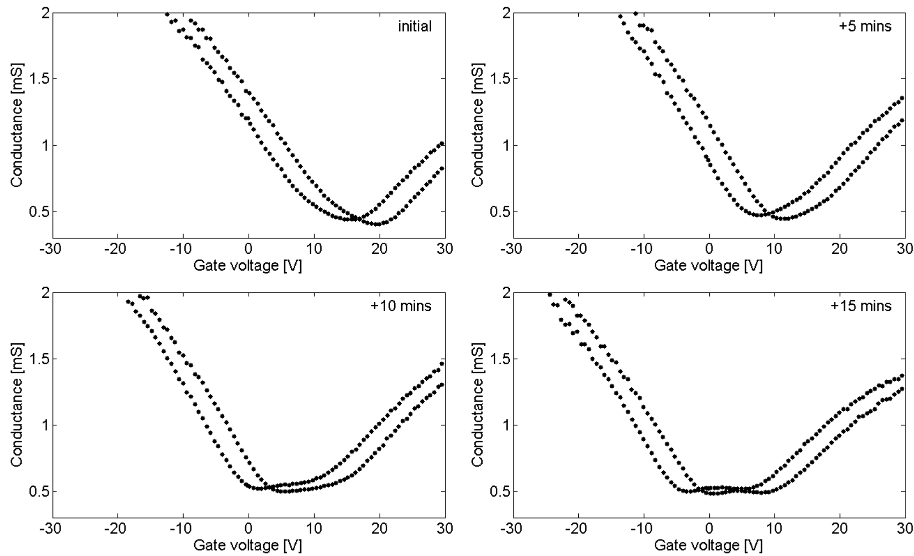

Figure 5.3: Effect of e-beam exposure of graphene sample for initial sample and 5, 10 and 15 mins of e-beam irradiation.

5.2.1 Splitting of the Charge Neutrality Point

As the irradiation dose is increased, a n-doping effect is observed. Furthermore, a splitting of the CNP is seen. This is contributed to the shadowing effect of the M4PP, which effectively creates two different areas, which are measured simultaneously. From Fig. 4.2b it is also seen that the probes shadow some of the high sensitivity area for M4PP measurements.

Other groups [77,84,102–104] argue the irradiation create lattice damage, however, their results are based on Raman spectroscopy, which shows a D-peak after irradiation. This D-peak will be present for both lattice damage and amorphous carbon deposition [107,108], and since the acceleration voltage was set to 5 keV, well below the threshold for knock-on damage of 86 keV [109], it is believed the doping effect is due to contamination, as also observed by Liu et al. [105].

5.3 Summary

Hysteresis and irradiation effects on electrical characterization of graphene devices were discussed here. Hysteresis can arise from charge trapping and detrapping with the gate insulator, which here was shown to be dependent on the gate sweep rate, with a hysteresis maximum at 0.8 V/s. Contamination of graphene showed a n-doping effect, which is attributed to amorphous carbon contamination during irradiation.

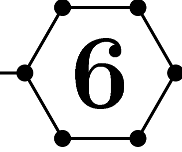

Nanopatterned Graphene

This chapter presents and discusses results obtained from nanostructuring graphene with an antidot lattice using electron beam lithography. The devices consists of a Hall bar structure with multielectrodes for characterization of different sections of increasing amounts of patterning.

6.1 Raman Analysis

Raman spectroscopy of the final devices were done as described in section 3.2, and Fig. 6.1 shows a SEM image and Raman maps of the D peak/G peak (Fig. 6.1b) and the 2D peak/G peak (Fig. 6.1c) ratios.

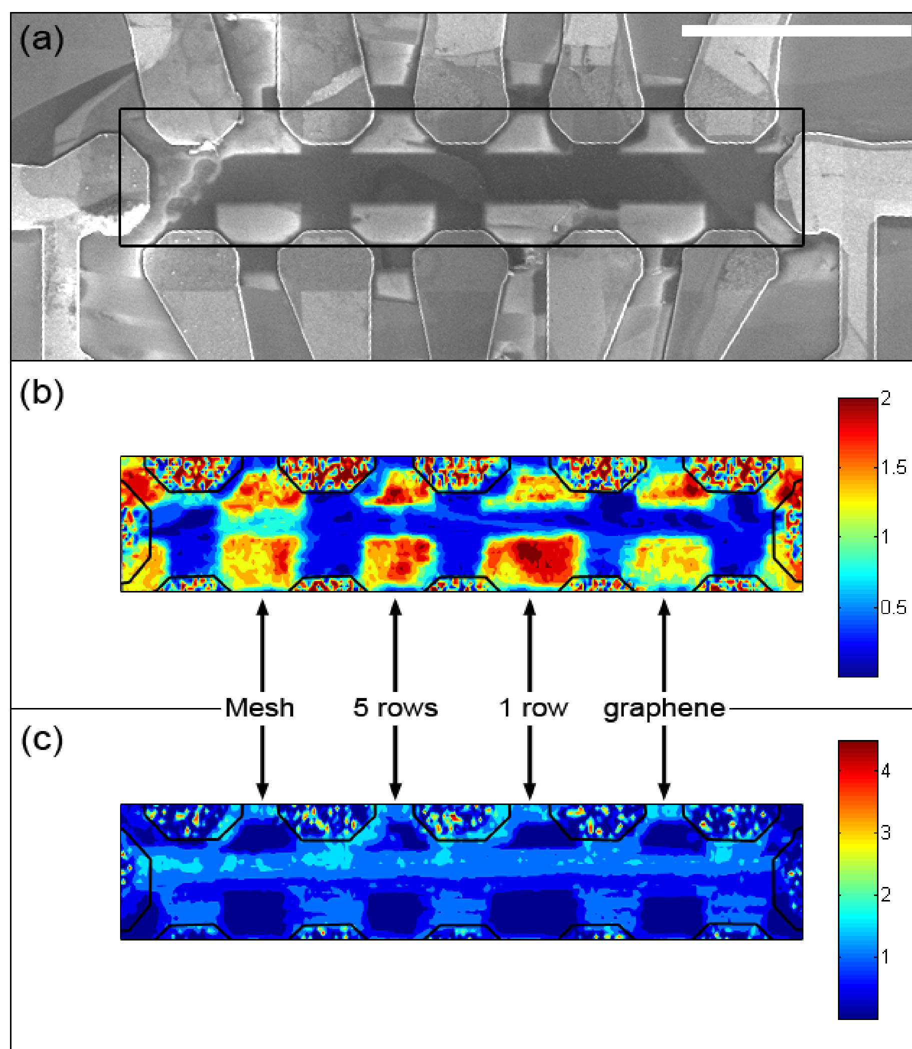

Figure 6.1: **(a)** SEM image of final device G. Although difficult to see, the sections are mesh, 5 rows, 1 row and graphene left to right respectively. Black rectangle defines the area of the Raman map. **(b)-(c)** D/G and 2D/G ratios of peak intensities respectively. Black outlines indicates position of metal electrodes.

Fig. 6.1(a) is a SEM image of device G after measurements, and Fig. 6.2 shows the mesh section, with 50 nm holes. The D/G ratio shown in 6.1(b) shows an increase in defects in the nanostructured sections due to the fabricated holes, while the 2D/G indicates single layer graphene.

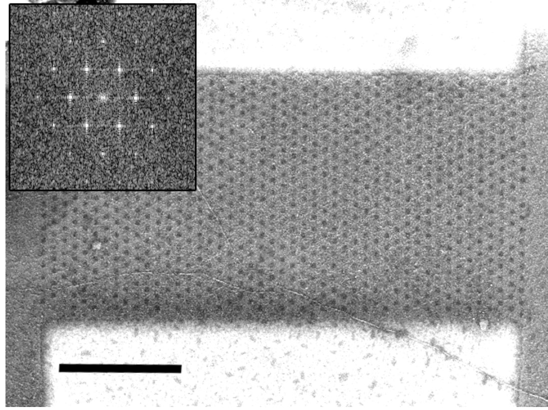

Figure 6.2: Antidots in graphene Hall bar. Hole diameters is 50 nm with a pitch of 100 nm. Inset shows the Fourier transform of the mesh. Scale bar is 1 μm.

6.2 Variations in Number of Rows

Electrical measurements are performed on the sample in Fig. 6.1, using the setup described in section 3.7. No data was collected for the 5 rows section because no functional electrodes were found in device G. Fig. 6.3 and Fig. 6.4 shows gate sweeps for graphene, 1 row and complete mesh.

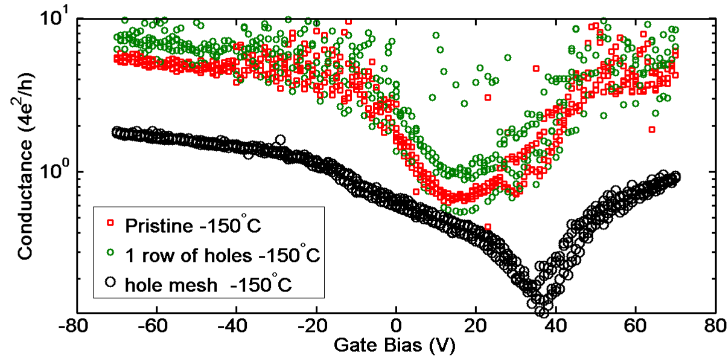

Figure 6.3: Gate sweeps for Hall bar sections of graphene, 1 row and a complete mesh at -150^oC.

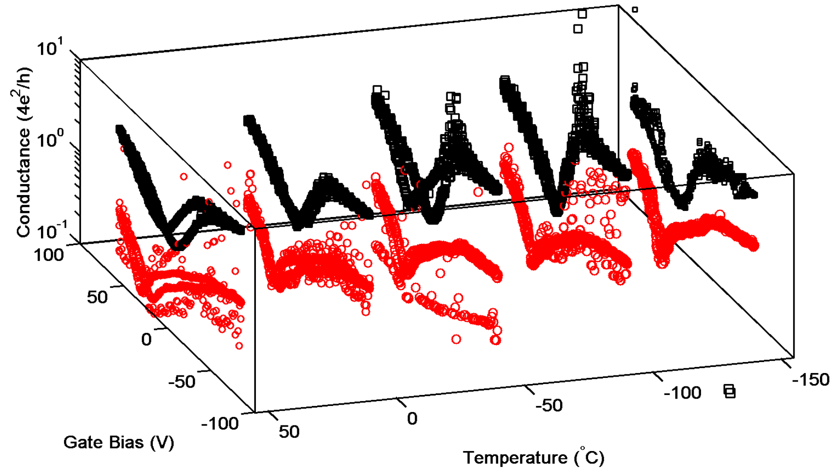

Figure 6.4: Conductance for varying gate voltages and temperatures for the pristine section (black squares) and the mesh section (red circles).

The gate sweep for the pristine graphene and a single row are very similar, whereas the conductance for the mesh is lower. The small difference is conductance between pristine graphene and a single row can be an effect of the e-beam lithography performed on the single row, resulting in a small increase in conductance. During characterization however, a single row was not observable in Raman or SEM. The resolution of the Raman map may not have been high enough to observed disorder from a single row, and contamination of the sample did not allow for a confirmation using SEM.

Since there is no difference between pristine graphene and a single row, it indicates that multiple rows are necessary to alter the electronic properties. The reason is most likely that either the neck width between the holes are too large for any electron confinement to occur, or that a single row does not increase the number of scattering event sufficient for altering of the electrical properties.

Bai et al. [42] (Fig. 2.7) showed a field effect in graphene antidot lattice fabricated with block copolymer lithography. Their devices have neck widths of 7-15 nm, which resulted in on-off ratios of around 10. Furthermore, their result indicate a reduction in conductance with decreasing neck widths. Fig. 6.3 also shows a reduced in conductance of the mesh compared to the pristine graphene, however, there is no on-off ratio for the mesh section of the Hall bar. This indicates that the antidot lattice with 50 nm neck widths does reduce conductance with a factor of around 10, comparable to the results from Bai et al., but the neck width is not adequate for defining an on-off ratio.

Fig. 6.4 shows the gate sweep for the pristine graphene and the mesh for temperatures between -150°C - +50°C. The hysteresis decreases with decreasing temperature. This is also shown in Fig. 6.5. As discussed previously, hysteresis in graphene is due to capacitive gating effects or charge transfer between the graphene and water on the surface. If water molecules are mobile on the graphene surface, a reduction in temperature will freeze the water and be frozen in place. At high temperature the charges can move in-line with the gate voltage and effect hysteresis, but at lower temperatures, the charges are localized in the ice, resulting in less hysteresis.

The temperature dependence on the hysteresis has also been observed by other groups [72, 110], and the suppression of trapping rates is attributed to ice on graphene exhibits a stronger dipole moment than water, which also agrees with theory [111].

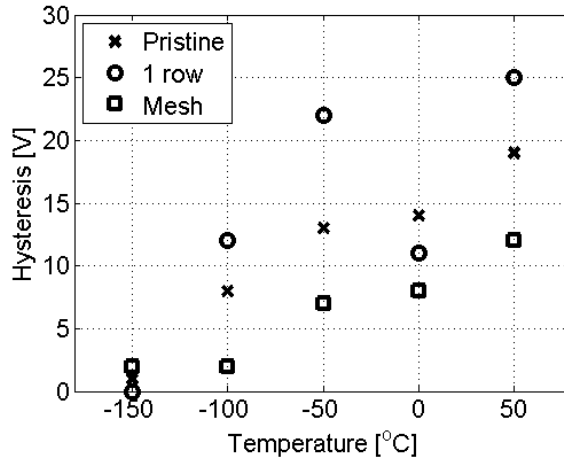

Figure 6.5: Hysteresis dependence on temperature on sample G.

6.2.1 Band gap in Antidot Lattice

To investigate if the antidot lattice show any indication of a band gap, gate sweeps on the different sections are performed at temperatures in the range -150°C - +50°C. As described in section 2.2.2, the conductance will increase with increasing temperature in the presence of a band gap. The minimum sheet conductance at the CNP for graphene, a single row and for five rows is shown in Fig. 6.6.

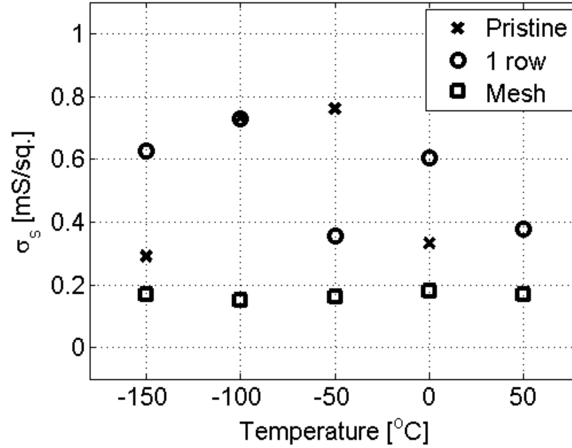

Figure 6.6: Sheet conductance at CNP for different hall bar sections and at various temperatures. No increase in conductance with decrease in temperature indicates that these sections does not have a band gap.

There is no clear tendency of a temperature dependence on the conductance, which indicates no band gap is present in either sections of the Hall bar. This is most likely due to the hole size of 50 nm and pitch of 100 nm is not small enough for band gap opening, consisting with [51]. With these parameters, the neck width of graphene between the holes are 50 nm, which is not small enough for electron confinement. Devices with hole diameters down to 20 nm and pitch of 40 nm were designed and fabricated, however final devices were either missing electrical connections, had leakage current to the gate or damages to the graphene during processing.

The conductance of the CNP varies between 0.2 mS for the mesh, and up to 0.8 mS for the pristine graphene and single row sections. From literature, the conductance through an antidot lattice at room temperature of neck width of around 7 nm is reported to be around 0.01 mS [17] and 0.1 mS [42], which correlate well with ours, considering our neck widths are 50 nm. Graphene nanoribbons by Han et al. [39], measures conductances of 0.08 mS for graphene nanoribbons of 50 nm widths. This is about half of our measurements on sample G of 0.2 mS (Fig. 6.6). Han et al. [39] also measures very low temperature dependence on the conductance in the range 50-300 K, similar to our measurements.

From the gate sweep, the carrier mobility for the different sections are calculated from equation 2.4, and shown in Fig.. 6.7.

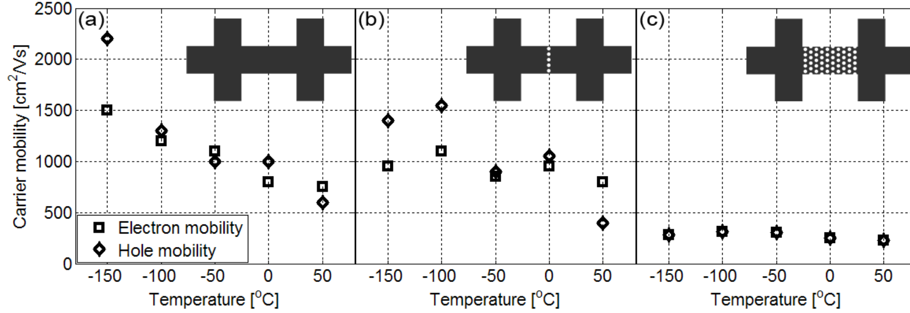

Figure 6.7: Carrier mobility for different sections at various temperatures. General trend is a reduction in carrier mobility with increasing defects in the graphene.

The carrier mobility deceases as the number of rows increases, which is due to the increase in defect density and thereby a decrease in the mean free path. Safron et al. [17] has reported fabrication of graphene antidot lattice using colloidal lithography with neck widths down to 6.9 nm, and measured the carrier mobility to be around 1 cm^2/Vs. The measured carrier mobility in Fig. 6.7c is around 300 cm^2/Vs for the antidot lattice, but does have a larger neck width of 50 nm.

The increase in mobility for pristine graphene has also been observed by Zhu et al. [112], where an increase of around 30% in carrier mobility in the temperature range of -150°C - +50°C. The results in Fig. 6.7a shows a doubling in mobility from around 750 cm^2/Vs to 1500 cm^2/Vs. The increase in carrier mobility is contribute to lower phonon scattering at lower temperatures [113,114], which is only present for the pristine and single row graphene. For the antidot lattice, the mobility is limited by defect scattering from the holes [115].

6.3 Summary

This chapter presented result of electrical characterization of multielectrode graphene devices. The devices were made with electron beam lithography, and with varying number of rows of holes. The conductance and carrier mobility decreases for the antidot lattice compared to pristine graphene, however the electrical measurements dependence on temperature suggests that the hole size of 50 nm are not small enough for creating a band gap, although for a single row (if present) the mobility is unaffected.

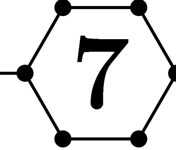

Conclusions

Characterization of graphene and other nanostructures were performed in this project. The micro four-point probe technique allows for fast and reliable characterization of graphene devices, but also for very sensitive nanostructure. It was shown that micro four-point probe could be used for electrical characterization of silver nanowires with a thickness of 80 nm, however the use of straight cantilevers could in some cases damage sensitive surfaces, such as graphene and nanograss. A solution is to use flexible L-shaped cantilever, which remains in static contact during small vibrations, translations and drift. Even at very high engagement depths of up to 20 μm, the cantilevers did not exhibit damage to TiW nanograss, and remained in static contact, compared to straight cantilevers, which showed visible scraping damage for an engagement of 1-2 μm.

Graphene devices were characterized in-situ SEM for determining the hysteresis effects, which shows a dependence on the gate sweep rate. The hysteresis has a maximum at a gate sweep rate of 0.8 V/s, which arises from a balance between the capacitance and the charge trapping rates. The hysteresis effect was also shown to be highly depended on temperature, which almost vanished at -150°C, which is attributed to a suppression of the trapping rates due to stronger dipole moments in ice, compared to water.

Graphene devices with antidot lattices with varying number of rows were fabricated using standard electron beam lithography, with a hole diameter of 50 nm. The multielectrode devices were made from a single micromechanical cleaved graphene flake with different sections, each with increasing number of rows of holes. The electrical measurements showed no difference between pristine graphene and a single row, however it was not possible to confirm that the single row was actually present in the device through Raman spectroscopy or scanning electron microscopy. A clear distinction was visible in the carrier mobility between pristine graphene and a perforated antidot mesh in the graphene flake. For pristine graphene, the carrier mobility varied with temperature from around 750 cm^2/Vs at 50°C to around 1500 cm^2/Vs at -150°C, while the carrier mobility for the mesh was constant with temperature, at around 300 cm^2/Vs.

The conductance of the different sections proved to be unaffected by temperature, which leads to believe that no band gap is present in the antidot lattices. This is most likely due to the size of the holes and the neck width of 50 nm being to large for electron confinement.

This project investigated graphene devices with hole size down to 50 nm, but it is believed that smaller holes potentially could produce devices with an observable band gap using the same fabrication and characterization methods as described here. Fabrication of smaller holes could be done with optimization of the electron beam lithography parameters, or by using a controlled over etching of the PMMA mask and underlying graphene.

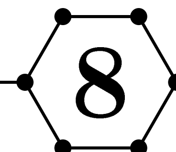

References

[1] Frank Schwierz. Graphene transistors. *Nature Nanotechnology*, 5(7):487–496, JUL 2010 2010.

[2] K. S. Novoselov, V. I. Fal'ko, L. Colombo, P. R. Gellert, M. G. Schwab, and K. Kim. A roadmap for graphene. *Nature*, 490(7419), 2012-Oct-11 2012.

[3] P. Norton, T. Braggins, and Levinste.H. Impurity and lattice scattering parameters as determined from hall and mobility analysis in n-type silicon. *Physical Review B*, 8(12):5632–5653, 1973 1973.

[4] V. I. Fistul, M. I. Iglitsyn, and E. M. Omelyanovskii. Mobility of electrons in germanium strongly doped with arsenic. *Soviet Physics-Solid State*, 4(4):784–785, 1962 1962.

[5] C. Jacoboni, F. Nava, C. Canali, and G. Ottaviani. Electron-drift velocity and diffusivity in germanium. *Physical Review B*, 24(2):1014–1026, 1981 1981.

[6] S. C. Jain and D. J. Roulston. A simple expression for band-gap narrowing (bgn) in heavily doped si, ge, gaas and gexsi1-x strained layers. *Solid-State Electronics*, 34(5):453–465, MAY 1991 1991.

[7] J. S. Blakemore. Semiconducting and other major properties of gallium-arsenide. *Journal of Applied Physics*, 53(10):R123–R181, 1982 1982.

[8] V. V. Karataev, M. G. Milvidskii, N. S. Rytova, and V. I. Fistul. Compensation in n-type inas. *Soviet Physics Semiconductors-Ussr*, 11(9):1009–1011, 1977 1977.

[9] Z. M. Fang, K. Y. Ma, D. H. Jaw, R. M. Cohen, and G. B. Stringfellow. Photoluminescence of insb, inas, and inassb grown by organometallic

vapor-phase epitaxy. *Journal of Applied Physics*, 67(11):7034–7039, JUN 1 1990 1990.

[10] T. Durkop, S. A. Getty, E. Cobas, and M. S. Fuhrer. Extraordinary mobility in semiconducting carbon nanotubes. *Nano Letters*, 4(1):35–39, JAN 2004 2004.

[11] K. S. Novoselov, A. K. Geim, S. V. Morozov, D. Jiang, M. I. Katsnelson, I. V. Grigorieva, S. V. Dubonos, and A. A. Firsov. Two-dimensional gas of massless dirac fermions in graphene. *Nature*, 438(7065):197–200, NOV 10 2005 2005.

[12] K. I. Bolotin, K. J. Sikes, Z. Jiang, M. Klima, G. Fudenberg, J. Hone, P. Kim, and H. L. Stormer. Ultrahigh electron mobility in suspended graphene rid e-1879-2011. *Solid State Communications*, 146(9-10):351–355, JUN 2008.

[13] K. S. Novoselov, A. K. Geim, S. V. Morozov, D. Jiang, Y. Zhang, S. V. Dubonos, I. V. Grigorieva, and A. A. Firsov. Electric field effect in atomically thin carbon films. *Science*, 306(5696):666–669, OCT 22 2004 2004.

[14] H. P. Boehm, R. Setton, and E. Stumpp. Nomenclature and terminology of graphite-intercalation compounds (iupac recommendations 1994). *Pure and Applied Chemistry*, 66(9):1893–1901, SEP 1994 1994.

[15] A. K. Geim and K. S. Novoselov. The rise of graphene. *Nature Materials*, 6(3):183–191, MAR 2007 2007.

[16] Richard Balog, Bjarke Jorgensen, Louis Nilsson, Mie Andersen, Emile Rienks, Marco Bianchi, Mattia Fanetti, Erik Laegsgaard, Alessandro Baraldi, Silvano Lizzit, Zeljko Sljivancanin, Flemming Besenbacher, Bjork Hammer, Thomas G. Pedersen, Philip Hofmann, and Liv Hornekaer. Bandgap opening in graphene induced by patterned hydrogen adsorption. *Nature Materials*, 9(4):315–319, APR 2010 2010.

[17] Nathaniel S. Safron, Adam S. Brewer, and Michael S. Arnold. Semiconducting two-dimensional graphene nanoconstriction arrays. *Small*, 7(4):492–498, FEB 18 2011 2011.

[18] Yuanbo Zhang, Tsung-Ta Tang, Caglar Girit, Zhao Hao, Michael C. Martin, Alex Zettl, Michael F. Crommie, Y. Ron Shen, and Feng Wang. Direct observation of a widely tunable bandgap in bilayer graphene. *Nature*, 459(7248):820–823, JUN 11 2009 2009.

[19] Katherine Bourzac. Electronics back to analogue. *Nature*, 483(7389), MAR 15 2012 2012.

[20] Dirch H. Petersen, Ole Hansen, Torben M. Hansen, Peter Boggild, Rong Lin, Daniel Kjaer, Peter F. Nielsen, Trudo Clarysse, Wilfried Vandervorst, Erik Rosseel, Nick S. Bennett, and Nick E. B. Cowern. Review of electrical

characterization of ultra-shallow junctions with micro four-point probes. *Journal of Vacuum Science & Technology B*, 28(1):C1C27–C1C33, JAN 2010 2010.

[21] B. Obradovic, R. Kotlyar, F. Heinz, P. Matagne, T. Rakshit, M. D. Giles, M. A. Stettler, and D. E. Nikonov. Analysis of graphene nanoribbons as a channel material for field-effect transistors. *Applied Physics Letters*, 88(14):142102, APR 3 2006 2006.

[22] T. R. Robinson. On klein tunneling in graphene. *American Journal of Physics*, 80(2), FEB 2012 2012.

[23] H. G. Zhang, H. Hu, Y. Pan, J. H. Mao, M. Gao, H. M. Guo, S. X. Du, T. Greber, and H. J Gao. Graphene based quantum dots (vol 22, 302001, 2010). *Journal of Physics-Condensed Matter*, 22(39):389802, OCT 6 2010 2010.

[24] P. R. Wallace. The band theory of graphite. *Physical Review*, 71(9):622–634, 1947 1947.

[25] C. Attaccalite, A. Grueneis, T. Pichler, and A. Rubio. Ab-initio band structure of doped graphene. *arXiv:0808.0786 [cond-mat.mes-hall]*, 2008.

[26] S. Reich, J. Maultzsch, C. Thomsen, and P. Ordejon. Tight-binding description of graphene. *Physical Review B*, 66(3):035412, JUL 15 2002 2002.

[27] J. C Charlier, P. C. Eklund, J. Zhu, and A. C. Ferrari. Electron and phonon properties of graphene: Their relationship with carbon nanotubes. *Carbon Nanotubes: Advanced Topics in the Synthesis, Structure, Properties and Applications*, 111:673–709, 2008 2008.

[28] Marvin Cohen and James Chelikowsky. *Electronic Structure and Optical Properties of Semiconductors*. Springer; 1 edition, 1988.

[29] Jian-Hao Chen, Chaun Jang, Shudong Xiao, Masa Ishigami, and Michael S. Fuhrer. Intrinsic and extrinsic performance limits of graphene devices on sio2. *Nature Nanotechnology*, 3(4):206–209, APR 2008.

[30] Akin Akturk and Neil Goldsman. Electron transport and full-band electron-phonon interactions in graphene. *Journal of Applied Physics*, 103(5):053702, MAR 1 2008 2008.

[31] Nikolaos Tombros, Alina Veligura, Juliane Junesch, J. Jasper van den Berg, Paul J. Zomer, Magdalena Wojtaszek, Ivan J. Vera Marun, Harry T. Jonkman, and Bart J. van Wees. Large yield production of high mobility freely suspended graphene electronic devices on a polydimethylglutarimide based organic polymer. *Journal of Applied Physics*, 109(9):093702, MAY 1 2011 2011.

[32] S. Das Sarma, Shaffique Adam, E. H. Hwang, and Enrico Rossi. Electronic transport in two-dimensional graphene. *Reviews of Modern Physics*, 83(2), MAY 16 2011 2011.

[33] J. Martin, N. Akerman, G. Ulbricht, T. Lohmann, J. H. Smet, K. Von Klitzing, and A. Yacoby. Observation of electron-hole puddles in graphene using a scanning single-electron transistor. *Nature Physics*, 4(2):144–148, FEB 2008 2008.

[34] Jannik C. Meyer, A. K. Geim, M. I. Katsnelson, K. S. Novoselov, T. J. Booth, and S. Roth. The structure of suspended graphene sheets. *Nature*, 446(7131):60–63, MAR 1 2007 2007.

[35] Toshiaki Kato and Rikizo Hatakeyama. Site- and alignment-controlled growth of graphene nanoribbons from nickel nanobars. *Nature nanotechnology*, 7(10), 2012-Sep-9 2012.

[36] Raghunath Murali, Yinxiao Yang, Kevin Brenner, Thomas Beck, and James D. Meindl. Breakdown current density of graphene nanoribbons. *Applied Physics Letters*, 94(24):243114, JUN 15 2009.

[37] Lei Liu, Yingli Zhang, Wenlong Wang, Changzhi Gu, Xuedong Bai, and Enge Wang. Nanosphere lithography for the fabrication of ultranarrow graphene nanoribbons and on- chip bandgap tuning of graphene. *Advanced Materials*, 23(10):1246–+, MAR 2011 2011.

[38] Melinda Y. Han, Juliana C. Brant, and Philip Kim. Electron transport in disordered graphene nanoribbons. *Physical Review Letters*, 104(5):056801, FEB 5 2010 2010.

[39] Melinda Y. Han, Barbaros Oezyilmaz, Yuanbo Zhang, and Philip Kim. Energy band-gap engineering of graphene nanoribbons. *Physical Review Letters*, 98(20):206805, MAY 18 2007 2007.

[40] Young-Woo Son, Marvin L. Cohen, and Steven G. Louie. Energy gaps in graphene nanoribbons. *Physical Review Letters*, 97(21):216803, NOV 24 2006 2006.

[41] Xiaogan Liang, Yeon-Sik Jung, Shiwei Wu, Ariel Ismach, Deirdre L. Olynick, Stefano Cabrini, and Jeffrey Bokor. Formation of bandgap and subbands in graphene nanomeshes with sub-10 nm ribbon width fabricated via nanoimprint lithography. *Nano Letters*, 10(7), JUL 2010 2010.

[42] Jingwei Bai, Xing Zhong, Shan Jiang, Yu Huang, and Xiangfeng Duan. Graphene nanomesh. *Nature Nanotechnology*, 5(3):190–194, MAR 2010 2010.

[43] Jinming Cai, Pascal Ruffieux, Rached Jaafar, Marco Bieri, Thomas Braun, Stephan Blankenburg, Matthias Muoth, Ari P. Seitsonen, Moussa Saleh, Xinliang Feng, Klaus Muellen, and Roman Fasel. Atomically precise

bottom-up fabrication of graphene nanoribbons. *Nature*, 466(7305), JUL 22 2010 2010.

[44] S. Y. Zhou, G. H Gweon, A. V. Fedorov, P. N. First, W. A. De Heer, D. H Lee, F. Guinea, A. H. Castro Neto, and A. Lanzara. Substrate-induced bandgap opening in epitaxial graphene. *Nature Materials*, 6(10), OCT 2007 2007.

[45] Seunghun Hong and Sung Myung. Nanotube electronics - a flexible approach to mobility. *Nature Nanotechnology*, 2(4):207–208, APR 2007 2007.

[46] Young-Woo Son, Marvin L. Cohen, and Steven G. Louie. Energy gaps in graphene nanoribbons. *Physical Review Letters*, 97(21):216803, NOV 24 2006 2006.

[47] Veronica Barone, Oded Hod, and Gustavo E. Scuseria. Electronic structure and stability of semiconducting graphene nanoribbons. *Nano Letters*, 6(12):2748–2754, DEC 13 2006 2006.

[48] Youngki Yoon and Jing Guo. Effect of edge roughness in graphene nanoribbon transistors. *Applied Physics Letters*, 91(7):073103, AUG 13 2007 2007.

[49] J. Jung, T. Pereg-Barnea, and A. H. MacDonald. Theory of interedge superexchange in zigzag edge magnetism. *Physical Review Letters*, 102(22):227205, JUN 5 2009 2009.

[50] Xiaolin Li, Xinran Wang, Li Zhang, Sangwon Lee, and Hongjie Dai. Chemically derived, ultrasmooth graphene nanoribbon semiconductors. *Science*, 319(5867), FEB 29 2008 2008.

[51] Thomas G. Pedersen, Christian Flindt, Jesper Pedersen, Niels Asger Mortensen, Antti-Pekka Jauho, and Kjeld Pedersen. Graphene antidot lattices: Designed defects and spin qubits. *Physical Review Letters*, 100(13):136804, APR 4 2008 2008.

[52] M. Sikka, N. Singh, A. Karim, F. S. Bates, S. K. Satija, and C. F. Majkrzak. Entropy-driven surface segregation in block copolymer melts. *Physical Review Letters*, 70(3), JAN 18 1993 1993.

[53] Alexander Sinitskii and James M. Tour. Patterning graphene through the self-assembled templates: Toward periodic two-dimensional graphene nanostructures with semiconductor properties. *Journal of the American Chemical Society*, 132(42):14730–14732, OCT 27 2010 2010.

[54] Jesper Goor Pedersen and Thomas Garm Pedersen. Band gaps in graphene via periodic electrostatic gating. *Physical Review B*, 85(23):235432, JUN 14 2012.

[55] Xuesong Li, Weiwei Cai, Jinho An, Seyoung Kim, Junghyo Nah, Dongxing Yang, Richard Piner, Aruna Velamakanni, Inhwa Jung, Emanuel Tutuc, Sanjay K. Banerjee, Luigi Colombo, and Rodney S. Ruoff. Large-area synthesis of high-quality and uniform graphene films on copper foils. *Science*, 324(5932):1312–1314, JUN 5 2009 2009.

[56] Sukang Bae, Hyeongkeun Kim, Youngbin Lee, Xiangfan Xu, Jae-Sung Park, Yi Zheng, Jayakumar Balakrishnan, Tian Lei, Hye Ri Kim, Young Il Song, Young-Jin Kim, Kwang S. Kim, Barbaros Ozyilmaz, Jong-Hyun Ahn, Byung Hee Hong, and Sumio Iijima. Roll-to-roll production of 30-inch graphene films for transparent electrodes. *Nature Nanotechnology*, 5(8):574–578, AUG 2010 2010.

[57] Daniel R. Lenski and Michael S. Fuhrer. Raman and optical characterization of multilayer turbostratic graphene grown via chemical vapor deposition. *Journal of Applied Physics*, 110(1):013720, JUL 1 2011 2011.

[58] Taisuke Ohta, Aaron Bostwick, J. L. McChesney, Thomas Seyller, Karsten Horn, and Eli Rotenberg. Interlayer interaction and electronic screening in multilayer graphene investigated with angle-resolved photoemission spectroscopy. *Physical Review Letters*, 98(20):206802, MAY 18 2007 2007.

[59] Aaron Bostwick, Taisuke Ohta, Jessica L. McChesney, Konstantin V. Emtsev, Thomas Seyller, Karsten Horn, and Eli Rotenberg. Symmetry breaking in few layer graphene films. *New Journal of Physics*, 9:385, OCT 31 2007 2007.

[60] S. Y. Zhou, G. H Gweon, J. Graf, A. V. Fedorov, C. D. Spataru, R. D. Diehl, Y. Kopelevich, D. H Lee, Steven G. Louie, and A. Lanzara. First direct observation of dirac fermions in graphite. *Nature Physics*, 2(9):595–599, SEP 2006 2006.

[61] H. P. Boehm, A. Clauss, U. Hofmann, and G. O. Fischer. Dunnste kohlenstoff-folien. *Zeitschrift Fur Naturforschung Part B-Chemie Biochemie Biophysik Biologie Und Verwandten Gebiete*, B 17(3):150–&, 1962 1962.

[62] Varrla Eswaraiah, Sasidharannair Sasikaladevi Jyothirmayee Aravind, and Sundara Ramaprabhu. Top down method for synthesis of highly conducting graphene by exfoliation of graphite oxide using focused solar radiation. *Journal of Materials Chemistry*, 21(19):6800–6803, 2011 2011.

[63] Maher F. El-Kady, Veronica Strong, Sergey Dubin, and Richard B. Kaner. Laser scribing of high-performance and flexible graphene-based electrochemical capacitors. *Science*, 335(6074):1326–1330, MAR 16 2012 2012.

[64] Dmitry V. Kosynkin, Amanda L. Higginbotham, Alexander Sinitskii, Jay R. Lomeda, Ayrat Dimiev, B. Katherine Price, and James M. Tour. Longitudinal unzipping of carbon nanotubes to form graphene nanoribbons. *Nature*, 458(7240):872–U5, APR 16 2009 2009.

[65] Liying Jiao, Li Zhang, Xinran Wang, Georgi Diankov, and Hongjie Dai. Narrow graphene nanoribbons from carbon nanotubes. *Nature*, 458(7240):877–880, APR 16 2009 2009.

[66] Ying Ying Wang, Zhen Hua Ni, Ting Yu, Ze Xiang Shen, Hao Min Wang, Yi Hong Wu, Wei Chen, and Andrew Thye Shen Wee. Raman studies of monolayer graphene: The substrate effect. *Journal of Physical Chemistry C*, 112(29), JUL 24 2008 2008.

[67] F. Schedin, A. K. Geim, S. V. Morozov, E. W. Hill, P. Blake, M. I. Katsnelson, and K. S. Novoselov. Detection of individual gas molecules adsorbed on graphene rid e-8556-2010. *Nature Materials*, 6(9):652–655, SEP 2007.

[68] Yaping Dan, Ye Lu, Nicholas J. Kybert, Zhengtang Luo, and A. T. Charlie Johnson. Intrinsic response of graphene vapor sensors rid a-8482-2011 rid c-4270-2008. *Nano Letters*, 9(4):1472–1475, APR 2009.

[69] Masa Ishigami, J. H. Chen, W. G. Cullen, M. S. Fuhrer, and E. D. Williams. Atomic structure of graphene on sio2 rid e-7634-2010. *Nano Letters*, 7(6):1643–1648, JUN 2007.

[70] P. Joshi, H. E. Romero, A. T. Neal, V. K. Toutam, and S. A. Tadigadapa. Intrinsic doping and gate hysteresis in graphene field effect devices fabricated on sio(2) substrates. *Journal of Physics-Condensed Matter*, 22(33):334214, AUG 25 2010.

[71] Zhi-Min Liao, Bing-Hong Han, Yang-Bo Zhou, and Da-Peng Yu. Hysteresis reversion in graphene field-effect transistors rid d-5315-2009. *Journal of Chemical Physics*, 133(4):044703, JUL 28 2010.

[72] Haomin Wang, Yihong Wu, Chunxiao Cong, Jingzhi Shang, and Ting Yu. Hysteresis of electronic transport in graphene transistors rid g-5965-2011. *Acs Nano*, 4(12):7221–7228, DEC 2010.

[73] Vincent E. Dorgan, Myung-Ho Bae, and Eric Pop. Mobility and saturation velocity in graphene on sio(2). *Applied Physics Letters*, 97(8):082112, AUG 23 2010 2010.

[74] R. R. Nair, P. Blake, A. N. Grigorenko, K. S. Novoselov, T. J. Booth, T. Stauber, N. M. R. Peres, and A. K. Geim. Fine structure constant defines visual transparency of graphene. *Science*, 320(5881):1308–1308, JUN 6 2008 2008.

[75] P. Blake, E. W. Hill, A. H. Castro Neto, K. S. Novoselov, D. Jiang, R. Yang, T. J. Booth, and A. K. Geim. Making graphene visible. *Applied Physics Letters*, 91(6):063124, AUG 6 2007 2007.

[76] Bjarke S. Jessen, Mikkel B. Klarskov, Lisa K. Tschammer, Tim J. Booth, and Peter Boggild. Automatic identification of single- and/or few-layer thin-film material, 2012.

[77] Isaac Childres, Luis A. Jauregui, Jifa Tian, and Yong P. Chen. Effect of oxygen plasma etching on graphene studied using raman spectroscopy and electronic transport measurements. *New Journal of Physics*, 13:025008, FEB 10 2011 2011.

[78] Dong Chul Kim, Dae-Young Jeon, Hyun-Jong Chung, YunSung Woo, Jai Kwang Shin, and Sunae Seo. The structural and electrical evolution of graphene by oxygen plasma-induced disorder. *Nanotechnology*, 20(37):375703, SEP 16 2009 2009.

[79] Huijiang Yu, Zhengguang Zou, Fei Long, Chunyan Xie, and Hao Ma. *Preparation of graphene with ultrasound- assisted in the process of oxidation*. 2010 2010. PT: B; CT: International Conference on Mechanical Engineering and Green Manufacturing (MEGM) 2010; CY: NOV 19-22, 2010; CL: Xiangtan, PEOPLES R CHINA; SP: Natl Nat Sci Fdn China; Shanghai Jiao Tong Univ; S China Univ Technol; Natl Univ Defense Technol; Central S Univ; Hunan Univ; Xiangtan Univ; Hunan Univ Sci & Technol; Hunan Inst Engn; TC: 0; UT: WOS:000290180601150.

[80] Yenny Hernandez, Valeria Nicolosi, Mustafa Lotya, Fiona M. Blighe, Zhenyu Sun, Sukanta De, I. T. McGovern, Brendan Holland, Michele Byrne, Yurii K. Gun'ko, John J. Boland, Peter Niraj, Georg Duesberg, Satheesh Krishnamurthy, Robbie Goodhue, John Hutchison, Vittorio Scardaci, Andrea C. Ferrari, and Jonathan N. Coleman. High-yield production of graphene by liquid-phase exfoliation of graphite. *Nature Nanotechnology*, 3(9), SEP 2008 2008.

[81] Shiren Wang, Yue Zhang, Noureddine Abidi, and Luis Cabrales. Wettability and surface free energy of graphene films. *Langmuir*, 25(18):11078–11081, SEP 15 2009 2009.

[82] P. M. Dunlap and S. R. Faris. Surface tension of aqueous solutions of potassium hydroxide. *Nature*, 196(4861):1312–&, 1962 1962.

[83] surface tension.de. Surface tension values of some common test liquids for surface energy analysis.

[84] Isaac Childres, Luis A. Jauregui, Michael Foxe, Jifa Tian, Romaneh Jalilian, Igor Jovanovic, and Yong P. Chen. Effect of electron-beam irradiation on graphene field effect devices. *Applied Physics Letters*, 97(17):173109, OCT 25 2010.

[85] Y. H. He, L. Wang, X. L. Chen, Z. F. Wu, W. Li, Y. Cai, and N. Wang. Modifying electronic transport properties of graphene by electron beam irradiation. *Applied Physics Letters*, 99(3):033109, JUL 18 2011 2011.

[86] A. Uhlir. The potentials of infinite systems of sources and numerical solutions of problems in semiconductor engineering. *Bell System Technical Journal*, 34(1):105–128, 1955 1955.

[87] Sune Thorsteinsson, Fei Wang, Dirch H. Petersen, Torben Mikael Hansen, Daniel Kjaer, Rong Lin, Jang-Yong Kim, Peter F. Nielsen, and Ole Hansen. Accurate microfour-point probe sheet resistance measurements on small samples rid b-9853-2009 rid a-8062-2010 rid c-4480-2011. *Review of Scientific Instruments*, 80(5):053902, MAY 2009.

[88] FM SMITS. Measurement of sheet resistivities with the 4-point probe. *Bell System Technical Journal*, 37(3):711–718, 1958.

[89] RYMASZEW.R. Relationship between correction factor of 4-point probe value and selection of potential and current electrodes. *Journal of Physics E-Scientific Instruments*, 2(2):170–&, 1969.

[90] Dirch H. Petersen. Micro four-point probe and micro hall effect - methods for reliable electrical characterization of ultra-shallow junctions, 2009.

[91] Dirch Hjorth Petersen, Rong Lin, Torben Mikael Hansen, Erik Rosseel, Wilfried Vandervorst, Christian Markvardsen, Daniel Kjaer, and Peter Folmer Nielsen. Comparative study of size dependent four-point probe sheet resistance measurement on laser annealed ultra-shallow junctions. *Journal of Vacuum Science & Technology B*, 26(1):362–367, JAN 2008 2008.

[92] Ozlem Sardan, Dirch H. Petersen, Kristian Molhave, Ole Sigmund, and Peter Boggild. Topology optimized electrothermal polysilicon microgrippers. *Microelectronic Engineering*, 85(5-6), MAY-JUN 2008 2008.

[93] Yugang Sun. Silver nanowires - unique templates for functional nanostructures. *Nanoscale*, 2(9), 2010 2010.

[94] Guanxiong Liu, Desalegne Teweldebrhan, and Alexander A. Balandin. Tuning of graphene properties via controlled exposure to electron beams. *Ieee Transactions on Nanotechnology*, 10(4), JUL 2011 2011.

[95] Jie Song, Menglin Chen, Mikkel Buster Olesen, Chenxuan Wang, Rasmus Havelund, Qiang Li, Erqing Xie, Rong Yang, Peter Boggild, Chen Wang, Flemming Besenbacher, and Mingdong Dong. Direct electrospinning of ag/polyvinylpyrrolidone nanocables. *Nanoscale*, 3(12), 2011 2011.

[96] D. Li and Y. N. Xia. Electrospinning of nanofibers: Reinventing the wheel? *Advanced Materials*, 16(14), JUL 19 2004 2004.

[97] Dirch H. Petersen, Ole Hansen, Torben M. Hansen, Peter R. E. Petersen, and Peter Boggild. Static contact micro four-point probes with $<$ 11 nm positioning repeatability. *Microelectronic Engineering*, 85(5-6), MAY-JUN 2008 2008.

[98] Myrsini Lafkioti, Benjamin Krauss, Timm Lohmann, Ute Zschieschang, Hagen Klauk, Klaus v Klitzing, and Jurgen H. Smet. Graphene on a hydrophobic substrate: Doping reduction and hysteresis suppression under ambient conditions. *Nano Letters*, 10(4):1149–1153, APR 2010.

[99] M. Mattmann, C. Roman, T. Helbling, D. Bechstein, L. Durrer, R. Pohle, M. Fleischer, and C. Hierold. Pulsed gate sweep strategies for hysteresis reduction in carbon nanotube transistors for low concentration no(2) gas detection. *Nanotechnology*, 21(18):185501, MAY 7 2010.

[100] Gopinadhan Kalon, Young Jun Shin, Viet Giang Truong, Alan Kalitsov, and Hyunsoo Yang. The role of charge traps in inducing hysteresis: Capacitance-voltage measurements on top gated bilayer graphene. *Applied Physics Letters*, 99(8):083109, AUG 22 2011 2011.

[101] Young Gon Lee, Chang Goo Kang, Uk Jin Jung, Jin Ju Kim, Hyeon Jun Hwang, Hyun-Jong Chung, Sunae Seo, Rino Choi, and Byoung Hun Lee. Fast transient charging at the graphene/sio2 interface causing hysteretic device characteristics. *Applied Physics Letters*, 98(18):183508, MAY 2 2011 2011.

[102] Jiyu Fan, J. M. Michalik, L. Casado, S. Roddaro, M. R. Ibarra, and J. M. De Teresa. Investigation of the influence on graphene by using electron-beam and photo-lithography. *Solid State Communications*, 151(21), NOV 2011 2011.

[103] D. Teweldebrhan and A. A. Balandin. Modification of graphene properties due to electron-beam irradiation rid c-1186-2009 rid f-9230-2011. *Applied Physics Letters*, 94(1):013101, JAN 5 2009.

[104] M. Z. Iqbal, Arun Kumar Singh, M. W. Iqbal, Sunae Seo, and Jonghwa Eom. Effect of e-beam irradiation on graphene layer grown by chemical vapor deposition. *Journal of Applied Physics*, 111(8):084307, APR 15 2012 2012.

[105] Ze Liu, Peter Boggild, Jia rui Yang, Yao Cheng, Francois Grey, Yi lun Liu, Li Wang, and Quan shui Zheng. A graphite nanoeraser. *Nanotechnology*, 22(26):265706, JUL 1 2011 2011.

[106] F. Giannazzo, S. Sonde, V. Raineri, and E. Rimini. Irradiation damage in graphene on sio2 probed by local mobility measurements. *Applied Physics Letters*, 95(26):263109, DEC 28 2009 2009.

[107] Andrea C. Ferrari. Raman spectroscopy of graphene and graphite: Disorder, electron-phonon coupling, doping and nonadiabatic effects. *Solid State Communications*, 143(1-2), JUL 2007 2007.

[108] A. C. Ferrari and J. Robertson. Origin of the 1150-cm(-1) raman mode in nanocrystalline diamond. *Physical Review B*, 63(12):121405, MAR 15 2001 2001.

[109] A. Zobelli, A. Gloter, C. P. Ewels, G. Seifert, and C. Colliex. Electron knock-on cross section of carbon and boron nitride nanotubes. *Physical Review B*, 75(24):245402, JUN 2007 2007.

[110] S. A. Imam, T. Deshpande, A. Guermoune, M. Siaj, and T. Szkopek. Charge transfer hysteresis in graphene dual-dielectric memory cell structures. *Applied Physics Letters*, 99(8):082109, AUG 22 2011 2011.

[111] O. Leenaerts, B. Partoens, and F. M. Peeters. Water on graphene: Hydrophobicity and dipole moment using density functional theory. *Physical Review B*, 79(23):235440, JUN 2009 2009.

[112] Wenjuan Zhu, Vasili Perebeinos, Marcus Freitag, and Phaedon Avouris. Carrier scattering, mobilities, and electrostatic potential in monolayer, bilayer, and trilayer graphene. *Physical Review B*, 80(23):235402, DEC 2009 2009.

[113] A. Betti, G. Fiori, and G. Iannaccone. Strong mobility degradation in ideal graphene nanoribbons due to phonon scattering. *Applied Physics Letters*, 98(21):212111, MAY 23 2011 2011.

[114] E. H. Hwang and S. Das Sarma. Acoustic phonon scattering limited carrier mobility in two-dimensional extrinsic graphene. *Physical Review B*, 77(11):115449, MAR 2008 2008.

[115] Jian-Hao Chen, W. G. Cullen, C. Jang, M. S. Fuhrer, and E. D. Williams. Defect scattering in graphene. *Physical Review Letters*, 102(23):236805, JUN 12 2009 2009.

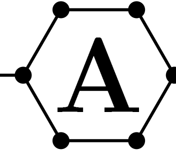

E-beam Fabrication Process

1.0	Grow oxide		
1.1	High doped wafers	<0.025 Ohm-cm	Dry oxide in phosper drive-in, use 2 dummy wafers at both ends of the boat. Recipe: dry1050C for 72mins. Complete times is usually around 4,5 hours
2.0	Fabricate index marks		
2.1	Surface preparation	HMDS coating	HMDS oven, recipe 4
2.2	Spin on resist	AZ5214e photoresist	SSE spinner, recipe: 2,2um 4inch
2.3	Pattern transfer	Mask: "Tibo index marks"	Karl Suss Aligner. Hard contact, 4.7sec
2.4	Image reversal	Hot plate, 110C, 100s for each wafer	Rest for 10 mins before flood exposure
2.5	Flood exposure	No mask	Karl Suss Aligner, 30 sec.
2.6	Develop	AZ5214e developer:H20 1:5	70 sec. develop, rinse in water 3 mins, spin dry
3.0	Clean wafers		
3.1	Remove graphite	Use tape under optical microscope	Remove graphite around graphene so there is space for metal contacts. Also remove large graphite pieces for more uniform resist

4.0	E-beam metal contacts		
4.1	Spin on resist	PMMA 950k 4% in Anisol	SSE Spinner, manual dispense, 1500 rpm, bake 180C for 3 mins, gives 300 nm
4.2	Al coating	150 Angstrom	Wordentec, thermal deposition, 2 Angstrom/s
4.3	E-beam exposure	To improve lift-off, smallest feature size should be 2 um, remember 4 corner boxes, and 180 degree rotation	E-beam writer, 1000 uC/cm2, 41 nA, aperture 7
4.4	Al removal	MF-CD-26	45 sec. clearly visible when removed, rinse in water for 1 min. Spin dry
4.5	Develop	1:3 MIBK:IPA	45 sec. Ensure movement during develop. Follow by rinse in water (45 sec), and rinse in IPA (45 sec). Blow dry.
4.6	Metal deposition	10 nm Ti and 100 nm Au	Alcatel (not Wordentec), 10 Angstrom/s
4.7	Lift-off	In Acetone	In petridish, soak for 15 mins, use cotton but to gently mechanically help the lift-off. Rinse in water (1 min), and IPA (1 min)
5.0	E-beam etch mask		
5.1	Spin on resist	PMMA 950k 4% in Anisol	SSE Spinner, manual dispense, 1500 rpm, bake 180C for 3 mins, gives 300 nm
5.2	Al coating	150 Angstrom	Wordentec, thermal deposition, 2 Angstrom/s
5.3	E-beam exposure	Draw large are around Hall bar, remember 4 corner boxes, and 180 degree rotation	E-beam writer: Large structures: 1000 uC/cm2, 6-8 nA Small structures: 1600 uC/cm2, 0.2 nA
5.4	Al removal	MF-CD-26	45 sec. clearly visible when removed, rinse in water for 1 min. Spin dry

5.5	Develop	1:3 MIBK:IPA	45 sec. Ensure movement during develop. Follow by rinse in water (45 sec), and rinse in IPA (45 sec). Blow dry.
5.6	Graphene etch	Depending on number of graphene layers to etch, use 3-5 sec etch. 3 sec for single layer, 5 sec for up to 3 layers	RIE 2, recipe mbk_graph: 45 sccm O2, 5 Ar, 40 mTorr, 10 W
5.7	Resist removal	In Acetone	In petridish, 5 mins. rinse in water (1 min), IPA (1 min), blow dry
6.0	Scribe wafers		
6.1	Scribe wafers	Cleanroom processing complete	

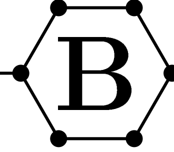

Graphene Identification

B.1 Graphene Identification

Automatic graphene identification consists of a series of image filters to successfully only single and/or few-layer graphene. Cleaved graphene on a SiO_2 wafer with index marks has some challenges, as illustrated in Fig. B.1. Graphene is identified as 10% contrast with the SiO_2 background. A background correction image is made, which is used reference. However, shadows from larger graphite flake, also has 10 % contrast in some part of the shadow. Furthermore, very small flakes of graphene ($<1\mu$m) are difficult to fabricate device from and are therefore not of highest interest. These factors leads to many false positive results, and therefore several image filters are combined to reduce them. Among the filters are expanding and contraction of areas of 10%, which will remove small areas.

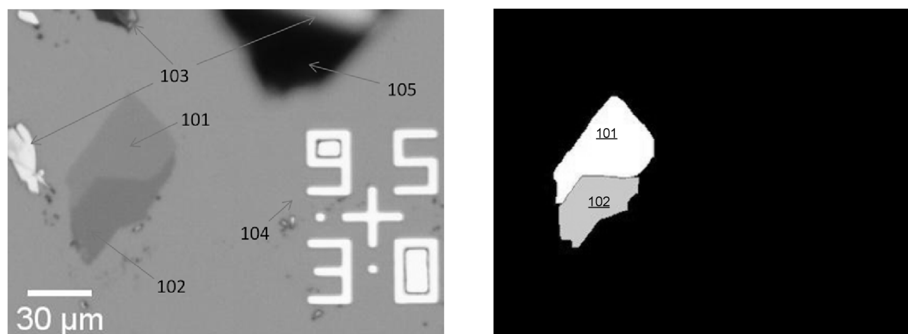

Figure B.1: **(Left)** Cleaved graphene on SiO_2. (101) Single layer graphene. (102) Bilayer graphene. (103) Graphite. (104) Au index mark. (105) Shadow. Image from [76]. **(Right)** Output of the script consists of a grayscale mask, indicating the areas of single, and few-layer graphene.

B.2 Image Recognition and Processing

The output image and mask from the graphene identification program (Fig. B.1) is further processed for making graphene devices. The process of identifying the position of the index marks in the image, rotate the image and the mask, perform image recognition to read out the numbers of the index marks, any number which was not identifiable is deduced from the other numbers, and finally write the data to a .cif-file.

The image recognition uses the fact that the numbers are written in a 7-segment display. For each number, each segment is tested by evaluating the intensity values of the pixel in the position of that segment, leading to an either true or false. When all segments are complete, the best estimate is considered being that number. It was found that the most difficult distinction was between the numbers zero and eight in the case of incomplete lift-off, as shown in Fig. 3.3

The programs has to be able to identify the crosses from two index marks in the image. Any other number found will be deduced from the position of those crosses. Another limitation is graphite flakes in contact with an number, will not successfully identify that number. Since these limitation only apply to a few images, the images can be modified using a standard image processing program in order to avert these issues.

B.3 Image Recognition Code

```
function [drawIM,drawG] = zImage2cif(folder,file,handles,hObject)
%IMAGE2CIF Summary of this function goes here
%   Function to analyse optical image of graphene on silicon
%   dioxide with index marks
%
%   Function includes:
%   - image recongnition of index marks
%   - image rotation of angled images
%   - graphene position identification
%   - drawing of index marks and graphene on different layers
%   - export to cif-file
%
%   Made by:
%   Mikkel Klarskov
%   Nanointegration
%   DTU Nanotech, Technical University of Denmark
%

indexmarkThreshold = 210;

filename = [folder file ".png"];
A = imread(filename);
A1 = A(:,:,1);

s = size(A);
imIndexMarks = zeros(s(1),s(2));

I = find(A1>indexmarkThreshold);
imIndexMarks(I) = 1;

txt = ["File: " file];
fprintf([txt "\n"]);
zUpdateLog(txt,1,handles,hObject);

%Find crosses in index marks
cross = zFindCrosses(imIndexMarks,handles,hObject);

filename = [folder file "fixed.png"];
%Graphene positions
imGraphene = imread(filename);
imGraphene = imGraphene(:,:,1);

%Rotate image
[imIndexMarks,imGraphene,angle] =
    zRotateImage(cross,imIndexMarks,imGraphene,handles,hObject);

%Image recognition of index marks
[drawIM,outLines] = zfindIndexMarks(imIndexMarks,handles,hObject);

drawG = bwboundaries(imGraphene);

A2 = imrotate(A1,angle);
```

```
zPlot(handles,flipud(A2),outLines,drawG);
guidata(hObject,handles);
fprintf("\n");

[drawIM,drawG] = zShift(drawIM,drawG);
zSaveCombinedCIF(struct,outFile);

end


function [cross] = zFindCrosses(image,handles,hObject)
%ZFINDCROSSES Summary of this function goes here
%   Detailed explanation goes here
minimumCrossWidth = 50;
maximumCrossWidth = 65;
ddx = (maximumCrossWidth+1)/2;
ints = [17 34 51];

boundaries = bwboundaries(image);

k = 1;
txt = "    Finding index marks locations... ";
fprintf(txt);
zUpdateLog(txt,1,handles,hObject);
for i=1:length(boundaries)
    c = boundaries{i};
    dx = max(c(:,2))-min(c(:,2));
    dy = max(c(:,1))-min(c(:,1));
    if(dx>minimumCrossWidth &&
       dx<maximumCrossWidth &&
       dy>minimumCrossWidth &&
       dy<maximumCrossWidth)
        s = "123456789";
        cx = round((max(c(:,2))+min(c(:,2)))/2);
        cy = round((max(c(:,1))+min(c(:,1)))/2);
        C = image(cy-ddx:cy+ddx,cx-ddx:cx+ddx);
        s(1) = num2str(C(ints(1),ints(1)));
        s(2) = num2str(C(ints(1),ints(2)));
        s(3) = num2str(C(ints(1),ints(3)));
        s(4) = num2str(C(ints(2),ints(1)));
        s(5) = num2str(C(ints(2),ints(2)));
        s(6) = num2str(C(ints(2),ints(3)));
        s(7) = num2str(C(ints(3),ints(1)));
        s(8) = num2str(C(ints(3),ints(2)));
        s(9) = num2str(C(ints(3),ints(3)));
        t = bin2dec(s);
        if(t==186)
            cross{k}.boundary = c;
            cross{k}.centerX = cx;
            cross{k}.centerY = cy;
            k = k+1;
        end
    end
end
txt = ["found " num2str(length(cross)) " index marks"];
fprintf([txt "\n"]);
zUpdateLog(strcat(txt,char(10)),0,handles,hObject);
```

```
end


function zSaveCombinedCIF(struct,outputFile)
%ZSAVECOMBINEDCIF Summary of this function goes here
%   Detailed explanation goes here
cifScaling = 2000;
cif = "(CIF export from MatLab);\n";
cif = [cif "(Automated generated file);\n"];
cif = [cif "(Scaling: 1 CIF Unit = 1/2000 Microns);\n"];
cif = [cif "(Written by Mikkel Klarskov, Nanointegration,...
       DTU Nanotech);\n"];

for j=1:length(struct)
    drawIM = struct{j}.drawIM;
    drawG = struct{j}.drawG;
    cif = [cif "DS " num2str(j) " 2 40;\n"];
    cif = [cif "9 " num2str(struct{j}.name) ";\n"];
    cif = [cif "L ImportedIndexMarks;\n"];

    for i=1:length(drawIM)
        c = drawIM{i}.boundary;
        cif = [cif "P "];
        for j=1:size(c)
            cif = [cif num2str(round(c(j,2)*cifScaling))...
                  "," num2str(round(c(j,1)*cifScaling)) " "];
        end
        cif = [cif ";\n"];
        for k=1:4
            %drawIM{i}.number{k}
            if(~isempty(drawIM{i}.number{k}))
                c = drawIM{i}.number{k}.boundary;
                cif = [cif "P "];
                for j=1:length(c)
                    cif = [cif num2str(round(c(j,2)*cifScaling))...
                           "," num2str(round(c(j,1)*cifScaling)) " "];
                end
                cif = [cif ";\n"];
            end
        end
    end

    cif = [cif "L Graphene;\n"];
    for i=1:length(drawG)
        c = drawG{i};
        %if(length(c)>20)
            cif = [cif "P "];
            for j=1:length(c)
                cif = [cif num2str(round(c(j,2)*cifScaling))...
                       "," num2str(round(c(j,1)*cifScaling)) " "];
            end
            cif = [cif ";\n"];
        %end
    end

    cif = [cif "DF;\n"];
```

```
end

cif = [cif "DS " num2str(length(struct)+1) " 2 40;\n"];
cif = [cif "9 importedGrapheneSamples;\n"];
for j=1:length(struct)
    cif = [cif "C " num2str(j) " T 0 0;\n"];
    cif = [cif "91 U" num2str(struct{j}.name) ";\n"];
end
cif = [cif "DF;\n"];
cif = [cif "E"];

fid = fopen(outputFile,"w");
fprintf(fid,cif);
fclose(fid);

end
```

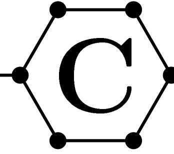

Articles

C.1 Fast and direct measurements of the electrical properties of graphene using micro four-point probes

IOP PUBLISHING NANOTECHNOLOGY
Nanotechnology **22** (2011) 445702 (6pp) doi:10.1088/0957-4484/22/44/445702

Fast and direct measurements of the electrical properties of graphene using micro four-point probes

M B Klarskov[1], H F Dam[1], D H Petersen[1], T M Hansen[1], A Löwenborg[1], T J Booth[1], M S Schmidt[1], R Lin[2], P F Nielsen[2] and P Bøggild[1]

[1] Department of Micro- and Nanotechnology, Technical University of Denmark, DTU Nanotech, Building 345E, DK-2800 Kongens Lyngby, Denmark
[2] CAPRES A/S, Scion-DTU, Building 373, DK-2800 Kongens Lyngby, Denmark

E-mail: mikkel.olesen@nanotech.dtu.dk

Received 8 July 2011, in final form 14 September 2011
Published 6 October 2011
Online at stacks.iop.org/Nano/22/445702

Abstract
We present measurements of the electronic properties of graphene using a repositionable micro four-point probe system, which we show here to have unique advantages over measurements made on lithographically defined devices; namely speed, simplicity and lack of a need to pattern graphene. Measurements are performed in ambient, vacuum and controlled environmental conditions using an environmental scanning electron microscope (SEM). The results are comparable to previous results for microcleaved graphene on silicon dioxide (SiO_2). We observe a pronounced hysteresis of the charge neutrality point, dependent on the sweep rate of the gate voltage; and environmental measurements provide insight into the sensor application prospects of graphene. The method offers a fast, local and non-destructive technique for electronic measurements on graphene, which can be positioned freely on a graphene flake.

(Some figures in this article are in colour only in the electronic version)

1. Introduction

Since the first demonstration of isolated graphene and its field effect properties [1], much effort has been focused on its electrical properties [2], since the carriers in graphene behave as massless fermions with a linear dispersion relation around the Dirac points [3].

The typical approach toward testing the electrical properties of graphene is by patterning the graphene into a suitable geometry and depositing electrodes by photo- or electron beam (e-beam) lithography [1, 4, 5]. In the case of microcleaved graphene, the lithography pattern must be aligned to the individual graphene flake, followed by at least one round of exposure, development, metallization and lift-off. Large-area graphene from chemical vapor deposition (CVD) and epitaxial growth on silicon carbide is less restrictive in terms of alignment, but still requires definition of a field effect transistor-like electrode geometry [6].

With the drastic increase in available graphene area [7, 8], the verification of the electronic properties of as-produced graphene becomes increasingly important, and will constitute a quickly narrowing bottleneck for industrial development and research. Furthermore, the lithographic patterning of graphene leads to irreversible changes to the sample, and previous results show that the lithography process itself may change the electronic properties, leaving resist residues, contaminants etc [9, 10].

An obvious solution is to use repositionable electrodes. Several scanning probe techniques have been applied to the characterization of graphene, such as scanning probe gate measurement of the charge neutrality point [11], and electrostatic force microscopy [12]. Conducting atomic force microscopy (AFM) is also possible [13]; however, here it was demonstrated that the bias voltage can lead to undesirable patterning of the graphene through local anodic oxidation [13]. Although these methods probe the

0957-4484/11/445702+06$33.00 1 © 2011 IOP Publishing Ltd Printed in the UK & the USA

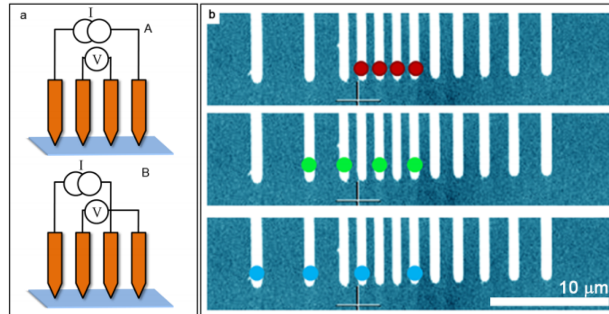

Figure 1. (a) Illustration of M4PP with two different measurement configurations, A and B, where V measures the voltage drop, and I indicates a current source. (b) Optical image of the 12-point probe used in ambient measurements. Three different pitches are indicated, 1.5 μm, 3.0 μm and 4.5 μm, respectively.

electrical properties, lithographic definition of at least one electrode on the graphene sample is still required. Recently, four independently positioned electrodes were applied for rotational square configuration measurements of multi-layer epitaxial graphene on SiC in a 100 × 100 μm^2 measurement area [14]. Although this technique allows for anisotropic conductance characterization [15], microfabricated four-point probes (M4PP) [16] are much simpler to operate, and do not involve individual alignment of the scanning probe tips. This makes mapping a practical possibility, which has been demonstrated for numerous other materials including conjugated monolayer polymers [17] and non-uniform ultra-thin semiconductors with lateral dimensions down to 10 × 10 μm^2 [18]. In addition, it has recently been shown that the Hall carrier mobility and carrier density can be extracted from collinear four-point probe measurements [19]. Multiple previous measurements of the conductance of graphene using lithographically defined fixed electrodes have been made, falling in the range 0.1–8 mS [20–22], and the conductivity of graphene particles has been measured at 64 mS cm^{-1} using standard four-point probe techniques [23].

In this work we show that repositionable, monolithic micro four-point probes provide a fast, local and non-destructive technique for measuring the electrical properties of graphene, despite the extreme thinness of the material and the mechanical contact required. We show that the method can be used in both ambient and vacuum conditions, and employ environmental scanning electron microscopy (ESEM) to investigate the effect of the local environment.

2. Methods

The current investigation involves equidistant M4PP measurements on micromechanically cleaved graphene samples. Two electrodes are used for sourcing a current, I, and the other two for measuring the corresponding voltage drop, V. Two different measurement modes were used; single and dual configuration. In the single configuration mode we calculate the sheet conductance $\sigma = I/(cV)$, where c is the geometrical correction factor [24]. Due to position errors of the electrodes there is a unique static error on the geometrical correction factor. Using dual configuration, this static position error is eliminated [25], as well as geometrical errors caused by finite sample size [27]. Figure 1(a) illustrates the two current/voltage electrode configurations used for dual configuration position correction, A and B.

Graphene samples were produced by mechanical exfoliation of graphite on low-resistivity wafers with thermally grown 90 nm silicon dioxide (SiO_2) film. Prior to the exfoliation, the wafers were baked at 120°C and cleaned in O_2/N_2 plasma for 5 min. Gate voltage was controlled by a back-side contact; however, to improve M4PP to surface alignment, top-side connections were preferred. To avoid chemical interaction with the graphene, the top electrode was made by removing an area of the SiO_2 by reactive ion etching and metal deposition using a shadow mask.

3. Ambient conditions

The measurements in ambient conditions (i.e. in air at room temperature and pressure) were obtained using a commercial Capres MicroRSP-M150 system with Capres M12PP probes (see figure 1(b)), from which the equidistant pitch configurations 1.5, 3 and 4.5 μm were selected for the measurements. An AC current of 1 μA was used. The time for making a measurement was 5 min, with a gate voltage sweep from 0 V to +60 V and back to 0 V.

Figure 2 displays a typical dual configuration measurement of the conductance as a function of applied gate voltage in ambient conditions. Three different pitches were used, indicated by the three different curves, and two different measurement configurations were combined [25, 26] to give the result shown. Defining hysteresis as the difference in the conductance minima, we observe a pronounced hysteresis of approximately 35 V. Such hysteresis effects are commonplace

Nanotechnology **22** (2011) 445702 M B Klarskov *et al*

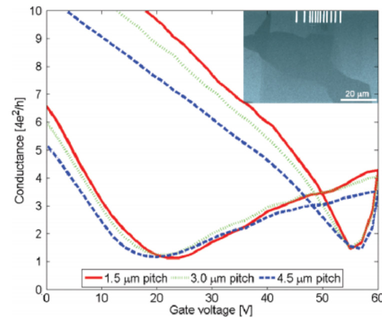

Figure 2. The conductance of a graphene flake in ambient conditions on clean SiO_2 as function of applied gate voltage. The conductance is measured with 10 configurations per gate step and gate voltage steps of 2 V. In each data point, recordings with three different voltage probe pitches, 1.5 μm (red solid), 3.0 μm (green dotted) and 4.5 μm (blue dashed), were done. The insert shows an optical image of a 12-point probe over a single layer of graphene.

for graphene on SiO_2 [4, 5, 27–29]. The effect was explained by Wang *et al* [30] as trapped charges in the SiO_2 leading to a different effective gate voltage experienced by the graphene, as compared to the applied gate voltage. The hysteresis effect is further discussed after vacuum measurements. The carrier mobility was calculated from $\mu = t/\varepsilon \times \mathrm{d}\sigma/\mathrm{d}V_g$ [1], where t is the thickness and ε is the permittivity of SiO_2 and V_g is the gate voltage. The mobilities are calculated to be in the range 1000–2500 $\mathrm{cm^2\ V^{-1}\ s^{-1}}$.

4. Vacuum conditions

For measurements in a vacuum (10^{-5} Pa), a FEI Quanta 200 ESEM FEG was used. The probes were mounted on a 13-axis SmarAct micromanipulator which was fitted in the ESEM, and all measurements were performed with 1.5 μm pitch probes. After carefully aligning the probe to the plane of the sample, they were brought within 1–2 mm of the surface before evacuating the chamber. Measurement on gold coated regions was used to verify proper operation of the individual electrodes. A DC current of 10 μA was sourced using a Keithley 2400 sourcemeter, while the voltage drop was measured with a National Instrument data acquisition (DAQ) card. The gate voltage was applied by the DAQ card, and amplified using a Falco Systems voltage amplifier. The gate voltage was swept from 0 to +60 to −60 V and back to 0 V in all measurements, at a controllable rate of between 0.4 and 240 $\mathrm{V\ s^{-1}}$, corresponding to a full sweep frequency between 1.7 mHz and 1 Hz.

Alignment of the M4PP was made with reference to lithographically defined index marks, and the probes were engaged with the graphene sample outside of the field of view of the microscope until electrical contact was measured. This was done in order to avoid exposing the graphene sample to the e-beam irradiation, which has been shown to introduce damage [31–34] as well as contamination on the surface. In order to do fast gate sweeps, we used a single configuration (A) for vacuum measurements. Conductance measurements for three different sweep rates are shown in figures 3(a)–(c), with only the positive gate voltages. For high sweep rates, there is a low signal-to-noise ratio, so multiple sweeps were averaged to produce the data shown.

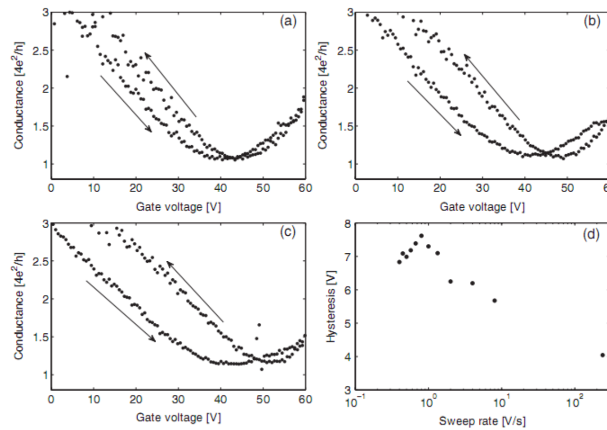

Figure 3. Measurements in a vacuum showing conductance (in $4e^2/h$) as a function of applied gate voltage for different sweep rates: (a) 240 $\mathrm{V\ s^{-1}}$, (b) 4 $\mathrm{V\ s^{-1}}$, (c) 0.4 $\mathrm{V\ s^{-1}}$. Arrows indicate the sweep direction. The hysteresis appears to increase as the sweep rate is decreased. (d) Hysteresis as function of sweep rate, which shows a maximum in hysteresis at 0.8 $\mathrm{V\ s^{-1}}$. Hysteresis was found by a parabolic fit to the data below a conductance of 1.5 times $4e^2/h$. Error on the fit is negligible.

Nanotechnology **22** (2011) 445702 M B Klarskov *et al*

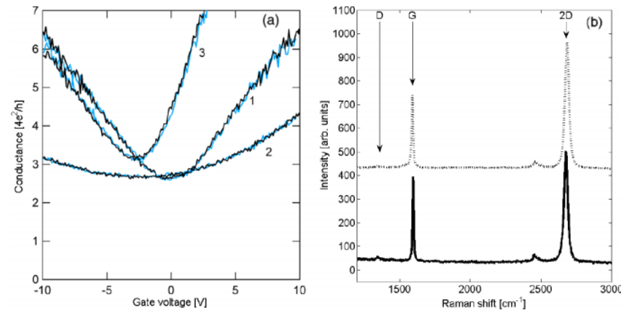

Figure 4. (a) Environmental measurement where the mobility decreases when graphene was exposed to water vapor. Graphene starts in high vacuum (1), water vapor is introduced (low vacuum) (2) and finally high vacuum is achieved again (3). Colors represent up- (black) and down-sweep (blue). (b) Raman spectrum before (solid) and after (dotted) measurements in SEM. The spectrum is shifted for clarity. The ratio of the intensity of the D peak to the G peak remains small after the measurement, indicating that the graphene did not alter in structure using the method described in the text.

The charge neutrality points are calculated by fitting a parabola near the minimum conductance of the up- and down-sweep, and finding the minimum of the fit. The carrier mobility is estimated in the same manner as the measurements in ambient conditions. As the sweep rate is decreased, the hysteresis changes, and the mobilities are observed to decrease slightly from ∼1200 to ∼1000 cm^2 V^{-1} s^{-1}.

The variation of hysteresis with sweep time is shown in figure 3(d). It is observed that the hysteresis increases up to 0.8 V s^{-1}, followed by a decrease. This trend was observed on all samples investigated.

In the following work we use an environmental SEM in which a range of gases can be leaked into the sample chamber in order to study the influence of the local gas environment on conductance and mobility. Figure 4(a) shows the effect of water vapor on conductance. First, a high vacuum (10^{-5} Pa) measurement was performed (1), resulting in mobility around 2000 cm^2 V^{-1} s^{-1}. Water vapor was introduced at 400 Pa (2), and the mobility dropped to roughly 500 cm^2 V^{-1} s^{-1}. Evacuating the chamber to 10^{-5} Pa again (3) the mobility was restored to its initial value, with a slight shift in the charge neutrality point and minimum conductivity.

Figure 4(b) shows Raman spectra from pristine graphene samples and graphene samples contacted outside the field of view. The $I(\mathrm{D})/I(\mathrm{G})$ ratio remains small after ESEM measurements, which shows no indication of an increased density of defects [35].

Our results obtained under vacuum in a SEM show that the hysteresis in the charge neutrality point depends on the sweep rate, with a maximum hysteresis at 0.8 V s^{-1}. The hysteresis effect has been observed in many graphene field effect devices, and has been suggested to be caused by charge trapping in the SiO_2 [4, 30].

When changing the gate voltage, the electric field traps or detraps charges at a specific rate. Therefore, it may be expected that the hysteresis will approach zero for high sweep rates since the traps do not have time to fill. This should lead to a time-dependence of the hysteretic effect, and thus a varying offset of the charge neutrality point. Furthermore, it is expected that a steady state will be achieved for very low sweep rates, so hysteresis should also approach a constant value, possibly zero. Mattmann *et al* [36] demonstrated that pulsing the gate voltage is a highly efficient method to strongly reduce gate hysteresis for carbon nanotube based field effect sensors.

Environmental measurements showed a clear reduction in carrier mobility, when comparing high vacuum to low vacuum with water vapor. These results contradict previous measurements with a variety of adsorbed gases on graphene which showed no change in mobility [37]. We are unable to specifically determine the cause of this contradiction, but suggest that our observations of changing mobility may be due to ionization of water molecules which adsorb onto the graphene surface, and thereby increase the number of charged surface scatterers. Protons and hydroxyl groups may also be able to neutralize some of the charged species already on the surface, which then may desorb from the surface when a high vacuum is reintroduced. This would explain why the mobility is slightly increased when comparing the two high vacuum states.

While we frequently encountered a poor electrical contact to the graphene, damage to the graphene surface was rarely observed. The graphene seemed very resistant to mechanical scratching; however, breakdown occurred consistently at a current of around 100 μA or more. This can be explained by a high current density at the contact points, which from previous studies [38] can be expected to be at minimum 100 nm in diameter. Assuming the thickness of the graphene layer to be 3.4 Å, the current density at the perimeter of a contact area is in rough agreement with the critical current density of graphene of 10^8 A cm^{-2} found experimentally by Murali *et al* [39], at 10^7 A cm^{-2}.

5. Conclusion

We have shown that micro four-point probes can be used to perform local and non-destructive measurements on graphene, within a shorter time span than with commonly used lithographic processing. The sample size is only limited by the electrode pitch, and the non-destructive approach makes further processing of the sample possible. To compete with lithographic contacts, it is of key importance that the approach can be used in a vacuum or controlled atmospheric conditions, which we have demonstrated here. We observed a strong tendency of the carrier mobility to decrease in the presence of water vapor, which conflicts with previous reports. It is anticipated that micro four-point probes could be an invaluable tool for inline verification and process monitoring in graphene fabrication, as well as providing a unique possibility of probing and mapping the local transport properties of graphene.

Acknowledgments

We appreciate financial support by the Danish Research Council for Technology and Production Sciences (Nanoengineered Graphene Devices) as well as helpful discussions with Cosmin Roman and Christofer Hierold, both ETH Zurich, Micro and Nanosystems.

References

[1] Novoselov K S, Geim A K, Morozov S V, Jiang D, Zhang Y, Dubonos S V, Grigorieva I V and Firsov A A 2004 Electric field effect in atomically thin carbon films *Science* **306** 666–9
[2] Avouris P, Chen Z and Perebeinos V 2007 Carbon-based electronics *Nature Nanotechnol.* **2** 605–15
[3] Novoselov K S, Geim A K, Morozov S V, Jiang D, Katsnelson M I, Grigorieva I V, Dubonos S V and Firsov A A 2005 Two-dimensional gas of massless Dirac fermions in graphene *Nature* **438** 197–200
[4] Lafkioti M, Krauss B, Lohmann T, Zschieschang U, Klauk H, Klitzing K and Smet J H 2010 Graphene on a hydrophobic substrate: doping reduction and hysteresis suppression under ambient conditions *Nano Lett.* **10** 1149–53
[5] Lohmann T, Klitzing K and Smet J H 2009 Four-terminal magneto-transport in graphene p–n junctions created by spatially selective doping *Nano Lett.* **9** 1973–9
[6] Cao H *et al* 2010 Electronic transport in chemical vapor deposited graphene synthesized on Cu: quantum Hall effect and weak localization *Appl. Phys. Lett.* **96** 122106
[7] Bae S *et al* 2010 Roll-to-roll production of 30-inch graphene films for transparent electrodes *Nature Nanotechnol.* **5** 574–8
[8] Li X *et al* 2009 Large-area synthesis of high-quality and uniform graphene films on copper foils *Science* **324** 1312–4
[9] Ishigami M, Chen J H, Cullen W G, Fuhrer M S and Williams E D 2007 Atomic structure of graphene on SiO_2 *Nano Lett.* **7** 1643–8
[10] Jacobsen A, Koehler F M, Stark W J and Ensslin K 2010 Towards electron transport measurements in chemically modified graphene: effect of a solvent *New J. Phys.* **12** 125007
[11] Yu Y, Zhao Y, Ryu S, Brus L E, Kim K S and Kim P 2009 Tuning the graphene work function by electric field effect *Nano Lett.* **9** 3430–4
[12] Filleter T, Emtsev K V, Seyller Th and Bennewitz R 2008 Local work function measurements of epitaxial graphene *Appl. Phys. Lett.* **93** 133117
[13] Kellar J A, Alaboson J M P, Wang Q H and Hersam M C 2010 Identifying and characterizing epitaxial graphene domains on partially graphitized SiC(0001) surfaces using scanning probe microscopy *Appl. Phys. Lett.* **96** 143103
[14] Yakes M K, Gunlycke D, Tedesco J L, Campbell P M, Myers-Ward R L, Eddy C R, Gaskill D K, Sheehan P E and Laracuente A R 2010 Conductance anisotropy in epitaxial graphene sheets generated by substrate interactions *Nano Lett.* **10** 1559–62
[15] Kanagawa T, Hobara R, Matsuda I, Tanikawa T, Natori A and Hasegawa S 2003 Anisotropy in conductance of a quasi-one-dimensional metallic surface state measured by a square micro four-point probe method *Phys. Rev. Lett.* **91** 036805
[16] Petersen C L, Grey F, Shiraki I and Hasegawa S 2000 Microfour-point probe for studying electronic transport through surface states *Appl. Phys. Lett.* **77** 3782
[17] Bøggild P, Grey F, Hassenkam T, Greve D R and Bjømholm T 2000 Direct measurement of the microscale conductivity of conjugated polymer monolayers *Adv. Mater.* **12** 947–50
[18] Rosseel E *et al* 2009 Monitoring of local and global temperature non-uniformities by means of therma-probe and micro four-point probe metrology *17th Int. Conf. on Advanced Thermal Processing of Semiconductors* pp 1–6
[19] Petersen D H, Hansen O, Lin R and Nielsen P F 2008 Micro-four-point probe Hall effect measurement method *J. Appl. Phys.* **104** 013710
[20] Bolotin K I, Sikes K J, Jiang Z, Klima M, Fudenberg G, Hone J, Kim P and Stormer H L 2008 Ultrahigh electron mobility in suspended graphene *Solid State Commun.* **146** 351–5
[21] Huard B, Stander J, Sulpizio J A and Goldhaber-Gordon D 2008 Evidence of the role of contacts on the observed electron–hole asymmetry in graphene *Phys. Rev.* B **78** 121405(R)
[22] Venugopal A, Colombo L and Vogel E M 2010 Contact resistance in few and multilayer graphene devices *Appl. Phys. Lett.* **96** 013512
[23] Alwarappan S, Erdem A, Liu C and Li C 2009 Probing the electrochemical properties of graphene nanosheets for biosensing applications *J. Phys. Chem.* C **20** 8853–6
[24] Smits F M 1958 Measurement of sheet resistivities with the four-point probe *Bell Syst. Techn. J.* **37** 711–8
[25] Rymaszewski R 1969 Relationship between the correction factor of the four-point probe value and the selection of potential and current electrode *J. Phys. E: Sci. Instrum.* **2** 170
[26] Thorsteinsson S, Wang F, Petersen D H, Hansen T M, Kjaer D, Lin R, Kim J Y, Nielsen P F and Hansen O 2009 Accurate microfour-point probe sheet resistance measurements on small samples *Rev. Sci. Instrum.* **80** 053902
[27] Dan Y, Lu Y, Kybert N J, Luo Z and Johnson A T C 2009 Intrinsic response of graphene vapor sensors *Nano Lett.* **9** 1472–5
[28] Joshi P, Romero H E, Neal A T, Toutam V K and Tadigadapa S A 2010 Intrinsic doping and gate hysteresis in graphene field effect devices fabricated on SiO_2 substrates *J. Phys.: Condens. Matter* **22** 334214
[29] Liao Z, Han B, Zhou Y and Yu D 2010 Hysteresis reversion in graphene field-effect transistors *J. Chem. Phys.* **133** 044703
[30] Wang H, Wu Y, Cong C, Shang J and Yu T 2010 Hysteresis of electronic transport in graphene transistors *ACS Nano* **4** 7221–8

[31] Teweldebrhan D and Balandin A A 2009 Modification of graphene properties due to electron-beam irradiation *Appl. Phys. Lett.* **94** 013101

[32] Rao G, Mctaggart S, Lee J L and Geer R E 2009 Study of electron beam irradiation induced defectivity in mono and bi layer graphene and the influence on raman band position and line-width *Mater. Res. Soc. Symp. Proc.* **1184** 151–6

[33] Childres I, Jauregui L A, Foxe M, Tian J, Jalilian R, Jovanovic I and Chen Y P 2010 Effect of electron-beam irradiation on graphene field effect devices *Appl. Phys. Lett.* **97** 173109

[34] Xu M, Fujita D and Hanagata N 2010 Monitoring electron-beam irradiation effects on graphene by temporal Auger electron spectroscopy *Nanotechnology* **21** 265705

[35] Tang B, Hu G and Hanyang G 2010 Raman spectroscopic characterization of graphene *Appl. Spectrosc. Rev.* **45** 369–407

[36] Mattmann M, Roman C, Helbling T, Bechstein D, Durrer L, Pohle R, Fleischer M and Hierold C 2010 Pulsed gate sweep strategies for hysteresis reduction in carbon nanotube transistors for low concentration NO_2 gas detection *Nanotechnology* **21** 185501

[37] Schedin F, Geim A K, Morozov S V, Hill E W, Blake P, Katsnelson M I and Novoselov K S 2007 Detection of individual gas molecules adsorbed on graphene *Nature Mater.* **6** 652–5

[38] Ansbaek T, Petersen D H, Hansen O, Larsen J B, Hansen T M and Bøggild P 2009 Fundamental size limitations of micro four-point probes *Microelectron. Eng.* **86** 987–90

[39] Murali R, Yang Y, Brenner K, Beck T and Meindl J D 2009 Breakdown current density of graphene nanoribbons *Appl. Phys. Lett.* **94** 243114

C.2 Micro-cantilever for non-destructive characterization of nanograss uniformity

MICRO-CANTILEVERS FOR NON-DESTRUCTIVE CHARACTERIZATION OF NANOGRASS UNIFORMITY

Dirch H. Petersen[1], Fei Wang[1], Mikkel B. Olesen[1], Rafal Wierzbicki[1], Michael S. Schmidt[1], Peter F. Nielsen[2], Peter Bøggild[1], Ole Hansen[1, 3], and Kristian Mølhave[1].

[1]DTU Nanotech, Technical University of Denmark, Building 345E, DK-2800 Kgs. Lyngby, Denmark

[2]CAPRES A/S, Scion-DTU, Building 373, DK-2800 Kgs. Lyngby, Denmark

[3]CINF - Center for Individual Nanoparticle Functionality, NanoDTU, Denmark

KEYWORDS

Nanograss; Surface morphology; Four-point probe; Tribology; Static contact; Non-destructive contact.

ABSTRACT

We demonstrate an application of three-way flexible micro four-point probes for indirect uniformity characterization of surface morphology. The mean sheet conductance of a quasi-planar 3D nanostructured surface is highly dependent on the surface morphology, and thus accurate sheet conductance measurements may be useful for process uniformity characterization. The method is applied for characterization of TiW coated nanograss uniformity. Three-way flexible L-shaped cantilever electrodes are used to avoid damage to the fragile surface, and a relative standard deviation on measurement repeatability of 0.12 % is obtained with a measurement yield of 97%. Finally, variations in measured sheet conductance are correlated to the surface morphology as characterized by electron microscopy.

INTRODUCTION

Densely nanostructured surfaces and nanowire arrays are relevant for a number of applications, including photovoltaics [1], superhydrophobic surfaces [2] and surface enhanced Raman spectroscopy [3, 4]. A range of tools such as Atomic Force Microscopy (AFM), Scanning Electron Microscopy (SEM) and ellipsometry [5] are available for characterization of homogeneity of surface morphology as well as other physical properties. There is no established method for measuring the homogeneity of the electrical properties of fragile nanostructured surfaces.

Micro four-point probes (M4PP) with straight cantilevers [6] have in recent years proved to be a very useful tool for accurate sheet resistance and carrier mobility characterization of ultra thin films [7]. Compared to conventional four-point probes, the M4PP greatly reduces the destructive nature of the probe contact [8]. However, electrical characterization of fragile surfaces such as organic thin films and high-aspect ratio nanostructured surfaces require an even gentler probe contact in order to avoid structural damage induced by lateral contact forces during mechanical contact. Three-way flexible L-shaped cantilever electrodes have been developed to achieve static contact on planar surfaces which drastically reduces frictional tip wear [9]. This type of probe is here applied to provide non-destructive contact to fragile conductive nanostructured surfaces.

In this paper, we propose a four-point probe method for indirect uniformity characterization of nanostructured surfaces. We investigate the measurement repeatability as well as the sensitivity to surface morphology variations by characterization of fragile TiW coated nanograss. Using three-way flexible electrodes we demonstrate how the mechanical contact may be non-destructive, resulting in an increased measurement yield compared to conventional straight cantilever electrodes.

CONDUCTANCE AND MORPHOLOGY

The exact analysis of four-point measurements of non-planar structures is not trivial. However, we may define a mean sheet conductance G_S for a quasi-planar 3D structured conductive film with a mean thickness d much smaller than the electrode pitch s, $d \ll s$. The mean sheet conductance is dependent on the thin film conductivity and morphology. The conductivity of thin films with a thickness comparable to the carrier mean free path is strongly dependent on the film thickness [10, 11]. However, the film thickness and specific surface morphology are both simple geometrical effects, and it follows that four-point measurements may be used as an indirect method to monitor variations in surface morphology, e.g. nanowire density, length and diameter.

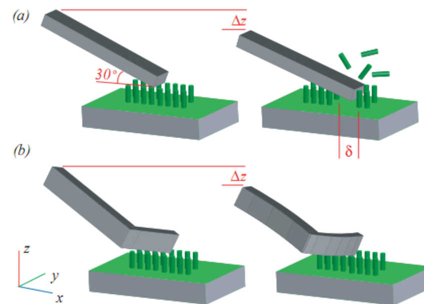

Figure 1: Schematic view of the conventional straight cantilever (a) and the L-shaped cantilever (b) engaged a distance Δz on fragile TiW nanograss. The straight cantilever is virtually incompressible and thus slides with a distance δ while damaging the nanograss. In comparison, the L-shaped cantilever exerts far smaller lateral force and thus allow to the probe tips to maintain a non-destructive static contact.

978-1-4577-0156-6/11/$26.00 ©2011 IEEE 1060 Transducers'11, Beijing, China, June 5-9, 2011

THREE-WAY FLEXIBLE ELECTRODES

To obtain a high measurement yield on fragile thin films and to avoid excessive sample damage, contact forces must be minimal. Straight cantilever electrodes are virtually incompressible in the cantilever length direction, hence for the straight cantilevers used in this work, the spring constant is more than two orders of magnitude larger in the length direction than in orthogonal directions. Thus, straight cantilevers will exert a large lateral force on the fragile nanostructured surface during engagement. In contrast, L-shaped cantilevers are designed to be equally flexible in all directions, and so the reaction force is almost perfectly normal to the sample surface and the lateral force insignificant $F_{lat} \approx 0$. Figure 1 shows a schematic comparison of the two cantilever designs resulting in destructive and non-destructive mechanical contacts to a nanograss surface for the straight and L-shaped cantilevers, respectively.

EXPERIMENTAL

The samples used in this investigation are TiW coated silicon nanograss. High aspect ratio nanograss was prepared by deep reactive ion etching (DRIE) of 100 mm boron-doped silicon wafers (1-20 Ωcm) using the black silicon method [4] and subsequent sputter deposition of semi-conformal TiW with a nominal thickness on planar surfaces of 300 nm. The DRIE process was performed in an STS ICP Advanced Silicon Etcher and TiW coating was done in a Wordentec deposition system.

Micro four-point probes where fabricated in 5 µm thick polysilicon using a process described by Özlem et al. [12] and the cantilever electrodes were coated with 10/200 nm Ti/Ni. Both straight and L-shaped cantilevers have a nominal spring constant of approximately 10 N/m normal to the sample surface.

Experiments to evaluate mechanical contacts were performed in-situ in an FEI Nova 600 NanoSEM with a M4PP SEM Module. Four-point repeatability and uniformity measurements were performed on a CAPRES microRSP-M150 using lock-in technique with a frequency of 11 Hz and a current set-point of 200 µA. Measurements were done with 20 µm electrode pitch and the mean sheet conductance was calculated using the dual configuration method [13, 14].

RESULTS AND DISCUSSION

Non-destructive contacts

To study contact scrub marks on nanograss, in-situ M4PP measurements with simultaneous recording of SEM images were performed with both cantilever types. For an engagement depth Δz of 1-2 µm, large scrub marks resulted from the straight cantilevers, cf. Fig. 2 (a,b), while no damage was observed for L-shaped cantilevers, cf. Fig. 2 (c,d). Even for an engagement depth of 20 µm, static contact was maintained and no visible damage at the tip contact area was observed. The results are representative for several experiments and visible damage was in no cases observed with the L-shaped cantilevers.

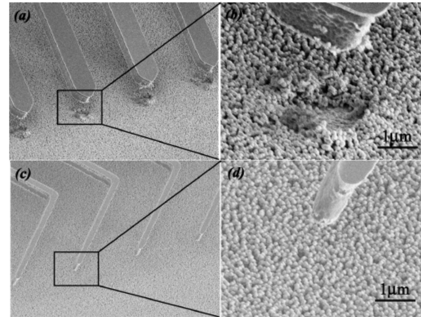

Figure 2: In-situ SEM images of M4PP measurements on TiW nanograss samples. (a,b) with engagement Δz of 1-2 µm, the straight cantilever probes leave large scrub marks with a radius of ~1 µm, (c,d) while the L-shaped cantilever probes leave no visible sample damage.

Table 1: Measurement repeatability on TiW nanograss with 65 measurement attempts for both probe types.

Cantilever type	Straight	L-shaped
Sheet conductance, G_S (S)	0.1835	0.1838
Standard deviation	0.55 %	0.12 %
Measurement yield[1]	76 %	97 %

[1] *Good measurements / measurement attempts*

Measurement repeatability

The measurement repeatability for the straight and L-shaped cantilevers is compared based on 65 measurement attempts (separate touchdowns with lateral steps of 5 µm) for both probe types; and the results are summarized in Table 1. The relative standard deviation in repeatability using L-shaped cantilevers is similar to that on planar thin film materials [15], whereas the straight cantilever probes exhibits a 1σ repeatability, which is five times larger. Both probe types measure the same mean sheet conductance since the sensitivity of dual configuration four-point probe measurements is very small at the probe contacts [16] where damage occurs for the straight cantilevers. In addition, the L-shaped cantilever probe shows a clear improvement in the measurement yield, reaching 97 % compared to 76 % for the straight cantilevers. The reduced measurement yield observed with the straight cantilevers is related to poor electrical contact and is most likely associated with nanograss fracturing.

Sample uniformity

Characterization of process uniformity and process control in manufacturing are interesting applications. For such applications the method must be sensitive to variations in surface morphology. Figure 3 shows an example of the radial variation in measured sheet conductance of a TiW coated high aspect ratio nanograss sample compared to a planar TiW coated reference sample. Small peak-to-peak sheet conductance variations of 4% are measured on the reference sample due to

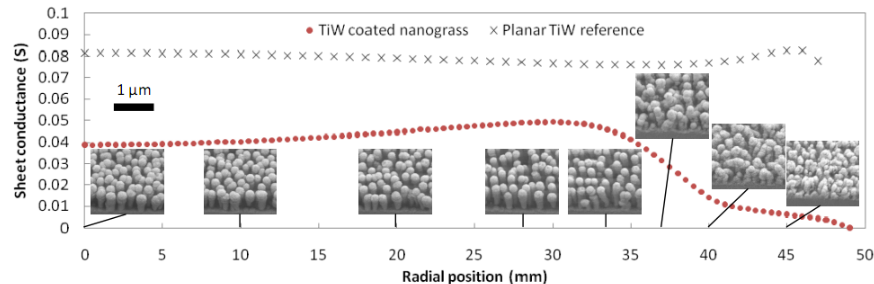

Figure 3: Sheet conductance characterization of nanograss uniformity (•) and a planar reference wafer (×) with conformally sputter-deposited TiW. SEM micrograph inserts with corresponding scale bar relates the change in sheet conductance to the nanoforest morphology which is radial symmetric on the wafer with origin in the wafer center.

process chamber shadowing effects. However, the reference sample variations are insignificant compared to the dominant variations on the nanograss sample which appear radial on the wafer. Radial process variations caused by plasma loading effects is a well known phenomenon [17] and it also affects the nanograss density and morphology as the micrograph inserts reveal. Several similar nanograss samples were processed with slightly different plasma parameter yielding different results, but the large sensitivity to variations is representative for all samples measured.

CONCLUSION

Four-point probe measurements have been proposed as an indirect method for characterization of surface morphology. A relative standard deviation in measurement repeatability of 0.12 % has been found, which is very close to measurement repeatability on planar conductive samples [15]. The method displays high sensitivity to variations in surface morphology and could be a possible metrology solution for process uniformity optimization and process monitoring. Non-destructive micro four-point measurements have been demonstrated with three-way flexible cantilever electrodes whereas conventional straight cantilevers leave large scrub marks at the electrode contacts on these fragile nanograss samples. The non-destructive contacts result in a measurement yield of 97 % which is a significant improvement compared to straight cantilevers (76 %).

ACKNOWLEDGEMENT

The authors would like to thank Helle V. Jensen (DTU Danchip) for fabrication of M4PPs. We are grateful for the financial support from the Danish Council for Independent Research : Technology and Production Sciences (FTP). Center for Individual Nanoparticle Functionality (CINF) is sponsored by The Danish National Research Foundation.

REFERENCES

[1] M. Law, L.E. Greene, J.C. Johnson, R. Saykally, P. Yang, "Nanowire dye-sensitized solar cells", Nature Mater. **4**, pp.455-459, 2005.

[2] S. Kumar, V. Gupta, K. Sreenivas, "Synthesis of photoconducting ZnO nano-needles using an unbalanced magnetron sputtered ZnO/Zn/ZnO multilayer structure", Nanotechnology **16**, pp.1167-1171, 2005.

[3] M.J. Zheng, L.D. Zhang, G.H. Li, W.Z. Shen, "Fabrication and optical properties of large-scale uniform zinc oxide nanowire arrays by one-step electrochemical deposition technique", Chem. Phys. Lett. **363**, pp.123-128, 2002.

[4] M.S. Schmidt, A. Boisen, J. Hubner, "Towards Easily Reproducible Nano-structured SERS Substrates", Proc. IEEE Sensors, pp.45-48, 2009.

[5] B. Bhushan, "Handbook of Nanotechnology", Springer, 2004.

[6] C.L. Petersen, T.M. Hansen, P. Boggild, A. Boisen, O. Hansen, T. Hassenkam, F. Grey, "Scanning microscopic four-point conductivity probes", Sensors and Actuators A **96**, pp.53-58, 2002.

[7] D.H. Petersen, O. Hansen, T.M. Hansen, P. Boggild, R. Lin, D. Kjaer, P.F. Nielsen, T. Clarysse, W. Vandervorst, E. Rosseel, N.S. Bennett, N.E.B. Cowern, "Review of electrical characterization of ultra-shallow junctions with micro four-point probes", J. Vac. Sci. Technol. B **28**, pp. C1C27-C1C33, 2010.

[8] T. Clarysse, A. Moussa, F. Leys, R. Loo, W. Vandervorst, M.C. Benjamin, R.J. Hillard, V.N. Faifer, M.I. Current, R. Lin, D.H. Petersen, "Accurate sheet resistance measurement on ultra-shallow profiles", Mater. Res. Soc. Symp. Proc. **912**, pp. 197-202 (2006).

[9] D.H. Petersen, O. Hansen, T.M. Hansen, P.R.E. Petersen, P. Boggild, "Static contact micro four-point probes with <11 nm positioning repeatability", Microelectron. Eng. **85**, pp.1092-1095, 2008.

[10] K. Fuchs, "The conductivity of thin metallic films according to the electron theory of metals", Proc. Camb. Phil. Soc. **34**, pp.100-108, 1938.

[11] E. H. Sondheimer, "The mean free path of electrons in metals," Adv. Phys. **50**, pp.499-537, 2001.

[12]O. Sardan, D.H. Petersen , K. Molhave, O. Sigmund, P. Boggild, "Topology optimized electrothermal polysilicon microgrippers", Microelectron. Eng. **85**, pp.1096-1099, 2008.

[13]L. J. Van der Pauw, "A method of measuring the resistivity and Hall coefficient on lamellae of arbitrary shape", Philips Tech. Rev. **20**, pp.220-224, 1958.

[14]R. Rymaszewski, "Relationship between the correction factor of the four-point probe value and the selection of potential and current electrodes", J. Phys. E **2**, pp.170-174, 1969.

[15]D. Kjaer, R. Lin, D.H. Petersen, P.M. Kopalidis, R. Eddy, D.A. Walker, W.F. Egelhoff, L. Pickert, "Micro four-point probe with high spatial resolution for ion implantation and ultra-shallow junction characterization", AIP Conf. Proc. **1066**, pp.167-170, 2008.

[16]F. Wang, D. H. Petersen, T. M. Hansen, T. R. Henriksen, P. Bøggild, and O. Hansen, "Sensitivity study of micro four-point probe measurements on small samples," . Vac. Sci. Technol. B **28**, pp.C1C34-C1C40, 2010.

[17]F. Chen and J. Chang, "Lecture Notes on Principles of Plasma Processing", Kluwer Academic / Plenum Publishers, 2003.

CONTACT

Dirch H. Petersen, Dirch.Petersen@nanotech.dtu.dk or
Fei Wang, Fei.Wang@nanotech.dtu.dk

C.3 Direct Electrospinning of Ag-Polyvinylpyrrolidone Nanocables

Nanoscale

Dynamic Article Links

Cite this: *Nanoscale*, 2011, **3**, 4966

www.rsc.org/nanoscale

PAPER

Direct electrospinning of Ag/polyvinylpyrrolidone nanocables

Jie Song,[ab] Menglin Chen,[a] Mikkel Buster Olesen,[d] Chenxuan Wang,[c] Rasmus Havelund,[a] Qiang Li,[a] Erqing Xie,[b] Rong Yang,[c] Peter Bøggild,[d] Chen Wang,[c] Flemming Besenbacher[a] and Mingdong Dong*[a]

Received 19th May 2011, Accepted 8th September 2011
DOI: 10.1039/c1nr10512d

Core–sheath silver nanowire/polyvinylpyrrolidone (AgNW/PVP) nanocables have been fabricated *via* an efficient single-spinneret electrospinning method. The core–sheath structure is revealed by combining several characterization methods. A possible formation mechanism of the AgNW/PVP nanocable involving a strong stretching during the electrospinning process is proposed. Further, electrical measurements were performed on AgNW/PVP nanocables as well as bare AgNWs, which indicated the nanocables became insulating due to the isolation of highly conductive AgNWs by insulating PVP sheath. Therefore, the described fabrication method holds potential for the fabrication of low-cost metal/polymer composite materials for nanoelectronic applications in general.

1. Introduction

One-dimensional (1D) metal nanorods and nanowires hold interesting applications in the area of nanoelectronics because of their potential use as interconnects in nano-optoelectronic devices.[1,2] However, surface effects from contaminants and oxidation may strongly influence the performance of such metallic nanowires. Contamination of the metallic nanowires can be prevented by enclosing the nanowires in an insulating sheath.[3,4] Numerous synthetic methods for the formation of such nanocables have been developed, including reactive laser ablation,[3] sol–gel process,[4,5] thermal reduction route,[6,7] surface modification[8,9] and electrochemical deposition.[10–12] Nevertheless, they either are often high cost or require a complicated multi-step process, and thus have limited success in large scale processing which can be extended to wide applications.

Electrospinning is a remarkably simple and versatile technique capable of generating composite fibers with various sizes ranging from nano to micro-scale.[13] In our previous studies, we have demonstrated the capability of the electrospinning technique in the synthesis of semiconductor/semiconductor,[14] semiconductor/metal,[15] and insulator/insulator[16] core–sheath composite electrospun nanofibers. As for metal/insulator core–sheath nanofibers, nanocables, Sun *et al.*[17] fabricated platinum/poly-(L-lactide) (Pd/PLA) core–sheath nanofibers through coaxial electrospinning, while Li *et al.*[18] developed an electrostatic force induced electrospinning method to grow copper/poly(vinyl alcohol) (Cu/PVA) core–sheath nanofibers. However, it seems there is no report about the silver (Ag) related nanocable using the electrospinning method.

Ag nanowires and Ag-related nanowires with well-defined dimensions are particularly interesting to synthesize and study because of their intriguing electrical, thermal, and optical properties.[2] Obviously, the nanocable with Ag nanowires as core will present very exciting properties for wide applications. Currently, the nanocables with Ag nanowires were mainly synthesized through surface modification with different molecules, which provide appropriate surface affinity compatible for making metal/dielectric core/shell nanowires.[4,19] However, the applications of such nanocables are still immature, because the essential conductive property of the core metallic nanowires should not be ignored except for special applications requiring exposed surfaces.

Here, we present a new route to fabricate silver nanowires (AgNWs) with a polyvinylpyrrolidone (PVP) shell *via* a single-spinneret electrospinning method. The structure of the AgNW/PVP nanocables can be clearly identified by scanning electron microscopy (SEM) by increasing the energy of the electron beam, combined with X-ray photoelectron spectroscopy (XPS) data. In addition, the effect of different AgNW concentrations and different diameters of the AgNW/PVP nanocable was investigated to explore the formation of AgNW/PVP nanocables during the electrospinning process. Based on the results, a tentative formation mechanism was proposed. Furthermore, electrical measurements were performed on AgNW/PVP nanocables as well as bare Ag nanowires.

2. Experimental

2.1 Synthesis of Ag nanowires (AgNWs)

The AgNWs were synthesized by a modified solution processing technique as reported by Xia *et al.*[20,21] A mixture of 0.792 g PVP

[a]*Interdisciplinary Nanoscience Center (iNANO), Department of Physics and Astronomy, Aarhus University, Aarhus C, DK-8000, Denmark. E-mail: Dong@inano.au.dk*
[b]*School of Physical Science and Technology, Lanzhou University, Lanzhou, 730000, People's Republic of China*
[c]*National Center for Nanoscience and Technology (NCNST), Beijing, 100190, People's Republic of China*
[d]*Denmark DTU Nanotech, Technical University of Denmark, DK-2800 Kgs Lyngby, Denmark*

This journal is © The Royal Society of Chemistry 2011

(poly(vinylpyrrolidone), $M_w \approx$ 1 300 000, Sigma) and 32 ml ethylene glycol (≥99%, Sigma-Aldrich) was heated and kept at 160 °C. Then, 0.204 g $AgNO_3$ (silver nitrate, 99%, Sigma-Aldrich) dissolved in 12 ml ethylene glycol was injected into the above refluxed mixture at a rate of ~0.6 ml min^{-1}. After injection, the reaction mixture was kept under vigorous magnetic stirring and further refluxed for an additional 60 min to ensure that the growth was complete. The AgNWs could be recovered from ethylene glycol through centrifugation and were then redispersed in ethanol.

2.2 Electrospinning of AgNW/PVP composite nanofibers

Fig. 1 illustrates the entire electrospinning process: the first two steps were to prepare the precursor solutions. AgNWs were dispersed in ethanol through a 10 min supersonic treatment prior to being added to the polymer solutions. The precursor solutions were then prepared by dissolving 0.1 or 0.25 g PVP in 2 ml ethanol dispersed with 0%, 0.175%, 0.7% and 2.8% (w/v) AgNWs at room temperature and stirring for 12 h. These homogeneous suspensions were subsequently placed in a 5 ml syringe fitted with a metallic needle of 0.4 mm inner diameter. The syringe was fixed horizontally on a syringe pump (Model: KDS 101, KD Scientific) and an electrode of a high voltage power supply (Spellman High Voltage Electronics Corporation, MP Series) was clamped to the metal needle tip. The flow rate of the solution was 1 ml h^{-1}, and the applied voltage was 15 kV. The tip-to-collector distance was set to 20 cm, and either aluminium foil or silicon wafer was used for the collection of the electrospun fibers.

2.3 Characterization of the nanofibers

The morphology of the composite nanofibers was determined by high-resolution SEM (FEI, Nova 600 NanoSEM). Here, in particular, the SEM was operated in both low-voltage (5 kV) and high-voltage (10 kV) mode to obtain the charge contrast imaging data. Besides, transmission electron microscopy (TEM) (Tecnai G2 F20 U-TWIN, 200 kV) was applied to reveal the micro and nanostructures of the samples. The structural properties of the samples were further investigated by X-ray diffraction (XRD) on a Bruker D8 diffractometer using the Bragg–Brentano geometry ($\theta/2\theta$) Cu Kα radiation. The surface chemistry was probed by X-ray photoelectron spectroscopy (XPS) using a Kratos Axis Ultra^{DLD} instrument equipped with a monochromated Al Kα X-ray source ($h\nu$ = 1486.6 eV) operating at 10 kV and 15 mA (15 W). Wide energy survey scans were obtained over the range of 0–900 eV binding energy (BE) at a pass energy of 160 eV.

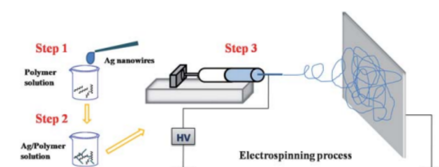

Fig. 1 Schematic illustration of the composite fiber formation using the electrospinning process.

2.4 Electrical measurements of AgNW/PVP nanocables

The micro-four point probes used for the electrical measurements consist of four silicon dioxide cantilevers coated with the 100/1000 Å Ti/Au electrode layer, extending over the edge of a silicon chip.[22] The electrode pitch in all experiments here was 1.5 μm. The probes are mounted in a SmarAct micromanipulator, placed inside a FEI Quanta 200 FEG Environmental Scanning Electron Microscope (ESEM), which allows control of the environmental conditions. Prior to each electrical measurement, the probes were tested by determining the resistivity of a 500 Å thick Au reference film. Electrical measurements of transport property were performed by placing the bare Ag nanowires as well as AgNW/PVP nanocables on a silicon dioxide insulating surface, locating the nanowires in the ESEM, and finally aligning the micro-four point probes to the samples.

3. Results and discussion

Fig. 2 shows the morphologies of purified AgNWs after centrifugation. The AgNWs were relatively uniform with lengths upto 10 μm, as shown in the SEM image of Fig. 2a. Based on statistical analysis of low-magnification TEM images (Fig. 2b), the mean diameter of AgNWs was found to be ~80 ± 17 nm. Fig. 2c shows a representative individual AgNW with a diameter of ~98 nm. Further studies by high resolution TEM image (Fig. 2d) and selected-area electron diffraction (the inset of Fig. 2d) showed that the nanowires were single crystalline.

Upon electrospinning, the AgNWs were expected to be aligned along the fiber axis inside the nanofibers. Fig. 3a shows representative SEM images of the sample with an AgNW

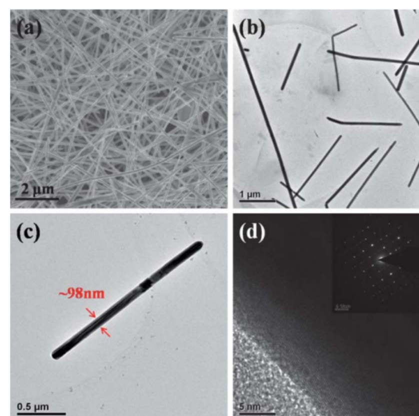

Fig. 2 (a) SEM and (b) TEM images of uniform silver nanowires. (c) The TEM image of an individual silver nanowire with the diameter of ~98 nm, and (d) a high-resolution TEM image. The selected-area electron diffraction pattern (the inset of d) shows that the nanowires are single crystalline.

This journal is © The Royal Society of Chemistry 2011

concentration of 0.7% (w/v). The typical electrospun composite nanofibers had diameters from about 100 nm to 500 nm. However, no further information could be revealed in Fig. 3a, especially for the presence of AgNWs. Therefore, charge contrast SEM was applied in order to determine the AgNW location in the nanofibers. Clear brightness contrasts were observed in the marked spots 1, 2, 3 and 1′, 2′, 3′ in Fig. 3a (operated at 5 kV) and Fig. 3b (operated at 10 kV). The inset of Fig. 3 shows larger magnification SEM images of spot 3 (and 3′). Due to the difference in electron charge transport properties between the conductive AgNWs and the insulating PVP polymer matrix, the secondary electron yield was enriched at the location of the AgNWs, in particular for higher electron beam energies.[23,24] Therefore, the brightness variations visible in the SEM charge contrast images could be related to the position of AgNWs in the sample. It is very important to identify the position of AgNWs in the PVP matrix in order to have accurate electrical measurements of AgNW/PVP composite materials. The SEM images confirm that the AgNWs were successfully incorporated into the PVP polymer matrix. This observation shows that using charge contrast imaging at high acceleration voltage, we are able to gain detailed information on the three-dimensional (3D) morphology of the conductive AgNWs in polymer fibers. So, all the SEM images of the remaining samples were obtained using the acceleration voltage of 10 kV. AgNWs are distributed sporadically within the PVP matrix. However, in order to reveal whether the AgNWs have been well embedded in the polymer fiber matrix, further studies were carried out to investigate the AgNW/PVP nanocables in more detail. Fig. 3c shows an XRD pattern of the nanofibers. The peaks at 2θ values of 38.20°, 44.40° and 64.60° (marked with ▼) are indexed to the face centered cubic (fcc) phase of silver, which further supports that the AgNW was successfully added into the PVP polymer matrix. Very interestingly, the XPS data show that no silver was present at the surface of the nanofibers. Fig. 3d shows the wide energy survey spectra acquired from an area of app. 300 μm × 700 μm. Only peaks related to C, N, and O appeared in the spectrum. By combining the charge contrast SEM images, XRD, and XPS data, it could be concluded that the AgNWs were completely embedded in the PVP nanofibers, at least deeper than 10 nm, which was the probe depth for XPS. This implies that we have successfully synthesized AgNW/PVP nanocables with the AgNW embedded inside as the core and PVP outside as the shell, as shown in the inset of Fig. 3d. These nanocables may potentially be used for fabricating low-cost metal/polymer composite materials for nanoelectronic applications in general.

To obtain a microscopic understanding of the synthesis process of the AgNW/PVP composite nanofiber in more detail, the effect of different AgNW concentrations on the fiber diameter was investigated. The photographs of 5% (w/v) PVP precursor solutions with 0%, 0.175%, 0.7%, and 2.8% (w/v) AgNWs are shown in Fig. 4. When more AgNWs were added to the precursor solution, more sedimentation appeared at the bottom of the solution vials. The SEM images of the nanofibers electrospun from different AgNW concentrations are shown in Fig. 4. Upon increasing the AgNW concentration, more and more AgNWs were observed in the fibers. No significant difference in the fiber diameter was observed upon addition of different AgNW concentrations which suggests that AgNWs have only little effect on fiber morphologies.

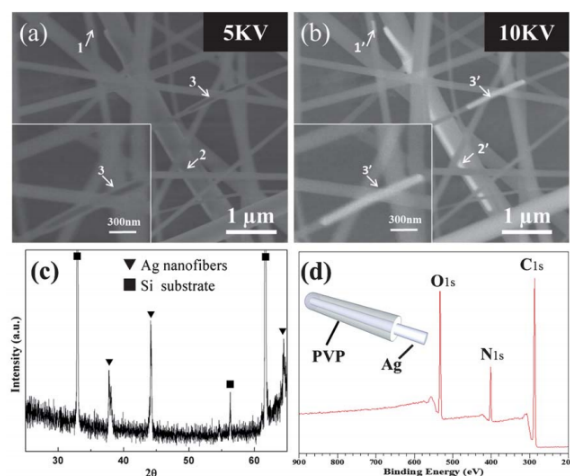

Fig. 3 Charge contrast SEM images of the same region of the AgNW/PVP composite nanofibers using (a) 5 kV and (b) 10 kV acceleration voltages. (c) XRD data confirming the presence of Ag in the AgNW/PVP nanocables. (d) XPS wide energy survey spectrum showing the elemental composition of the surface of the composite nanofibers. The above results show that the formed AgNW/PVP nanocable is corresponding with the ideal nanocable model (the inset of d).

This journal is © The Royal Society of Chemistry 2011

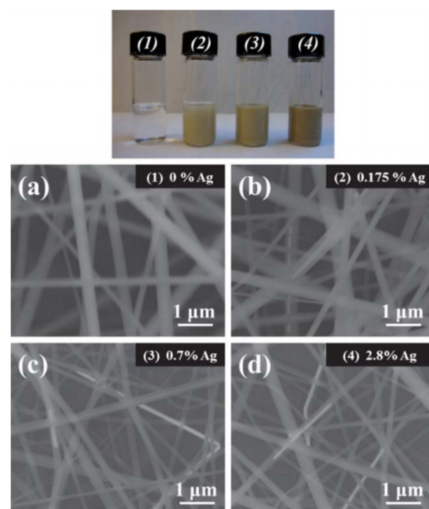

Fig. 4 Photograph of 5% (w/v) PVP precursor solutions with 0%, 0.175%, 0.7%, and 2.8% (w/v) AgNWs and the corresponding SEM images, (a), (b), (c), and (d), respectively.

While the effect of the AgNW concentration on the fiber morphologies appears insignificant, the fiber size influences the positioning of the AgNWs in the fibers. Fig. 5a and d show SEM images of pure PVP fibers prepared from the solutions with different PVP concentrations. The diameters of the fibers from the solution with 12.5% (w/v) PVP were in the low micrometre scale (~900 nm, Fig. 5a), while fibers from the 5% (w/v) solution were in the nanometre scale (~150 nm, Fig. 5d). After adding the same amount of AgNWs (2.8% w/v) to the two precursor solutions, a difference in the AgNW positioning was observed. For the fibers with larger diameters (Fig. 5b), multiple AgNWs were found to be located side by side within the polymer matrix. However, for the thinner fibers (Fig. 5e), no parallel arrangement of AgNWs was observed.

TEM studies were used to further explore the microstructure of AgNW/PVP composite fibers. Fig. 5c shows a single composite microfiber with four parallel AgNWs. The AgNWs were randomly distributed and near randomly oriented within the polymer matrix of the microfibers. However, when the diameter decreased in the nanometre scale, the AgNWs were well aligned along the axis of the composite electrospun-fiber as shown in Fig. 5f. The fiber segment represents an ideal nanocable with an AgNW as the core and PVP as the sheath. The results clearly demonstrate that the alignment of the AgNWs in the nanocable depends strongly on the diameter of the electrospun fibers.

The TEM image in Fig. 6 shows a single fiber with a varying fiber diameter from >1.5 μm at the segment marked I, through a medium diameter at segment II, to a < 1.0 μm at segment III. The trend on how the AgNWs are positioned from a–c indicates a possible mechanism for the formation of the AgNW/PVP nanocable. Comparing to the CNT, AgNWs are rigid metallic wires and have an inherent linear structure. The AgNWs appear to be well-oriented along the fiber axis, the same as the CNT/PS system. However the CNT/PS nanocables show the irregularly twisted and curled nanotubes in the spun dispersion.[25] The mechanism is schematically presented in Fig. 6. The essence of the electrospinning process is to generate a continuous jet from a liquid droplet by charging the surface of the droplet.[13] While the jet travels through the air, the diameter of the jet gradually decreases as a result of solvent evaporation and continuous stretching of the jet caused by electrostatic repulsion between the

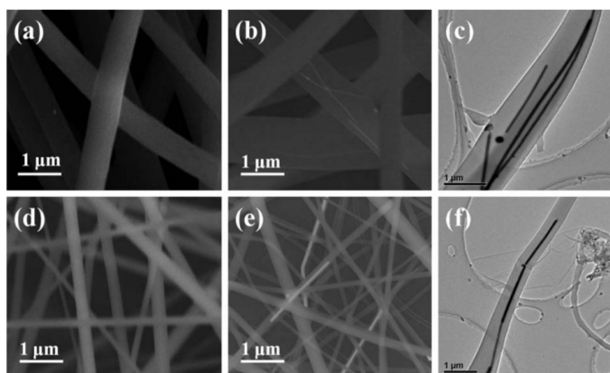

Fig. 5 (a) and (d) SEM images of the electrospun fibers with 12.5% and 5% (w/v) PVP concentrations but without any AgNWs, (b) and (e) with 2.8% (w/v) AgNWs, and (c) and (f) TEM images of electrospun fibers with 12.5% and 5% (w/v) PVP and 2.8% (w/v) AgNWs.

This journal is © The Royal Society of Chemistry 2011

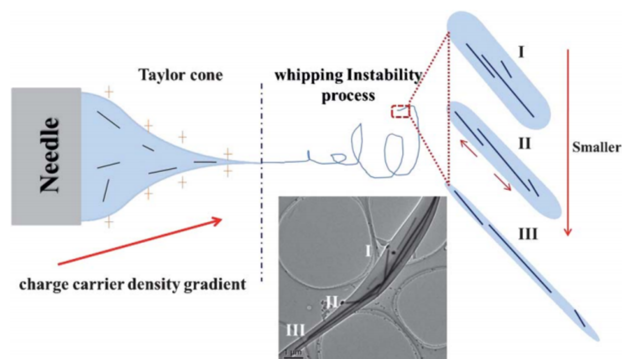

Fig. 6 Schematic representation of the formation of the AgNW/PVP nanocable.

charges on the jet. At the same time, the jet path is looped due to the whipping instability originating from the electrostatic interactions between the external electric field and the surface charges on the jet.[26,27]

When rigid nanowires such as the AgNWs are present in the polymer solution, the overall axial flow of solution involved in the stretching of the jet induces alignment of the nanowires along the axis of the jet. At the same time, the stretching disperses the AgNWs along the length of the jet. For dilute polymer solutions the alignment and dispersion are enhanced by a faster stretching combined with a higher mobility of the AgNWs. This observation is in agreement with another report, which indicated that the surface Gibbs free energy favors a smooth jet with polymer at the surface.[28] The position of the AgNWs in a jet is confined by the TEM. This effect plays an important role in the alignment of AgNWs, especially when the diameter becomes comparable to the length of the AgNWs (indicated in Fig. 6I–III).

Sequentially, electrical measurements were performed using the home-built four-probe method. In this case, an individual Ag nanowire of ~120 nm in diameter and ~8 μm in length was aligned on silicon dioxide substrate across four-probe electrodes, as show in the inset of Fig. 7. A current of upto 1 mA was passed through the two outer probes, while the voltage drop across the two inner probes was monitored using a National Instrument Data Acquisition Card (DAQ). As shown in Fig. 7, a linear *I–V* curve was obtained, from which an electrical conductivity of approximately 0.5×10^5 S cm^{-1} was calculated for this Ag nanowire. Additional measurements on Ag nanowires were obtained, and the conductivity of those nanowires was $\sim 0.3 \times 10^5$ S cm^{-1}. The conductivities based on four-probe measurements are comparable to values of 0.8×10^5 S cm^{-1} obtained by Xia's group.[13] It indicates that the single crystal Ag nanowires show excellent conductivity property, which is promising for the future applications of AgNW nanocables in the area of nanoelectronics.

Furthermore, the AgNW/PVP nanocables were also aligned on the silicon dioxide substrate across four probe electrodes and tested by the same method. A fixed source current of 1 μA was set

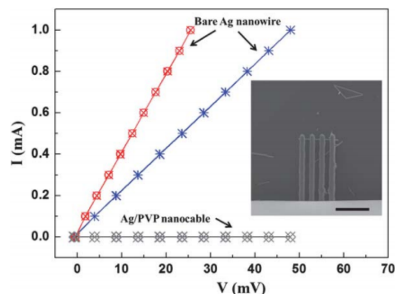

Fig. 7 *I–V* characteristics of two different Ag nanowires showing a resistance of 49 and 26 ohms, corresponding to a conductivity of 0.3–0.5 $\times$ 10^5 S cm^{-1}. But for the AgNW/PVP nanocable, no current passed through the insulated wires, upto 50 mV. Inset: SEM image of micro-four point probes measuring on Ag nanowires. The scale bar is 5 μm.

between the outer probes, while the compliance voltage was stepwise increased from 1 V to 50 V. It was not possible to pass any current through the insulated wires upto 50 V, as shown in Fig. 7. Therefore, the above results illustrated that the PVP shell in the AgNW/PVP was insulating and effective for the Ag nanowires to be an ideal nanocable.

4. Conclusion

We have demonstrated a novel and facile way to fabricate AgNW/PVP nanocables. Uniform AgNWs with excellent conductivity were synthesized in large scale by a soft, solution-phase approach and embedded in a polymer matrix by electrospinning. Based on charge contrast SEM and TEM data, a possible formation mechanism of the AgNW/PVP nanocable was proposed. The stretching of the electrospinning jet induced the AgNWs to be well aligned along the axis of the composite

This journal is © The Royal Society of Chemistry 2011

electrospun fiber. Further, by combining XRD and XPS analysis, it was confirmed that the AgNWs were embedded in the PVP matrix, forming a core–sheath nanocable structure. Furthermore, electrical measurements were performed on AgNW/PVP nanocables as well as bare Ag nanowires, which indicated the PVP shell was insulating for isolating Ag nanowires with a conductivity of approximately 0.5×10^5 S cm^{-1}. Such nanocables comprising nanowires in an insulating sheath may serve as important components in nanoelectronic devices. It is also possible to use this method to fabricate other composite nanomaterials for applications such as nanometre-scale electronics, optoelectronics, and sensing devices.

Acknowledgements

We gratefully acknowledge the financial support from the Danish Natural Science Research Councils and the Danish Ministry for Science and Innovation through the iNANO Center. M.D. acknowledges a STENO grant from the Danish Research Council. J.S. acknowledges PhD Scholarship from China Scholarship Council of the Ministry of Education of China. We sincerely thank Professor Seeram Ramakrishna (National University of Singapore) for fruitful discussions and suggestions.

References

1 Y. Xia, P. Yang, Y. Sun, Y. Wu, B. Mayers, B. Gates, Y. Yin, F. Kim and H. Yan, *Adv. Mater.*, 2003, **15**, 353–389.
2 Y. Sun, *Nanoscale*, 2010, **2**, 1626–1642.
3 Y. Zhang, K. Suenaga, C. Colliex and S. Iijima, *Science*, 1998, **281**, 973–975.
4 Y. Yin, Y. Lu, Y. Sun and Y. Xia, *Nano Lett.*, 2002, **2**, 427–430.
5 S. Xie, F. Ma, Y. Liu and J. Li, *Nanoscale*, 2011, **3**, 3152–3158.
6 J. Q. Hu, Q. Li, X. M. Meng, C. S. Lee and S. T. Lee, *Chem. Mater.*, 2003, **15**, 305–308.
7 P. Zhang, C. Shao, Z. Zhang, M. Zhang, J. Mu, Z. Guo and Y. Liu, *Nanoscale*, 2011, **3**, 2943–2949.
8 D. Sun, J. Yang and X. Wang, *Nanoscale*, 2010, **2**, 287–292.
9 J. A. Sioss, R. L. Stoermer, M. Y. Sha and C. D. Keating, *Langmuir*, 2007, **23**, 11334–11341.
10 J. Ku, R. Vidu, R. Talroze and P. Stroeve, *J. Am. Chem. Soc.*, 2004, **126**, 15022–15023.
11 Z. Wang, R. Guo, G. Li, L. Ding, Y. Ou and Y. Tong, *RSC Adv.*, 2011, **1**, 48–51.
12 G. Li, Z. Wang, F. Zheng, Y. Ou and Y. Tong, *J. Mater. Chem.*, 2011, **21**, 4217–4221.
13 D. Li and Y. Xia, *Adv. Mater.*, 2004, **16**, 1151–1170.
14 J. Song, J. Zhou, W. Wang, Y. Liu, X. Li, X. Xu, X. An and E. Xie, *J. Phys. Chem. C*, 2010, **114**, 10761–10767.
15 J. Song, X. An, J. Zhou, Y. Liu, W. Wang, X. Li, W. Lan and E. Xie, *Appl. Phys. Lett.*, 2010, **97**, 122103.
16 M. Chen, M. Dong, R. Havelund, V. R. Regina, R. L. Meyer, F. Besenbacher and P. Kingshott, *Chem. Mater.*, 2010, **22**, 4214–4221.
17 Z. Sun, E. Zussman, A. L. Yarin, J. H. Wendorff and A. Greiner, *Adv. Mater.*, 2003, **15**, 1929–1932.
18 Z. Li, H. Huang and C. Wang, *Macromol. Rapid Commun.*, 2006, **27**, 152–155.
19 S. E. Hunyadi and C. J. Murphy, *J. Phys. Chem. B*, 2006, **110**, 7226–7231.
20 Y. Sun, B. Gates, B. Mayers and Y. Xia, *Nano Lett.*, 2002, **2**, 165–168.
21 Y. Sun and Y. Xia, *Adv. Mater.*, 2002, **14**, 833–837.
22 C. L. Petersen, F. Grey, I. Shiraki and S. Hasegawa, *Appl. Phys. Lett.*, 2000, **77**, 3782–3784.
23 K. T. Chung, J. H. Reisner and E. R. Campbell, *J. Appl. Phys.*, 1983, **54**, 6099–6112.
24 J. Loos, A. Alexeev, N. Grossiord, C. E. Koning and O. Regev, *Ultramicroscopy*, 2005, **104**, 160–167.
25 Y. Dror, W. Salalha, R. L. Khalfin, Y. Cohen, A. L. Yarin and E. Zussman, *Langmuir*, 2003, **19**, 7012–7020.
26 Y. M. Shin, M. M. Hohman, M. P. Brenner and G. C. Rutledge, *Polymer*, 2001, **42**, 9955–9967.
27 A. L. Yarin, S. Koombhongse and D. H. Reneker, *J. Appl. Phys.*, 2001, **89**, 3018–3026.
28 D. He, B. Hu, Q. Yao, K. Wang and S. Yu, *ACS Nano*, 2009, **3**, 3993–4002.

This journal is © The Royal Society of Chemistry 2011

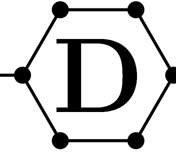

Patents

D.1 Automatic Identification of Single- and/or Few-layer Thin-Film Material

The following patent was written and formulated in cooperation with European Patent Attorney David Hendriksen, partner at Plougmann & Vingtoft, and was filed to the European Patent Office on the 13th of August 2012. The first author of the patent is Bjarke Sørensen Jessen.

AUTOMATIC IDENTIFICATION OF SINGLE- AND/OR FEW-LAYER THIN-FILM MATERIAL.

FIELD OF THE INVENTION

5 The present invention relates to a method of and a system for automatic identification of a digital representation of layered thin-film material, e.g. single-, and/or few-layer graphene, in a digital image.

Few-layer is to be understood to comprise up to 10 layers or more. Few-layer
10 in this context specifically comprises single-, bi-, tri-, and four-layer.

BACKGROUND OF THE INVENTION

Graphene is a two dimensional material comprising a single layer of carbon atoms arranged in a honeycomb grid. It has many advantageous room
15 temperature properties like almost twice the electrical conductivity of copper, more than ten times the thermal conductivity of silver, almost thirty times the electron mobility of silicon, about 5 times the tensile or Young's modulus of steel, and more than 45 times the tensile strength of diamond.

20 These properties enable many uses and improvements when using graphene.

High quality graphene may e.g. be obtained by a technique usually referred to as micro-cleaving or micro-mechanically cleaving or various exfoliation
25 methods.

Alternatively, graphene can be 'grown' using chemical vapour deposition (CVD) methods. However, a drawback of CVD is that graphene typically is 'grown' on copper or nickel and then need to be moved to another usable
30 substrate using a so-called transfer technique. Furthermore, each coherent area of graphene obtained in this way is relatively small, i.e. CVD graphene can be seen as comprising a larger number of much smaller adjacent graphene areas.

35 Graphene has a thickness of only 0.335 nm whereby characterization tools involving equipment such as atomic force microscope (AFM), scanning

tunneling microscope (STM), or scanning electron microscope (SEM) often is used to properly and reliably identify graphene. However, using these techniques is time consuming and the equipment is also relatively costly.

5 Furthermore, given that coverage of research or similar grade single-layer micro-cleaved graphene is typically only some few thousand μm^2 on a 4" wafer or similar, such time consuming identification methods are not practical for large-scale production or research use.

10 Alternatively, manual identification of graphene – which is still used – is slow, tedious and/or error-prone, especially for fragmented samples. Typical time spent on manual identification of graphene is e.g. about 5 seconds pr. digital image and about 6 – 7 hours for a 4" wafer when digitised at an appropriate resolution needed to properly identify graphene.

15

Patent application US 2011/0299720 discloses to an automated approach for determining a number of atomic planes in layered material samples. According to one aspect, calibration is carried out for a thin film material under specific illumination conditions where a correlation is determined

20 between the number of layers of the layered thin film material and a range of colour component values. The correlation is then used to determine the number of layers in a selected region of an image for another sample comprising the same material as used during the calibration. For accurate results, the image needs to be captured under the same illumination

25 conditions as used during the calibration.

Calibration is carried out e.g. using micro-Raman spectroscopy and atomic force microscopy (AFM).

30 Once the calibration is carried out, it may be used for layer detection for other samples as long as the sample material and the calibration material is the same, the substrate for the calibration material and for the sample material is the same, and the illumination conditions stay the same.

However, it is not practically simple ensuring that illumination conditions truly stay the same and a given sample material will always have small variations e.g. in thickness, even across the sample material.

5 Thus, there is a need for an automated simple, reliable, robust, and/or efficient way of identifying graphene and/or other thin-film materials in a digital image.

OBJECT AND SUMMARY OF THE INVENTION

10 It is an object to enable automated robust and reliable identification of graphene and/or other thin-film materials..

A further object is to enable this identification in a simple and/or efficient way.

15 According to one aspect, one or more of these objects are achieved at least to an extent by a method of automatically identifying one or more digital representations of single- and/or few-layer thin-film material in a digital image, the digital image having a predetermined number of colour components, and the method comprising

20 – determining a background colour component of the digital image for each colour component, and
– determining or estimating a colour component of thin-film material to be identified in the digital image for each colour component, the thin-film material to be identified having a given number of layers being at 25 least one,

wherein determining or estimating a colour component of thin-film material to be identified in the digital image for each colour component comprises

– obtaining a pre-determined contrast value for each colour component and determining or estimating the colour component of the thin-film 30 material to be identified and having the given number of layers for each colour component by, for each colour component, multiplying a numerical difference between the pre-determined contrast value for a given colour component and about 1 with the background colour component for the given colour component,

35 and wherein the method further comprises

4

- identifying one or more digital representations of single- and/or few-layer thin-film material as points or parts of the digital image that, for each colour component, has a colour component being within a predetermined range of the determined or estimated colour component of the thin-film material to be identified having the given number of layers.

In this way, robust and reliable identification of layered thin-film material in a digital image is provided since identification is made based on the actual colour of the background and then the actual colour of the thin-film material is derived using information about contrasts.

Furthermore, this is provided without the need for calibration involving expensive and/or time-consuming equipment like such as atomic force microscope (AFM), scanning tunneling microscope (STM), or scanning electron microscope (SEM).

Additionally, the identification works on digital images obtained by relatively cheap and standard equipment.

This identification may be used on all types of layered thin-film materials, where a given contrast corresponds to a given layer, e.g. single-layer, of the thin-film material. For graphene, it is currently possible to distinguish at least 10 layers. For other thin-film materials, it may be possible to distinguish even more layers and of course also fewer.

In one embodiment, the thin-film material is graphene.

In one embodiment, the thin-film material is any one selected from the group of

- molybdenum disulphide,
- hexagonal boron nitride,
- Sb_2Te_3,
- $MoTe_2$,
- WS_2,
- $MoSe_2$,

- $TaSe_2$,
- Bi_2Te_3
- $NbSe_2$, and
- $NiTe_2$.

5

It is to be understood that other types of layered thin-film materials may also be identified in a similar way.

In one embodiment, the digital image is a grey-scale image or is converted
10 into a grey-scale image and the number of colour components is one.

In an alternative embodiment, the digital image is a colour image and the number of colour components is three or more.

15 In one embodiment, the method comprises identification of one or more digital representations of single- and/or few-layer thin-film material in a series of digital images, wherein

- determining a background colour component of the digital image for each colour component, and/or
- 20 determining or estimating a colour component of thin-film material to be identified in the digital image for each colour component,

is done for each digital image of the series or is done once where the determination(s) are used for later digital images of the series.

25 It is more exact to determine the background colour and/or the colour of the thin-film material for each image but to do either or both only once and use the determined value(s) is simpler and may be fully sufficient for certain uses.

In one embodiment, the thin-film material of the digital image was located on
30 a given substrate, having a predetermined thickness, when the digital image was captured and wherein determining a background colour component of the digital image for each colour component comprises

- providing predetermined information of an approximate range of a background colour component for each colour component as a
35 function of the particular type and a thickness of the given substrate.

In one embodiment, the method further comprises

- applying a filter (302), e.g. a median filter, to the digital image to remove high-frequency noise and/or salt-and-pepper noise before determining a background colour component of the digital image for
5 each colour component,
- applying one or more dilation steps followed by one or more erosion steps in order to improve the quality of the digital image for identification of thin-film material,
- applying a threshold where all pixels of the digital image are discarded
10 except those pixels that have, for each colour component, a colour component being within a second predetermined range of the determined or estimated colour component of the thin-film material to be identified having the given number of layers, and/or
- detecting edges or a contour of at least one part of the digital image
15 that has been identified to be one or more digital representations of single- and/or few-layer thin-film material.

According to another aspect, the invention also relates to a system for automatic identification of one or more digital representations of single-
20 and/or few-layer thin-film material in a digital image, the digital image having a predetermined number of colour components, wherein the system comprises one or more processing units adapted to

- determine a background colour component of the digital image for each colour component, and
25 - determine or estimate a colour component of thin-film material to be identified in the digital image for each colour component, the thin-film material to be identified having a given number of layers being at least one,

wherein one or more processing units is adapted to determine or estimate a
30 colour component of thin-film material to be identified in the digital image for each colour component by

- obtaining a pre-determined contrast value (C_R; C_G; C_B) for each colour component and determining or estimating the colour component of the thin-film material to be identified and having the given number of
35 layers for each colour component by, for each colour component, multiplying a numerical difference between the pre-determined

contrast value (C_R; C_G; C_B) for a given colour component and about 1 with the background colour component for the given colour component,

and wherein the one or more processing units is further adapted to

5 – identify one or more digital representations of single- and/or few-layer thin-film material as points or parts of the digital image that, for each colour component, has a colour component being within a predetermined range of the determined or estimated colour component of the thin-film material to be identified having the given

10 number of layers.

The system and embodiments thereof correspond to the method and embodiments thereof and have the same advantages for the same reasons.

15 **BRIEF DESCRIPTION OF THE DRAWINGS**

These and other aspects will be apparent from and elucidated with reference to the illustrative embodiments as shown in the drawings, in which:

Figure 1 illustrates a digital image of a substrate comprising single-layer and

20 bi-layer graphene;

Figure 2 schematically illustrates a flow-chart of one embodiment of a thin-film material identification method;

25 Figure 3 schematically illustrates a graph of pixel histograms of each colour component obtained for the image of Figure 1;

Figure 4 schematically illustrates the image of Figure 1 after (optional) image processing removing so-called salt-and-pepper noise without blurring edges

30 in the image;

Figures 5a – 5f schematically illustrate the effect of (optional) additional image processing of the image of Figure 1;

35 Figure 6 schematically illustrates the image of Figure 1 after single-layer graphene has been identified and non-graphene has been removed;

Figure 7 schematically illustrates Figure 6 after some additional image processing removing noise and/or artefacts;

5 Figure 8 schematically illustrates the image of Figure 1 after bi-layer graphene has been identified and non-graphene has been removed;

Figure 9 schematically illustrates Figure 8 after some additional image processing removing noise and/or artefacts;

10

Figure 10 schematically illustrates the end result of processing the image of Figure 1 showing both identified single- and bi-layer graphene; and

Figure 11 schematically illustrates one embodiment of a system for automatic
15 identification of a digital representation of single-, bi-, and/or few-layer thin-film material, e.g. graphene, in a digital image.

DESCRIPTION OF PREFERRED EMBODIMENTS

Figure 1 illustrates a digital image of a substrate comprising single-layer and
20 bi-layer graphene obtained by a more or less standard optical microscope. The figure shows a digital representation of a substrate comprising – in this particular example – single-layer graphene 101 as well as bi- 102 and many-layer graphene 103. Many-layer graphene is also referred to as graphite, and is typically considered as graphene with more than 10 layers. Also shown is a
25 shadow 105 cast by a larger piece of many-layer graphene.

This particular exemplary digital image 100 is a segment or part of a larger digital image.

30 The image also shows (optional) metal index marks or other types of index marks 104, typically physically present on the substrate, enabling identification of where this specific digital image 100 is from in the larger overall substrate. Such marks 104 are also useful for enabling determination of the location of a given item, e.g. an area of single-layer graphene, on the
35 substrate.

In addition, the digital image may comprise digital representations of tape residues, noise, scratches and/or other artefacts.

In this particular example, the substrate is silicon dioxide SiO_2 with a
5 thickness of 90 nm on silicon Si. However, other substrates, e.g. poly(methyl methacrylate) on Si or Al_2O_3 on Si or Al and/or other thicknesses may equally be used, as long as they provide a numerically significant contrast for the thin-film of interest.

10 A digital image, such as the one shown in Figure 1, may be used to identify single-, bi-, tri-, four- and/or few-layer thin-film material, e.g. like graphene, as will be described in further detail as one example in connection with Figure 2 and elsewhere.

15 Even though the digital image 100 in this particular example comprises graphene it is to be understood that other images comprising other types of layered thin-film material may also be investigated in a similar manner to identify a given layered thin-film material. As examples of such thin-film materials are e.g. Molybdenum disulphide (MoS_2), hexagonal boron nitride
20 (BN), Sb_2Te_3, $MoTe_2$,WS_2, $MoSe_2$, $TaSe_2$, Bi_2Te_3, $NbSe_2$, $NiTe_2$, etc.

As can be seen, the colour of single-layer graphene 101 is close to the colour of the background (i.e. the colour of the substrate) but still distinguishable by a human eye although perhaps not easily so.
25

Figure 2 schematically illustrates a flow-chart of one embodiment of a thin-film material identification method. Shown is a flow-chart 300 that starts at step 301. Before or when starting, a digital image (e.g. like the one shown in Figure 1) is provided or obtained for automatic processing in order to identify
30 single-, bi-, tri-, four- and/or few-layer thin-film material. In the following, graphene on a SiO_2 substrate will be used as an example.

At step 302 (an optional step), high-frequency noise – also often referred to as salt-and-pepper noise – is removed in order to obtain a more uniform
35 digital image enabling more reliable detection of one or more regions comprising graphene.

This may e.g. be done by applying a median filter or similar that replaces each pixel value with a median value of the surrounding pixels thereby effectively removing outlying pixels.

5

A median filter is very effective at removing salt-and-pepper noise while preserving the sharpness of edges and therefore particular useful for enabling or improving precision of area identification and/or of subsequent edge detection if used (see below for step 309) and/or other functions.

10

One example of applying such a filter or function may e.g. be seen in Figure 4 showing a digital image 100 after a median filter has been applied to the image of Figure 1. As can be seen, salt-and-pepper/high-frequency noise has been removed or diminished and the image contains more uniform colours.

15

After step 302, (optional) step 303 is carried out that applies additional image processing to enhance the identification process even further. More particularly, one or more dilation steps or similar is carried out followed by one or more erosion steps or similar. The number of dilation steps need not
20 be equal to the number of erosion steps.

Dilation and its counterpart – erosion – are in their basic form operations in mathematical morphology. Dilation is a convolution of a given image (binary, grey scale, or colour) with a kernel or the like, usually called a local maximum
25 operator. The operation replaces all pixels with the maximum value of the surrounding pixels limited by the size and shape of the kernel. As one example, a square 3x3 pixel kernel may be used. This has e.g. been used in connection with Figures 5a – 5f but it is to be understood that other shapes and/or sizes of the kernel may be used.

30

On a border between a darker and a lighter region in a given image, application of dilation will expand the border of the light region (being the same as reducing the border of the dark region) thereby increasing the areas of lighter areas while application of erosion will do the opposite, i.e. expand
35 the border of the dark region (being the same as reducing the border of the light region) thereby increasing the areas of darker areas.

Specifically in connection with identification of graphene (or other thin-film materials), dilation may be used to remove edges around small pieces, spots, or areas of graphite and residues since pixels with a positive pixel contrast
5 (i.e. darker than the background colour) close to the background colour will be eliminated.

Figures 5a – 5c illustrate one example of dilation being applied successively a number of times (in this particular example three times) to the image of
10 Figure 4.

As can be seen, the borders of light regions are expanded and the contribution from edges, etc. is greatly reduced in essence 'cleaning up' the image even further for more accurate processing.

15

However, the part(s) of the image that corresponds to graphene is reduced in size as well during this process. Therefore, to more accurately obtain more exact boundaries or borders of areas of graphene, one or more applications of erosion is performed afterwards.

20

Figures 5d – 5f shows one example of erosion being applied successively a number of times (in this particular example also three times).

As can be seen, the borders of the dark regions are expanded.

25

Applying dilation one or more times followed by applying erosion one or more times will (when being balanced but not necessarily equal) reduce or remove smaller and darker parts or elements of the image and then enlarge larger parts or elements more or less back to their original size where parts or
30 elements being removed will not be restored. This in essence further 'cleans up' of the image without removing and/or changing substantial colour and/or edge information for the graphene parts of the image.

After (optional) step 303, step 304 is carried out where the actual colour of
35 the specific background, i.e. the actual colour of the specific substrate, is determined.

12

It could be tempting simply to register the background colour of a reference image of the used substrate and then simply subtract the reference image, e.g. the RGB values (or similar in another colour space) or grayscale value,
5 from images of one or more wafers to be processed for identification.

However, when obtaining digital images of a substrate comprising graphene (or other thin-film material), the background colour changes over the entire, e.g. 4", wafer. The difference is quite pronounced and may be caused by
10 small variations in the thickness of the substrate, the lamp intensity of an illuminating source, the microscope/image capturing device shutter time, and/or the defocus due to wafer bow, etc.

Preferably, the background colour is determined individually for each image
15 to be processed for identification, e.g. as part of analysis of a series of images, to provide an actual colour of the specific background. Alternatively, the background colour may be determined once and used for subsequent images, which is simpler but not as accurate.

20 One simple and efficient way to determine the background colour is simply to use predetermined information of an approximate range of a background colour for a given substrate of a given thickness.

This predetermined information for one or more types of substrates may e.g.
25 be stored physically in an appropriate memory and/or storage (see e.g. 203 in Figure 11) for retrieval or use when needed.

For the specific example in Figure 1, the colour component value of each primary colour components R(ed), G(reen), and B(lue) is known to e.g. be
30 about 175±10, 145±10, 140±10. For grey-scale processing, the single colour component value is known to be about 150±10. It is to be understood, that other intervals may be used instead, e.g. 140±5, 140±15, etc. for each primary colour. The range should not be too narrow (potentially discarding background pixels) or too broad (less of an issue with respect to loosing
35 useful information but then simply wasting processing time and/or effort).

It is also to be understood that other colour spaces or models than RGB may be used, e.g. like HSL (hue, saturation, luminance), HSV (hue, saturation, value), HIS (hue, saturation, and intensity), etc.

5 Using a colour component value interval and pixel histograms for each primary colour component (or a single colour component interval and histogram for grey-scale images), the actual background colour component values (or grey-scale value) for the specific image may be determined, e.g. by determining a global optimum within the predetermined range for each 10 colour component (or grey-scale value) assuming that the background colour will be the far more dominant colour of the image. This assumption is very safe to make for images of this kind with material located in this manner on a substrate. Alternatively, other methods for determining the background colour could be equally valid.

15

This is e.g. illustrated in Figure 3 showing a pixel histogram for each of R (401), G (402), and B (403) using the RGB colour space. It can easily be seen that the background colour (the rightmost broken line in each pixel histogram) is far the dominant one.

20

As an alternative, an expected value and range of colour component values are not needed causing the need to determine a global optimum for each colour component over all the available values. This will work equally well for all other embodiments but just require more processing time and/or effort.

25

To derive one or more pixel histograms from a digital image is fairly straight forward and well known.

When the specific colour component values for the background colour have 30 been determined, the specific colour for graphene is then determined.

This is in this embodiment done by first obtaining one or more predetermined contrast values at step 305 e.g. from a suitable memory and/or storage (see e.g. 203 in Figure 11). For grey-scale images only a single contrast value is 35 obtained while three different contrast values are obtained for a colour image e.g. using R, G, B colour components. It is to be understood that other colour

models/spaces than RGB may be used and that the number of colour components may be different from three.

The contrast may be calculated as the difference between the colour
5 intensity, as represented by the values of the colour components, of the background and the colour intensity of graphene of interest divided by the colour intensity of the background, i.e.

$$C = \frac{I_{background} - I_{graphene}}{I_{background}}$$

10

This also holds for each colour component, e.g.

$$C_{red} = \frac{I_{background,red} - I_{graphene,red}}{I_{background,red}}$$

15 The inventors have realised and shown that the contrast of graphene of a given type (i.e. being either single, bi-, tri-, four-, or few layer graphene) in a digital image – for a given thickness of the substrate that the graphene is deposited on – is constant (to within a small tolerance) – even for different colour spaces/models – and likewise that the contrast of graphene for each
20 colour component is constant (to within a small tolerance) and uniquely determined by the substrate (and its thickness).

The contrast of graphene of a given layer is distinguishably different from the contrast of graphene of another given layer, e.g. the contrast of single layer
25 graphene is different than the contrast of bi-layer graphene that is different than the contrast of tri-layer graphene, and so on. The contrast of bi-layer graphene is about 2 times the contrast of single-layer graphene, while the contrast of three-layer graphene is about 3 times the contrast of single-layer graphene, etc.
30

This enables easy and efficient distinction and thereby separate identification of graphene of different layers including graphite.

For example, the R, G, B contrasts [C_R; C_G; C_B] for a digital colour image of
35 single-layer graphene on a 90 nm SiO_2 substrate is about [9%; 11%; 8%]. It can vary a bit due to small variations and errors. The inventors have for

example experimentally measured contrasts to be e.g. about [8.6%; 10.5%; 8.1%] as well as other examples.

Contrast values (e.g. for each colour component) may simply be measured
5 once for a given substrate as a function of the type of substrate and its thickness and then stored in a suitable memory and/or storage (see e.g. 203 in Figure 11) for later use.

One way of determining the contrast values for a given substrate with a given
10 thickness is e.g. to manually find a piece of graphene with an optical microscope, capture an image of the piece and measure the contrast. Alternatively one could calculate the contrast by considering light propagation in layered thin-films e.g. by using the Fresnel equations and convert it to an appropriate colour space.

15

After this predetermination, there is no need to measure it again for the same substrate with the same thickness avoiding the need for further calibration.

The specific value for each colour component of a given-layer graphene may
20 then be determined using such predetermined contrast values [C_R; C_G; C_B] for each colour component and the determined background colour (as determined at step 304) also for each component.

This is done at step 306 where the identified background colour components,
25 each is multiplied by the result of 1 minus the contrast of the same colour component of the graphene in question. It is to be understood that using values close to 1 may still give usable results.

For example, for single-layer graphene where the red component
30 background colour intensity has been determined to be 175 and the predetermined red contrast value C_R has been retrieved to be 9%, the result will be 175 x (1 – 9%) being equal to about 159 signifying that single-layer graphene's red colour component has a value of about 159 in the actual image. This corresponds to the peak in pixel values seen in the red
35 histogram around 159 in Figure 3. In a similar way, the values for green and blue are determined.

When these values are determined, the actual (or a very good estimate thereof) colour of the given type of graphene with the given number of layers in the given image is determined. Areas or regions containing that particular
5 type of graphene with that particular number of layers (being at least one) may then easily be identified e.g. simply by finding the parts of the image that have the same colour component values – preferably within a given range. This may e.g. be done simply searching for pixels in the image having the corresponding values (e.g. within a certain range) for each colour
10 component.

As an example continuing the above, if the single-layer graphene's red colour component has a value of 159 then all pixels having a red colour value within the range of e.g. 159±5 (and also fulfilling having a value within the suitable
15 range for both green and blue) is determined to contain single-layer graphene.

If other types of graphene, e.g. bi-layer graphene, are to be identified in the image as well, that may be derived in the same manner using the
20 predetermined contrasts for the particular types of graphene.

However, simply searching for pixels is not efficient. Alternatively, the relevant pixels may be determined according to (optional) steps 307 and 308 as will be described in the following.
25

Having determined the colour values for a particular type of graphene, a threshold is applied at step 307, where all pixels are discarded (e.g. set to the colour black) except those pixels having values corresponding to a suitable relatively small range around values of the particular type of graphene. The
30 remaining pixels may then be set to another colour, e.g. white. An exemplary result of this may be seen in Figure 6 for single-layer graphene.

It is important to note, that the threshold is applied to the three RGB colours together. If a given RGB pixel obeys the pixel-contrast (i.e. is within the
35 relevant value range) for anything less than all three colours it is discarded. Using constraints on three colours results in a much higher accuracy than in

grey-scale images where the three RGB colours are flattened into a single grey-scale colour, e.g. according to grey intensity = 0.3 x red intensity + 0.59 x green intensity + 0.11 x blue intensity or similar.

5 However, the process may still be used on grey-scale image – but then with less precision – whereby the threshold is applied only for a single grey-scale colour.

If several types of graphene are determined, they may each be given their 10 unique colour, e.g. single-layer graphene may be set to white, bi-layer graphene may be set to one given shade of grey, etc. Figure 8 shows an example of bi-layer graphene.

However, the obtained threshold image may still contain some artefacts and 15 noise – as also can be seen in Figures 6 and 8. This may be removed, e.g. according to (optional) step 308, where one or more steps of erosion followed by one or more steps of dilation is performed.

Alternatively, other filters may be applied achieving the same effect.

20

This effectively removes remnants of non-graphene pixels. While the combined erode and dilate steps serve to mostly preserve the area and shape of the graphene it should be noted that thin features will also be eliminated. However, that is not normally an issue as thin areas of graphene 25 (should the thin feature really represent this) is not normally of interest for further processing.

Figures 7 and 9 show the images of Figures 6 and 8, respectively, after application of erosion followed by dilation and an area of graphene can 30 clearly be seen and has been efficiently identified as such.

The procedure might end now. However, in some embodiments, further functions may (optionally) be applied as in step 309 depending on the use thereof. These functions may e.g. comprise applying an appropriate edge-or 35 contour detection algorithm, e.g. enabling more quantitative information about a given area of graphene to be derived.

When the contour/all the edges of a given graphene area has been determined, it is simple to calculate one or more parameters like area, perimeter, circularity, pseudo-length, pseudo-width, etc. Circularity
5 represents the ratio of actual perimeter to that of a circle with the same area. Pseudo-length is the length of a rectangle with the given area and perimeter while the pseudo-width is pseudo-length divided by the area.

Such parameters may be useful in characterising the graphene areas.
10 Especially area and circularity may be important parameters or constraints for detection of suitable graphene areas e.g. for use to be post-processed with E-beam lithography for Hall-bar devices requiring a certain length and width or for other uses.

15 A location of a graphene area on the substrate or wafer may be determined using the index marks of the image. This location information may e.g. (together with other relevant parameters) be used in a CAD program or similar enabling automatic optimised placement of devices in the identified graphene areas. This could include the identification of position and/or
20 orientation of individual domains of graphene grown on Cu, Ni, SiC, Ru, Ir and similar materials before or after transfer processes and processing.

Figure 10 shows the end result of processing the image of Figure 1 showing both identified single- and bi-layer graphene.

25

By optional steps is to be understood that they need not be present, even though they can be, in the procedure performing the identification, as opposed to being present but not invoked.

30 After one image has been processed and one or more e.g. differently layered graphene areas has/have been identified, the method may loop back to step 301 or 302 and process another image if applicable. This may e.g. be continued until all images of a wafer or similar has been processed and can also continue for more wafers.

35

It is to be understood that the execution order of steps 304 and 305 e.g. may be switched or even done in parallel. As another alternative, step 302 may be done after step 303.

5 Figure 3 schematically illustrates a graph of pixel histograms of each colour component obtained for an area around the single- and bi-layer graphene in Figure 1 to make the information more clear. Alternatively, they may be derived for the entire image. Shown is a pixel histogram for each of the colour components R (401), G (402), and B (403). The rightmost dashed line 10 is for the background colour, the middle dashed line is for single-layer graphene, while the left dashed line is for bi-layer graphene.

Figure 4 schematically illustrates the image of Figure 1 after (optional) image processing removing so-called salt-and-pepper noise without blurring edges 15 in the image. Shown is a processed digital image 100.

Figures 5a – 5f schematically illustrate the effect of (optional) additional image processing of the image of Figure 1.

20 Figures 5a – 5c illustrate the effect of applying dilation three times (one application per Figure).

Figures 5d – 5f illustrate the effect of applying erosion three times (one application per Figure).

25

Figure 6 schematically illustrates the image of Figure 1 after single-layer graphene has been identified and non-graphene has been removed with some artefacts and noise still present.

30 Figure 7 schematically illustrates Figure 6 after some additional image processing removing noise and/or artefacts.

Figure 8 schematically illustrates the image of Figure 1 after bi-layer graphene has been identified and non-graphene has been removed.

35

Figure 9 schematically illustrates Figure 8 after some additional image processing removing noise and/or artefacts.

Figure 10 schematically illustrates the end result of processing the image of Figure 1 showing both identified single- and bi-layer graphene.

The contents and actions of Figures 4 – 10 have been explained in more detail in connection with the flow chart of Figure 2.

Figure 11 schematically illustrates one embodiment of a system for automatic identification of a digital representation of single-, bi-, and/or few-layer thin-film material, e.g. graphene, in a digital image. Shown is a system 200 comprising at least one processing unit 201 connected via one or more communications and/or data buses 202 to a memory and/or storage 203, optional communications elements 204 e.g. for communicating via a network, the Internet, a Wi-Fi connection, and/or the like, and an (optional) display 205.

The system 200 may be a more or less standard computational system, like a PC, laptop, tablet, etc. or any other appropriate system suitably programmed to carry out the method or procedure as described in the various embodiments throughout the specification and variations thereof.

The system 200 optionally also comprises an image capturing device 206 for obtaining images like the one shown in Figure 1. Alternatively, such an image may simply be provided to the system 200.
In the claims, any reference signs placed between parentheses shall not be constructed as limiting the claim. The word "comprising" does not exclude the presence of elements or steps other than those listed in a claim. The word "a" or "an" preceding an element does not exclude the presence of a plurality of such elements.

The mere fact that certain measures are recited in mutually different dependent claims does not indicate that a combination of these measures cannot be used to advantage.

It will be apparent to a person skilled in the art that the various embodiments of the invention as disclosed and/or elements thereof can be combined without departing from the scope of the invention.

22

Patent Claims:

----

1. A method of automatically identifying one or more digital representations of single- (101) and/or few-layer (102) thin-film material in a digital image (100),
5 the digital image (100) having a predetermined number of colour components, and the method comprising

- determining (304) a background colour component of the digital image (100) for each colour component, and
- determining or estimating (306) a colour component of thin-film
10 material to be identified in the digital image (100) for each colour component, the thin-film material to be identified having a given number of layers being at least one,

wherein determining or estimating (306) a colour component of thin-film material to be identified in the digital image (100) for each colour component
15 comprises

- obtaining a pre-determined contrast value for each colour component and determining or estimating the colour component of the thin-film material to be identified and having the given number of layers for each colour component by, for each colour component, multiplying a
20 numerical difference between the pre-determined contrast value for a given colour component and about 1 with the background colour component for the given colour component,

and wherein the method further comprises

- identifying (307) one or more digital representations of single- (101)
25 and/or few-layer (102) thin-film material as points or parts of the digital image (100) that, for each colour component, has a colour component being within a predetermined range of the determined or estimated colour component of the thin-film material to be identified having the given number of layers.

30

2. The method according to claim 1, wherein the thin-film material is graphene.

3. The method according to claim 1, wherein the thin-film material is any one
35 selected from the group of

- molybdenum disulphide,

- hexagonal boron nitride,
- Sb_2Te_3,
- $MoTe_2$,
- WS_2,
- $MoSe_2$,
- $TaSe_2$,
- Bi_2Te_3,
- $NbSe_2$, and
- $NiTe_2$.

4. The method according to any one of claims 1 – 3, wherein
   - the digital image (100) is a grey-scale image or is converted into a grey-scale image and the number of colour components is one, or
   - the digital image (100) is a colour image and the number of colour components is three or more.

5. The method according to any one of claims 1 – 4, the method comprises identification of one or more digital representations of single- (101) and/or few-layer (102) thin-film material in a series of digital images (100), wherein
   - determining (304) a background colour component of the digital image (100) for each colour component, and/or
   - determining or estimating (306) a colour component of thin-film material to be identified in the digital image (100) for each colour component,

is done for each digital image of the series or is done once where the determination(s) are used for later digital images of the series.

6. The method according to any one of claims 1 – 5, wherein the thin-film material of the digital image (100) was located on a given substrate, having a predetermined thickness, when the digital image was captured and wherein determining (304) a background colour component of the digital image (100) for each colour component comprises
   - providing predetermined information of an approximate range of a background colour component for each colour component as a function of the particular type and a thickness of the given substrate.

7. The method according to any one of claims 1 – 6, wherein the method further comprises

- applying a filter (302), e.g. a median filter, to the digital image (100) to remove high-frequency noise and/or salt-and-pepper noise before
5 determining (304) a background colour component of the digital image (100) for each colour component,
- applying (303) one or more dilation steps followed by one or more erosion steps in order to improve the quality of the digital image (100) for identification of thin-film material,
10 – applying a threshold (307) where all pixels of the digital image (100) are discarded except those pixels that have, for each colour component, a colour component being within a second predetermined range of the determined or estimated colour component of the thin-film material to be identified having the given number of layers, and/or
15 – detecting edges or a contour (309) of at least one part of the digital image (100) that has been identified to be one or more digital representations of single- (101) and/or few-layer (102) thin-film material.

20 8. A system (200) for automatic identification of one or more digital representations of single- (101) and/or few-layer (102) thin-film material in a digital image (100), the digital image (100) having a predetermined number of colour components, wherein the system comprises one or more processing units (201) adapted to

25 – determine a background colour component of the digital image (100) for each colour component, and
- determine or estimate a colour component of thin-film material to be identified in the digital image (100) for each colour component, the thin-film material to be identified having a given number of layers
30 being at least one,

wherein one or more processing units (201) is adapted to determine or estimate a colour component of thin-film material to be identified in the digital image (100) for each colour component by

- obtaining a pre-determined contrast value for each colour component
35 and determining or estimating the colour component of the thin-film material to be identified and having the given number of layers for

25

each colour component by, for each colour component, multiplying a numerical difference between the pre-determined contrast value for a given colour component and about 1 with the background colour component for the given colour component,

5 and wherein the one or more processing units (201) is further adapted to

- identify one or more digital representations of single- (101) and/or few-layer (102) thin-film material as points or parts of the digital image (100) that, for each colour component, has a colour component being within a predetermined range of the determined or estimated colour
10 component of the thin-film material to be identified having the given number of layers.

9. The system according to claim 8, wherein the thin-film material is graphene.

15

10. The system according to claim 8, wherein the thin-film material is any one selected from the group of

- molybdenum disulphide,
- hexagonal boron nitride,
- Sb_2Te_3, (20)
- $MoTe_2$,
- WS_2,
- $MoSe_2$,
- $TaSe_2$,
- Bi_2Te_3, (25)
- $NbSe_2$, and
- $NiTe_2$.

11. The system according to any one of claims 8 – 10, wherein

- the digital image (100) is a grey-scale image or is converted into a grey-scale image and the number of colour components is one, or (30)
- the digital image (100) is a colour image and the number of colour components is three or more.

12. The system according to any one of claims 8 – 11, wherein the system is adapted to identify one or more digital representations of single- (101) and/or few-layer (102) thin-film material in a series of digital images (100), wherein
    - determining a background colour component of the digital image (100) for each colour component, and/or
    - determining or estimating a colour component of thin-film material to be identified in the digital image (100) for each colour component,

is done for each digital image of the series or is done once where the determination(s) are used for later digital images of the series.

13. The system according to any one of claims 8 – 12, wherein the thin-film material of the digital image (100) was located on a given substrate, having a predetermined thickness, when the digital image was captured and wherein the one or more processing units (201) is adapted to determine a background colour component of the digital image (100) for each colour component by
    - providing predetermined information of an approximate range of a background colour component for each colour component as a function of the particular type and a thickness of the given substrate.

14. The system according to any one of claims 8 – 13, wherein the one or more processing units (201) is further adapted to
    - apply a filter, e.g. a median filter, to the digital image (100) to remove high-frequency noise and/or salt-and-pepper noise before determining a background colour component of the digital image (100) for each colour component,
    - apply one or more dilation steps followed by one or more erosion steps in order to improve the quality of the digital image (100) for identification of thin-film material,
    - apply a threshold where all pixels of the digital image (100) are discarded except those pixels that have, for each colour component, a colour component being within a second predetermined range of the determined or estimated colour component of the thin-film material to be identified having the given number of layers, and/or
    - detect edges or a contour of at least one part of the digital image (100) that has been identified to be one or more digital representations of single- (101) and/or few-layer (102) thin-film material.

ABSTRACT

This invention relates to a system for and a method of automatically identifying one or more digital representations of single- (101) and/or few-layer (102) thin-film material in a digital image (100), the digital image (100)
5 having a predetermined number of colour components, and the method comprising

- determining (304) a background colour component of the digital image (100) for each colour component, and
- determining or estimating (306) a colour component of thin-film
10 material to be identified in the digital image (100) for each colour component, the thin-film material to be identified having a given number of layers being at least one,

wherein determining or estimating (306) a colour component of thin-film material to be identified in the digital image (100) for each colour component
15 comprises

- obtaining a pre-determined contrast value (C_R; C_G; C_B) for each colour component and determining or estimating the colour component of the thin-film material to be identified and having the given number of layers for each colour component by, for each colour component,
20 multiplying a numerical difference between the pre-determined contrast value (C_R; C_G; C_B) for a given colour component and about 1 with the background colour component for the given colour component,

25 In this way, robust and reliable identification of layered thin-film material in a digital image is provided since identification is made based on the actual colour of the background and then the actual colour of the thin-film material is derived using information about contrasts.

30 Figure 2 is to be published.

1/9

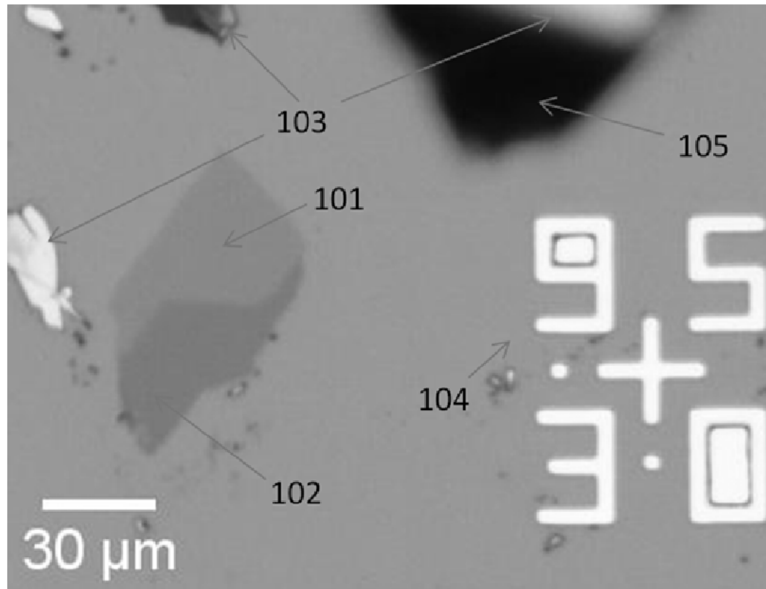

Figure 1 100

Figure 10 100

2/9

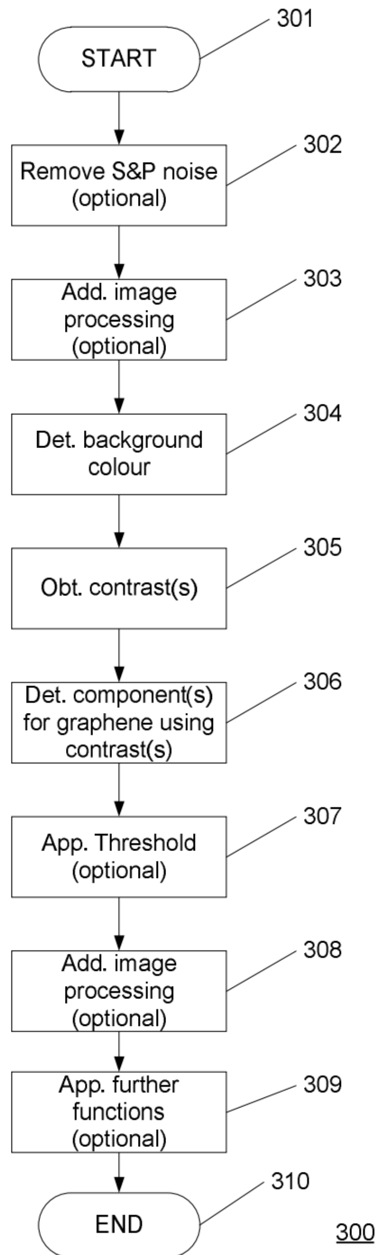

Figure 2

3/9

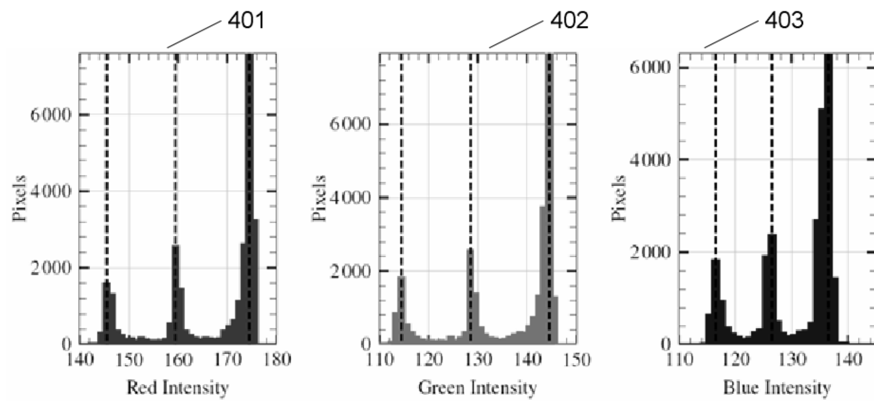

Figure 3

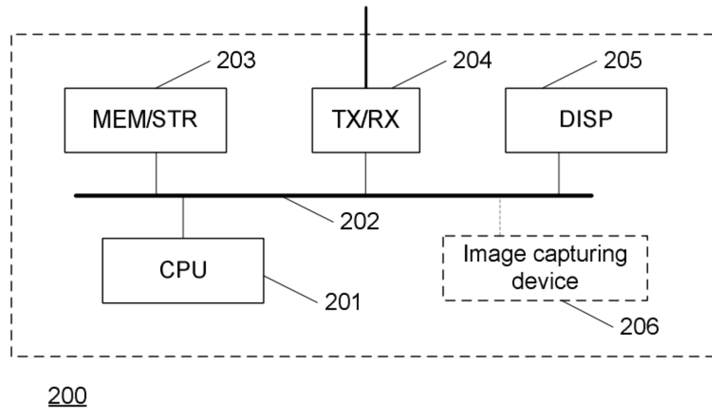

Figure 11

4/9

100

Figure 4

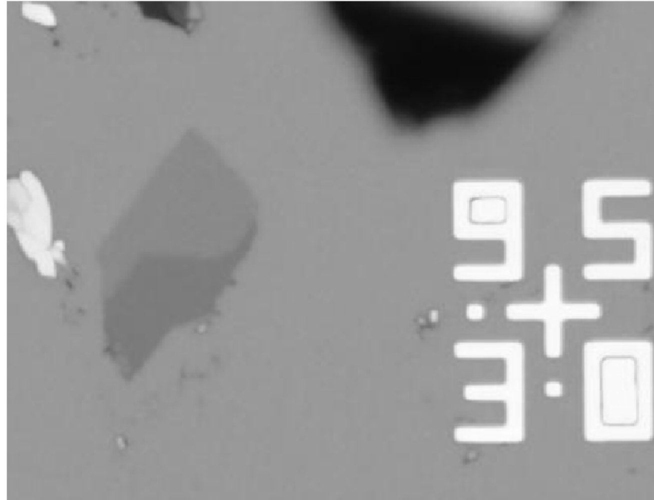

Figure 5a 100

Figure 5b 100

6/9

Figure 5c 100

Figure 5d 100

7/9

Figure 5e 100

Figure 5f 100

8/9

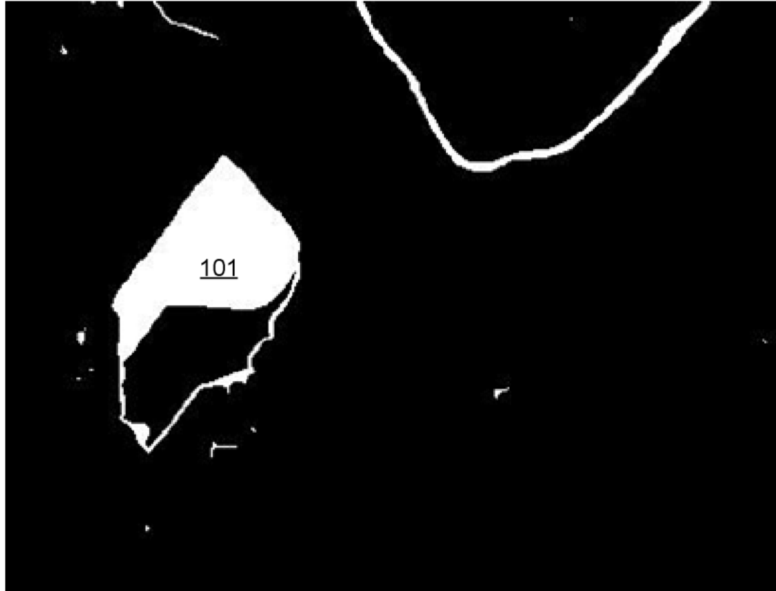

Figure 6 100

Figure 7 100

9/9

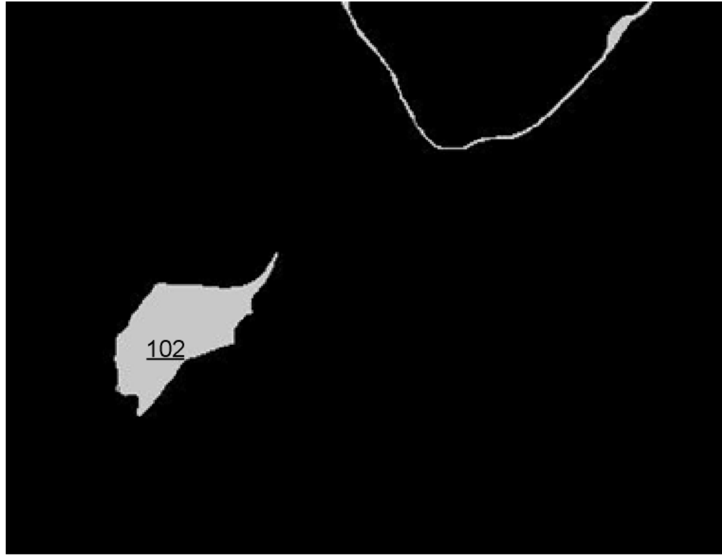

Figure 8 100

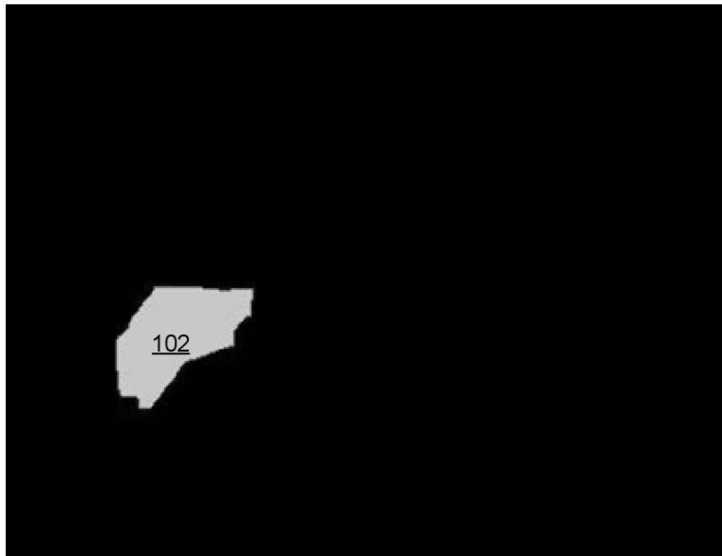

Figure 9 100